SAND2020-3887R
CASL-U-2020-1939-000

Consortium for Advanced Simulation of LWRs

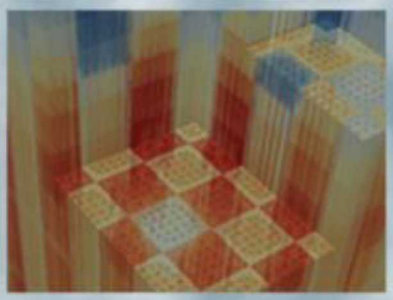
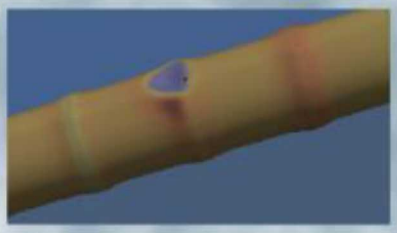
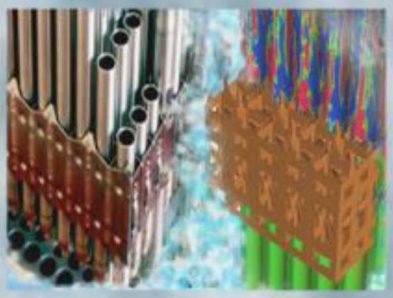

FY20 Verification of BISON Using Analytic and Manufactured Solutions

Aysenur Toptan[1], Nathan W. Porter[2], Jason D. Hales[1], Richard Williamson[1], and Martin Pilch[3]

[1]Idaho National Laboratory
[2]Sandia National Laboratories
[3]MPilch Consulting

31 March 2020

U.S. DEPARTMENT OF ENERGY | Nuclear Energy

Sandia National Laboratories is a multimission laboratory managed and operated by National Technology & Engineering Solutions of Sandia, LLC, a wholly owned subsidiary of Honeywell International Inc., for the U.S. Department of Energy's National Nuclear Security Administration under contract DE-NA0003525.

Revision Log

Revision	Date	Affected Pages	Revision Description
0	31 March 2020	All	Initial Release

Document pages that are:

Export Controlled:	None
IP/Proprietary/NDA Controlled:	None
Sensitive Controlled:	None
Unlimited:	All

Sandia National Laboratories is a multimission laboratory managed and operated by National Technology and Engineering Solutions of Sandia, LLC, a wholly owned subsidiary of Honeywell International, for the U.S. Department of Energy's National Nuclear Security Administration under contract DE-NA0003525. This paper describes objective technical results and analysis.

Executive Summary

In 2010, the U.S. Department of Energy created its first Energy Innovation Hub, which is focused on developing high-fidelity and high-resolution Modeling and Simulation (M&S) tools for modeling of Light Water Reactors (LWRs). This hub, Consortium for Advanced Simulation of LWRs (CASL), has developed an LWR simulation tool called Virtual Environment for Reactor Applications (VERA). The multi-physics capability of VERA is achieved through the coupling of single-physics codes, including BISON, CTF, MPACT, and MAMBA.

BISON is a fuel performance code which models the thermo-mechanical behavior of nuclear fuel using high performance M&S. It is capable of modeling traditional LWR fuel rods, fuel plates, and TRi-structural ISOtropic (TRISO) fuel particles. It can employ three-dimensional Cartesian, two-dimensional axisymmetric cylindrical, or one-dimensional radial spherical geometry. It includes empirical models for a large variety of fuel physics: temperature- and burnup-dependent thermal properties, fuel swelling and densification, fission gas production, cladding creep, fracture, cladding plasticity, and gap/plenum models.

This document details a series of code verification test problems that are used to test BISON. These problems add confidence that the BISON code is a faithful representation of its underlying mathematical model. The suite of verification tests are mapped to the underlying conservation equations solved by the code: heat conduction, mechanics, and species conservation. Twenty-two problems are added for the heat conduction solution, two for the mechanics solution, and none for species conservation. Method of Manufactured Solutions (MMS) capability is demonstrated with three problems, and temperature drops across the fuel gap are tested.

Contents

List of Figures

List of Tables

List of Symbols

Greek Letters		
α	Thermal diffusivity	m^2/s
ρ	Density	kg/m^3
$\boldsymbol{\sigma}$	Cauchy stress tensor	Pa
Nondimensional Numbers		
Bi	Biot $= hL/k$	
Fo	Fourier $= kt/(c_p \rho L^2)$	
Roman Letters		
c_p	Specific heat	kJ/K/kg
D	Diffusion coefficient	m^2/s
E	Young's modulus	Pa
$\dot{F}$	Volumetric fission rate	$/m^3$
$\boldsymbol{f}$	Body force per unit mass	N/kg
h	Characteristic grid size	
h	Heat transfer coefficient	$W/m^2/K$
k	Thermal conductivity	W/m/K
p	Basis function order	
q'''	Volumetric heat source	W/m^3
q''	Heat flux	W/m^2
u	Temperature	K
$\boldsymbol{u}$	Displacement field	
U	Generic quantity of interest	
Subscripts		
c	Clad	
ci	Clad inner	
co	Clad outer	
F	Formal	
f	Fuel	
O	Observed	

Acronyms

BVP	boundary value problem
CASL	Consortium for Advanced Simulation of LWRs
ECCS	Emergency Core Cooling System
FE	finite element
LWR	Light Water Reactor
INL	Idaho National Laboratory
MOOSE	Multiphysics Object-Oriented Simulation Environment
M&S	Modeling and Simulation
MES	Method of Exact Solutions
MMS	Method of Manufactured Solutions
PDE	partial differential equation
SQA	Software Quality Assurance
TRISO	TRi-structural ISOtropic
SNL	Sandia National Laboratories
QoI	quantity of interest
VERA	Virtual Environment for Reactor Applications

1. Introduction

The invention of the computer in the early nineteenth century has revolutionized the scientific process. The relatively quick evolution of computers and Modeling and Simulation (M&S) methods has enabled a detailed understanding of complex coupled physical phenomena. In the nuclear industry, M&S became a primary focus in the 1970's. During that century, many of the well-known nuclear simulation codes and methods were developed. As computational methods have continued to improve, the underlying numerical and computational methods of many of these "legacy codes" have become outdated, necessitating the development of modern computational tools.

The development of Multiphysics Object-Oriented Simulation Environment (MOOSE) at Idaho National Laboratory (INL) has been one project which attempts to fulfill the role of modern M&S software. It is a high-performance, open source, C++ finite element (FE) toolkit[1] [1]. This software package has generalized the conservation process into a finite-element formulation which can be applied to a variety of problems. It allows scientists and engineers to focus on the empirical models relevant to their particular field, while avoiding the details of computational science. One of the most prolific applications of the MOOSE framework is BISON [2, 3], which focuses on the simulation of nuclear fuel.

BISON is a fuel performance code which models the thermo-mechanical behavior of nuclear fuel using high performance M&S. BISON solves the fully-coupled equations of energy conservation, mechanics, and species conservation to account for a majority of possible fuel behaviors. It is capable of modeling traditional Light Water Reactor (LWR) fuel rods, fuel plates, and TRi-structural ISOtropic (TRISO) fuel particles. It can employ three-dimensional Cartesian, two-dimensional axisymmetric cylindrical, or one-dimensional radial spherical geometry. It includes empirical models for a large variety of fuel physics: temperature- and burnup-dependent thermal properties, fuel swelling and densification, fission gas production, cladding creep, fracture, cladding plasticity, and gap/plenum models.

In 2010, the U.S. Department of Energy created its first Energy Innovation Hub, which is focused on developing high-fidelity and high-resolution M&S tools for modeling of LWRs. This hub, the Consortium for Advanced Simulation of LWRs (CASL)[2], has developed an LWR simulation tool called the Virtual Environment for Reactor Applications (VERA). BISON is the high-fidelity and high-resolution fuel performance tool used in VERA.

[1] `www.github.com/idaholab/moose`
[2] `www.casl.gov`

Accurate simulation of nuclear fuels is an integral part of reactor analysis. In normal operating conditions, the fuel melting temperature limits the total power output of a reactor. A full characterization of the temperature distribution within the fuel requires an understanding of the thermo–mechanical behavior of crud deposits, cladding, gap, and fuel. Fuel behavior is also consequential to the modeling of severe accident scenarios, as the cladding serves as the first barrier which prevents releases of nuclear material. As such, cladding temperature, creep, swelling, and rupture are included as modeling requirements for testing of an LWR Emergency Core Cooling System (ECCS) [4]. As fuel modeling is important, consequential, and difficult to validate, it is necessary to ensure predictive capability by providing BISON with a thorough pedigree.

A variety of processes have been developed to quantify the reliability and predictive capability of M&S tools. Here, we provide a general overview of these processes; more detail can be found in [5, 6, 7]. In general, these processes include verification and validation.

1. *Verification* is used to ensure that the code functions correctly.
   (a) Software Quality Assurance (SQA) is the process of detecting unintentional coding mistakes in software. This is done through defect analyses (unit, component, and system tests), regression tests, and code comparisons.
   (b) *Code verification* ensures that the code is a faithful representation of the underlying mathematical model.
   (c) *Solution verification* is the assessment of all sources of numerical uncertainty: round-off, statistical variation, iterative tolerances, and truncation error.
2. *Validation* is the process of assessing a code's capability to accurately model physical problems. Comparisons between code results and experiments quantify this capability.

The application of these software development procedures is crucial to the development of computational tools that are free of coding mistakes and that accurately represent reality. A concise application of these procedures and a complete template for the necessary code development steps have been outlined and demonstrated for some models in a thermal-hydraulics subchannel code [8, 9, 10]. Existing verification and validation work in BISON can be found in [11, 12].

This study focuses on expanding the formal verification of BISON, with a primary focus on its conduction solution and secondary focus on mechanical behavior. The methodologies used in this work, verification procedure, and design of the test matrix are outlined in Chapter 2. Results for heat conduction are reported in Chapter 3. Appendix B details a few mechanics verification problems. The document concludes with a discussion of the results and future work in Chapter 4.

2. Methods

In this chapter, the BISON verification methodology is described. The first discussion is an outline of the BISON conservation equations and available solution options in Section 2.1. Verification is defined in detail in Section 2.2. The two code verification methodologies: Method of Exact Solutions (MES) and Method of Manufactured Solutions (MMS) are discussed in Section 2.3. The formal order of accuracy in BISON is derived in Section 2.4. Section 2.5 defines the verification procedure. In Section 2.6, the test matrix creation process is briefly described.

2.1 BISON Governing Equations

The BISON governing equations consist of three coupled partial differential equations (PDEs) for energy, species, and momentum conservation [3].

$$\underbrace{\rho c_p \frac{\partial u}{\partial t}}_{\text{transient}} - \underbrace{\nabla \cdot (k \nabla u)}_{\text{conduction}} - \underbrace{e_f \dot{F}}_{\text{fission}} = 0 \tag{2.1}$$

$$\underbrace{\frac{\partial C}{\partial t}}_{\text{transient}} - \underbrace{\nabla \cdot (D \nabla C)}_{\text{diffusion}} + \underbrace{\lambda C}_{\text{decay}} - \underbrace{S}_{\text{source}} = 0 \tag{2.2}$$

$$\underbrace{\nabla \cdot \boldsymbol{\sigma}}_{\substack{\text{Cauchy stress} \\ \text{tensor}}} + \underbrace{\rho \boldsymbol{f}}_{\text{body force}} = 0 \tag{2.3}$$

Here, all quantities are defined in the List of Symbols. For the momentum conservation equation, note that a constitutive relation is used to relate the primary solution variable—the displacement field $\boldsymbol{u}$—to the stress field via the strain.

These governing differential equations can each be separated into two parts: a balance equation or conservation principle and a constitutive equation or physical law. For example, for a one-dimensional steady state boundary value problem [13]

$$\text{balance equation:} \quad \frac{d\tau(x)}{dx} + \beta(x)U(x) = f(x), \quad \text{and} \tag{2.4}$$

$$\text{constitutive model:} \quad \tau(x) = -\alpha(x)\frac{dU(x)}{dx}. \tag{2.5}$$

Here, $d\tau(x)/dx$ represents loss of the conserved quantity from the system due to flow across boundaries, $\beta(x)U(x)$ represents interior losses, and $f(x)$ represents external sources. The proportionality constant, $\beta(x)$ is a physical or material property and $f(x)$ is generally known. The flux $\tau(x)$ represents the flow of some quantity, a force, or a stress. The flux is described as the derivative of the quantity of interest (QoI) $U(x)$ multiplied by some prescribed physical or material property $\alpha(x)$.

As an example, consider the heat conduction equation. In this case, the QoI $U(x)$ is temperature $u(x)$. The physical property $\beta(x)$ is the convection loss coefficient hL/A and the eternal source is composed of convection from ambient hLu_∞/A and an external heat source q'''. The constitutive equation which relates the flux to temperature is Fourier's law. Therefore, the one dimensional steady state heat conduction equation is

$$-\frac{d}{dx}\left(k\frac{du(x)}{dx}\right) + \frac{hL}{A}u(x) = q''' + \frac{hL}{A}u_\infty. \tag{2.6}$$

Division of conservation equations into these underlying components is important during the code verification process. The numerical convergence of the governing equation can be tested, but the underlying physical properties, material properties, and external sources (i.e., β, α, and f) must be tested separately. This is usually achieved by ensuring that (1) the models are coded correctly and return the expected values and (2) they do not degrade the order of accuracy when the models are enabled. This can be achieved through a combination of SQA and verification activities.

The BISON conservation equations are arranged into balance equations and constitutive models in Table 2.1. Note that only the elastic region is considered for solid mechanics.

Table 2.1: Definition of BISON conservation equations as one-dimensional boundary value problems

Application	Unknown	Physical/material		Exterior	Flux source	Balance equation	Constitutive equation	Governing equation
		properties	load					
General	U	α	β	f	τ	$\frac{d\tau}{dx} + \beta u = f$	$\tau = -\alpha\frac{du}{dx}$	$-\frac{d}{dx}\left(\alpha\frac{du}{dx}\right) + \beta u = f$
Heat cond.	u	k	$\frac{hL}{A}$	$q''' + \frac{hL}{A}u_\infty$	q	$\frac{dq}{dx} + \frac{hL}{A}u = q''' + \frac{hL}{A}u_\infty$	$q = -k\frac{du}{dx}$	$-\frac{d}{dx}\left(k\frac{du}{dx}\right) + \frac{hL}{A}u = q''' + \frac{hL}{A}u_\infty$
Elasticity	u	E		f	σ	$-\frac{d\sigma}{dx} = f$	$\sigma = E\frac{du}{dx}$	$-\frac{d}{dx}\left(E\frac{du}{dx}\right) = f$
Species diff.	C	D	λ	S	j	$\frac{dj}{dx} + \lambda C = S$	$j = -D\frac{dC}{dx}$	$-\frac{d}{dx}\left(D\frac{dC}{dx}\right) + \lambda C = S$

To solve the prescribed conservation equations, BISON uses an FE method [14, 15, 13, 16, 17] as implemented in the INL tool MOOSE. BISON is capable of generating simple meshes using the MOOSE input

`GeneratedMeshGenerator`[1]. For more complex geometries, BISON can import meshes generated using other tools, such as CUBIT, which is a mesh generation tool developed at Sandia National Laboratories (SNL) [18].

The FE framework used in MOOSE is typically libMesh, which is a FE library developed at the University of Texas at Austin. The FE types defined in libMesh and used in BISON are defined in Table 2.2.

Table 2.2: FE types used in the BISON/MOOSE solution algorithm

Dim.	Description	Pictorial representation			
1D	elem_type	`EDGE`			
	type	line			
	shape				
2D	elem_type	`TRI`	`QUAD`		
	type	triangular	quadrilateral		
	shape				
3D	elem_type	`HEX`	`TET`	`PRISM`	`PYRAMID`
	type	hexahedron	tetrahedron	prism	pyramid
	shape	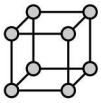	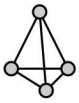	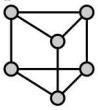	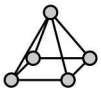

Though BISON is based upon libMesh and MOOSE and both of those codes have been individually verified, it is also important to verify BISON. This ensures that there are no errors in the incorporation of libMesh or MOOSE into the BISON framework. For example, it would be possible that BISON passes an incorrect index to MOOSE. Even though MOOSE would solve the problem correctly, this coding error would disrupt the BISON order of accuracy. Therefore, individual verification of BISON is an important step to establishing its credibility.

2.2 Verification

In the context of large simulation codes solving nonlinear PDEs, verification involves quantifying numerical errors between known and discrete solutions [5]. Verification is composed of three components: SQA, code verification, and solution verification.

1. SQA is used to eliminate coding errors and is comprised primarily of software engineering practices: version control, regression testing, defect testing, quantification of code coverage, and code-to-code comparisons.
2. Code verification ensures that *the computer code is a faithful representation of the underlying mathematical model.* This is achieved through the comparison of code solutions to a known solution as its

[1] `https://mooseframework.org/source/mesh/GeneratedMesh.html`

mesh is refined. Through comparison to the expected behavior of the discretization error, it can be ensured that the numerical algorithm is behaving correctly.

3. Solution verification focuses on the estimation of numerical errors that occur when a mathematical model is discretized and solved on a digital computer. Though solution verification and code verification have some similar methodology, solution verification uses problems which do not have a known solution. Therefore, numerical errors must be estimated and not simply evaluated. This includes all sources of numerical error: round-off, statistical sampling, iterative error, and discretization errors.

Note that some literature includes SQA as a part of code verification (e.g., [5, 19]). Here, the two activities are distinguished to clearly separate testing of the numerical algorithm from other testing activities. Verification is concerned only with computer science and mathematics. Validation activities, which are concerned with the actual behavior of real-world systems and comparisons to experimental data, are out of the scope of this work. Existing validation results for BISON are outlined in [11].

2.3 MES and MMS

In general, the code verification process ensures that the coded numerical algorithm is a faithful representation of the underlying mathematical model. Here, we notate the the intended mathematical model as some nonlinear system operator $\mathcal{L}$.

$$\mathcal{L}[f(\vec{x},t)] = 0 \tag{2.7}$$

The solution $f(\vec{x},t)$ is a function of space $\vec{x}$ and time t. The first option for finding a known solution is to use the Method of Exact Solutions (MES) [19], which involves calculating an exact analytic solution to Eq. 2.7. However, finding a nontrivial analytic solution to a complex nonlinear differential equation is difficult. The solution of these equations often requires significant simplifying assumptions. For example, many analytic solutions require that one or more of the terms in the PDE are trivial and eliminated from the solution. This process becomes even more difficult when a system of nonlinear equations is considered. Often, only approximate solutions are possible. for example, the well-known Navier-Stokes equations only have analytic solutions for the most trivial boundary and initial conditions.

A complete set of code verification analyses would require that all features of a code are tested. At its best, application of MES to the verification of all code options is a laborious process; at its worst, it can preclude sufficient testing of one or more relevant code options. For example, many analytic solutions involve only a single equation of state, varying property, or nonlinear source, and no solution is possible with multiple combinations of these complex physics. However, many codes default setting is to use a variety of equations of states, many varying properties, and nonlinear sources.

To address thorough code verification, analysts can employ the Method of Manufactured Solutions (MMS) [5, 7, 19, 20]. In this method, a particular problem is worked backwards. The analyst determines a particular form of the solution $M(\vec{x},t)$. Then one seeks the necessary space- and time-dependent

source $Q(\vec{x},t)$ that would result in the manufactured solution:

$$\mathcal{L}\left[M(\vec{x},t)\right] = Q(\vec{x},t). \tag{2.8}$$

The source $Q(\vec{x},t)$ is implemented in the simulation tool, then the verification process is performed. This methodology requires that the manufactured solution is formulated using continuous and smooth functions. These functions must be sufficiently complex to reveal nonlinearity in the governing equations. The chosen manufactured solution can be physically unrealistic, as it is intended only to test the underlying numerical algorithms. MMS is particularly powerful when combined with symbolic computation tools (e.g., Mathematica), as calculation of the source term can be automated.

Any necessary boundary conditions or initial conditions can be derived directly from the manufactured solution $M(\vec{x},t)$. Any equations of state, varying properties, or nonlinear sources can be incorporated into the MMS process by implementing them in the nonlinear operator $\mathcal{L}$. This allows all relevant code options to be tested in different combinations. In addition, MMS does not require the complex analytic solutions formed for MES, which greatly reduces the labor required for the verification process.

In this work, a series of traditional MES problems are solved for BISON to establish a pedigree. For the conduction solution, these include steady state problems solved on one- and two-dimensional domains with a variety of properties and external sources. Once this baseline pedigree is established, the MMS capability in BISON is demonstrated using three manufactured problems. For the mechanics solution, these problems include two preliminary MES problems (see Appendix B), which is not enough to construct a full test matrix.

2.4 Order of Accuracy

In this section, the formal order of accuracy is established for spatial and temporal discretization in BISON.

Spatial Order To establish the spatial formal order of accuracy of the BISON solution algorithm, we provide a heuristic derivation [13, 17] and point the reader to more mathematically rigorous analyses with the same result [14, 15, 16, 21]. In this work, the convergence of the computed solution to the analytic solution is analyzed as the size of the FEs approaches zero, e.g., h-convergence. No effort is made to quantify p-convergence, during which convergence is analyzed as the order of the basis functions is increased [22].

For problems in this work, there are no singularities in mesh, properties, or external sources. All analytic solutions are continuous, smooth, and infinitely differentiable. The mesh has constant spacing and is uniformly refined. Under these conditions, the analysis of the discretization error is relatively simple. Here, we will analyze the error behavior of the QoI U at some specified point in the domain x^*, and use the results to generalize about the entire domain. First, note that the exact solution to a specific problem can be represented by a Taylor series about some point $\hat{x}$ in the FE that contains x^*:

$$U(x) = \sum_{n=0}^{\infty} \frac{1}{n!} \left.\frac{d^n U}{dx^n}\right|_{\hat{x}} (x-\hat{x})^n. \tag{2.9}$$

This expansion assumes that $U(x)$ is infinitely differentiable, which is true for all solutions in this work. Here, we have used a Taylor series approximation, which corresponds to a polynomial basis function of degree p. Note that this procedure is equally applicable to other basis functions. The approximate solution calculated by the simulation tool $\tilde{U}$ using the chosen basis function of degree p is

$$\tilde{U}(x) = \sum_{n=0}^{p} a_n (x - \hat{x})^n. \tag{2.10}$$

The Taylor series coefficients have been collapsed into the arbitrary constant a_n. We define the length of an element as h and note that $|x - \hat{x}| \leq h$ because $\hat{x}$ is a point inside the element. As the mesh is uniformly refined, $h \to 0$, the approximate solution $\tilde{U}$ approaches arbitrarily close to the terms of Eq. 2.9 which are degree p or lower. In addition, the domain point x^* approaches the FE point $\hat{x}$ as the mesh is refined. Therefore, the remaining terms of $p+1$ and greater will form the error at point x^*.

$$U(x^*) - \tilde{U}(x^*) \to \sum_{n=p+1}^{\infty} c_n (x - \hat{x})^n, \quad \text{as } h \to 0. \tag{2.11}$$

Note that c_n is a constant which includes the coefficient and derivative term from Eq. 2.9. For a sufficiently small h, higher order terms become negligible and the $p+1$ term will dominate.

$$U(x^*) - \tilde{U}(x^*) = c_{p+1} h^{p+1} \tag{2.12}$$

Now we generalize the error at a single point (Eq. 2.12) to all of space using a norm:

$$||U(x)||_{L_2(\Omega)} = C h^{p+1}, \tag{2.13}$$

where C is an arbitrary constant that is problem-dependent, and the MOOSE function `ElementL2Error`[2] is used to compute the L2 norm over the domain Ω:

$$||U||^2_{L_2(\Omega)} = \int_{\Omega} (U - \tilde{U})^2 d\Omega = \sum_{\Omega} (U - \tilde{U})^2. \tag{2.14}$$

As Eq. 2.13 is an exponential function, the slope of error on a log-log plot is the observed order of accuracy $p_O = p + 1$. Note that the finite element degree p is sometimes referred to as the finite element order; however, it is not equivalent to the order of accuracy for a particular numerical method, which we notate as $p + 1$. Using two different meshes, the observed order of accuracy can be approximated as

$$p_O = \frac{\log\left(||U||_{2h} / ||U||_h\right)}{\log(2)}. \tag{2.15}$$

All of the above arguments can also be applied to the flux. Since the flux is the first derivative of the QoI, its asymptotic rate should be one order lower than that of the function, that is its formal order is the same as the degree of the chosen FE.

[2] `https://mooseframework.org/docs/doxygen/moose/ElementL2Error_8C_source.html`

$$||U(x)||_{H_{1,\text{semi}}(\Omega)} = Ch^p, \tag{2.16}$$

where C is an arbitrary constant that is problem-dependent, and the MOOSE function `ElementH1SemiError`[3] is used to calculate the norm.

$$||U||^2_{H_{1,\text{semi}}(\Omega)} = \int_\Omega |\nabla(U - \tilde{U})|^2 d\Omega = \sum_\Omega \left|\nabla\left(U - \tilde{U}\right)\right|^2 \tag{2.17}$$

Eq. 2.15 can also be used to estimate the observed order of accuracy p_O for the flux.

Temporal Order The MOOSE framework provides eight time discretization options which can be used to solve the transient BISON conservation equations:

1. Implicit/backward Euler (default),
2. Explicit/forward Euler,
3. Crank-Nicolson,
4. Two-step backward differentiation formula (BDF),
5. Explicit midpoint,
6. Diagonally implicit Runge-Kutta (DIRK),
7. Explicit total variation diminishing (TVD) two-stage Runge-Kutta, and
8. Newmark-beta.

Here, we derive the formal order of accuracy for the implicit Euler method, which is the default option in BISON. Similar exercises can be completed for all methods. We notate the transient conservation equation for some QoI U as

$$\frac{\partial U}{\partial t} = \mathcal{M}\left(\vec{x}, t, U\right) \tag{2.18}$$

here, $\mathcal{M}$ is some function of space $\vec{x}$, time t, and the QoI U which includes the finite element treatment of U. The implicit Euler scheme discretizes this equation as

$$\frac{U^{n+1} - U^n}{\Delta t} = \mathcal{M}\left(\vec{x}, t, U^{n+1}\right) \tag{2.19}$$

The QoI at $n+1$ is expanded about n to approximate the numerical error in time:

$$U^{n+1} = \sum_{k=0}^{\infty} \frac{1}{k!} \left.\frac{\partial^k U}{\partial t^k}\right|^n \Delta t^k \approx U^n + \left.\frac{\partial U}{\partial t}\right|^n \Delta t + \frac{1}{2} \left.\frac{\partial^2 U}{\partial t^2}\right|^n \Delta t^2 \tag{2.20}$$

This is substituted into Eq. 2.19 and simplified, yielding:

$$\left.\frac{\partial U}{\partial t}\right|^n + \frac{1}{2} \left.\frac{\partial^2 U}{\partial t^2}\right|^n \Delta t = \mathcal{M}(\vec{x}, t, U^{n+1}) \tag{2.21}$$

[3] `https://mooseframework.org/docs/doxygen/moose/classElementH1SemiError.html`

The second term scales with Δt, so the implicit Euler method is first order in time. Note that additional numerical error is introduced by the remaining U^{n+1} terms, but these errors will be first order or greater. Similar analyses performed on the other time integration schemes indicate that three of the methods (implicit Euler, explicit Euler, and explicit midpoint) are first order and the rest are second order.

2.5 Code Verification Procedure

The purpose of code verification is to ensure that discretized equations solved on a computation system faithfully represent the underlying continuous equations. This is achieved by comparing the formal and observed orders of accuracy. For each problem, a practical prescribed process is followed.

1. **Define and solve the mathematical model.** For MES problems, this involves selecting the conservation terms to be tested, setting boundary conditions and/or initial conditions, and mathematically solving the analytic problem. For MMS, a manufactured solution is chosen and the corresponding source term is derived.
2. **Choose the numerical algorithm and establish formal order of accuracy.** In BISON, a variety of FE types and temporal discretization schemes are available; one or more methods must be selected before solving the numerical problem. The corresponding formal order of accuracy for each method was established in Section 2.4.
3. **Obtain numerical solutions.** After formulating the required mesh and input deck, a numerical representation of the mathematical model is solved on at least four meshes. In this work, many meshes are evaluated to examine the behavior outside the asymptotic region. For steady state problems, only the spatial mesh is refined; however, the spatial and temporal mesh can be refined simultaneously for transient problems. Such combined order analysis methodology has been analyzed in [23]. Given the spatial and temporal formal order of accuracy, refinement factors can be selected from Table 2.3, which gives the corresponding expected reduction in error.
4. **Examine convergence behavior.** The expected convergence behavior is shown in Fig. 2.1. When the mesh is coarse, higher order terms degrade the order of accuracy (region **I**). The region analyzed in the code verification process is the *asymptotic region* (region **II**), where the higher order terms are small enough that the observed order approximates the formal order. Finally, the numerical solution cannot converge to a tolerance finer than external sources of numerical error; therefore, as the mesh is refined further, there is a leveling-off of error and a slight increase as numerical error accumulates (region **III**). In this work, the source of numerical error is primarily due to the iterative tolerance for the matrix solve. Finally, note that some problems will display hyper-convergent behavior. This is expected for problems where the FE order is high enough to exactly fit the analytic solution. For example, a first order method exactly approximates a linear solution and a second order method exactly approximates a quadratic solution. In these cases, the error plot starts in region **III**, as it immediately approximates the analytic solution to within numerical error.

Table 2.3: Temporal refinement factors required to conduct combined spatial and temporal order verification (from [5]). Temporal verification can be conducted by choosing a temporal refinement factor—for more complicated cases with $p \neq q$—according to [24] as $r_t = (r_x)^{p/q}$.

Spatial order, p	Temporal order, q	Spatial refinement factor, r_x	Temporal refinement factor, r_t	Expected error reduction ratio (coarse/fine)
1	1	2	2	2
1	2	2	$\sqrt{2}$	2
1	3	2	$\sqrt[3]{2}$	2
1	4	2	$\sqrt[4]{2}$	2
2	1	2	4	4
2	2	2	$\sqrt{4}$	4
2	3	2	$\sqrt[3]{4}$	4
2	4	2	$\sqrt[4]{4}$	4
3	1	2	8	8
3	2	2	$\sqrt{8}$	8
3	3	2	$\sqrt[3]{8}$	8
3	4	2	$\sqrt[4]{8}$	8

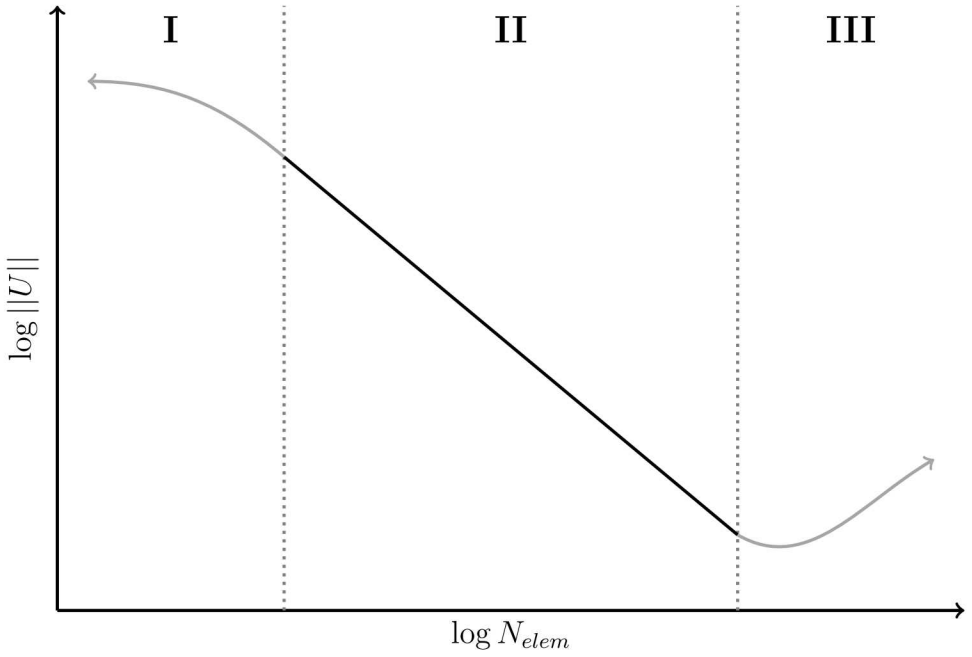

Figure 2.1: A pictorial representation of expected convergence behavior. Region **I** represents coarse meshes, region **II** is the asymptotic region, and region **III** is caused by numerical error.

5. **Debug and correct errors if necessary.** If the convergence behavior is significantly different than Fig. 2.1, it indicates an error in the analytic solution, numerical model, or post-processing of the simulation results. Debugging and correcting these errors is an integral part of the verification process.
6. **Document results.** The numerical and analytic solutions will be plotted using different FEs and meshes, then the convergence plot is created. These are included in this document, and also added to existing BISON documentation. In addition, code mistakes that are fixed as a result of the debugging process are also documented in Chapter 4.

Once this process is complete and the observed order of accuracy matches the formal order of accuracy, the particular code verification problem is successful. The problem is added as evidence that the particular combination of physics, discretization, geometry, boundary conditions, and initial conditions is numerically free of coding mistakes.

2.6 Test Matrix Construction

The selection of MES and MMS problems is an important part of the verification process. An analyst is tasked with providing enough evidence that the numerical algorithm is correct without performing redundant or unnecessary work. In this report, we approach this issue by first incorporating each option for physics, geometry, boundary condition, and FE into at least one verification problem. Once each option has been tested, we expand on the verification matrix by employing different *combinations* of these options. This ensures that the coupling between different options does not reveal coding mistakes that are otherwise hidden.

Chapter 3 presents the verification matrix for heat condition and corresponding numerical results. For the mechanics solution, there are not enough completed examples to fully define a verification matrix. However, a few preliminary examples are included in Appendix B. In the future, these will be expanded upon and a matrix will be formulated.

3. Thermal

In this chapter, the first conservation equation solved in BISON is considered: heat conduction. For all types of fuel—fuel plate, fuel rod, and TRISO particle—the transport of heat through the fuel is of utmost importance when determining the cladding and fuel temperatures, which are enforced as safety limits. In Section 3.1, the heat conduction equation itself is verified using a series of sixteen MES and three MMS problems. Section 3.2 expands these analyses to include an important consideration for nuclear reactors: the temperature jump across a gap in the fuel. This is verified for all three coordinate system options in BISON: Cartesian, cylindrical, and spherical.

3.1 Basic Heat Conduction

As provided in Chapter 2, the heat conduction equation solved in BISON is

$$\rho c_p \frac{\partial u}{\partial t} - \nabla \cdot (k \nabla u) + \dot{q} = 0. \tag{3.1}$$

The vector identities provided in Appendix A can be used to transform this vector equation into all three coordinate systems solved in BISON: Cartesian, cylindrical, and spherical coordinates.

This equation requires testing of both the temporal and spatial order of accuracy. In addition, the implementation of the thermal conductivity and external heat source can be verified. In many classic solutions for the conduction equation, the thermal conductivity is treated as constant. When this assumption is relaxed, the conduction equation becomes nonlinear and difficult to solve. Usually, numerical methods are required to solve these problems, though analytical methods can be applied to some simple cases. These simple cases are used to verify BISON for these types of problems.

For transient problems, a suitable time step must be selected such that the numerical solution is stable. The limiting choice of temporal discretization scheme which requires the smallest time step is explicit Euler. The limit for numerical stability of this method is established using von Neumann stability analysis [25]. The criterion for the stability requirement in three dimensions (where the spatial coordinates are defined in the general form $\vec{x} = \{x_1, x_2, x_3\}$) is given by

$$r = \alpha \left(\frac{\Delta t}{(\Delta x_1)^2} + \frac{\Delta t}{(\Delta x_2)^2} + \frac{\Delta t}{(\Delta x_3)^2} \right) \leq \frac{1}{2}, \tag{3.2}$$

where α is the thermal diffusivity ($\alpha = k/(\rho c_p)$, Δt is the time step size, and Δx_i is the spatial mesh size in i-th direction for $i = 1, 2, 3$. This limit is sometimes referred to as the Fourier limit. Because the denominator is squared, combined spatial and temporal mesh refinement studies can be computationally expensive.

A verification matrix is constructed following the methodology discussed in Section 2.6 and considering available resources. It includes all considerations discussed so far: treatment of the temporal term, coordinate system, dimensions, property and source term treatment, and boundary conditions. The matrix is shown in Table 3.1 and includes sixteen MES and three MMS problems. Literature sources for the MES problems are listed. The MMS problems are included to demonstrate BISON capability, rather than to fill gaps in the verification matrix. All options in the matrix have at least one corresponding test except for three-dimensional conduction, temperature-dependent specific heat, and temperature-dependent thermal diffusivity. Different combinations of options are tested, though not *all combinations* are tested.

For each problem in Table 3.1, this chapter includes a problem description, BISON results compared to the analytic solution, and a convergence plot for both temperature and heat flux. The observed order of accuracy for most problems match with the formal order derived in Section 2.4. Therefore, these results can be added as evidence that the conduction equation is implemented correctly in BISON and is free of coding mistakes.

Table 3.1: Verification matrix for BISON conduction equation

	Reference	Transient		Coordinate System			Dimension			Properties and External Sources						Boundary Conditions		
		Transient	Steady State	Cartesian	Cylindrical	Spherical	x_1	x_2	x_3	k_c	$k(T)$	q'''	$q'''(\vec{x})$	α_c	$\alpha(T)$	Drichlet	Neumann	Convective
Method of Exact Solutions																		
3.1	[26]		✓	✓			✓			✓		✓				✓		
3.2	[26]		✓	✓			✓				✓					✓		
3.3	[27]		✓	✓			✓				✓	✓				✓	✓	
3.4	[28]		✓	✓			✓	✓		✓						✓		
3.5	[26]		✓		✓		✓			✓						✓		
3.6	[26]		✓		✓		✓				✓					✓		
3.7	[28]		✓		✓		✓				✓	✓				✓		
3.8	[29]		✓		✓		✓			✓		✓					✓	✓
3.9	[29]		✓		✓		✓			✓		✓					✓	✓
3.10	[28]		✓		✓		✓		✓	✓						✓		
3.11	[29, 30]		✓			✓	✓			✓		✓				✓		
3.12	[26]		✓			✓	✓			✓						✓		
3.13	[26]		✓			✓	✓				✓					✓		
3.14	[29, 31]		✓			✓	✓			✓			✓			✓		
3.15	[29, 32]		✓			✓	✓			✓		✓						✓
3.16	[29]		✓			✓	✓			✓		✓				✓	✓	
Method of Manufactured Solutions																		
3.17			✓	✓			✓			✓						✓	✓	
3.18			✓	✓			✓	✓		✓						✓		
3.19	[1]	✓		✓			✓			✓				✓		✓		

Problem 3.1: Plate with internal heating

An infinite plate has constant thermal conductivity k and internal heat generation q'''. It is exposed on each face to a constant temperature, $u(0) = u_0$ and $u(\ell) = u_\ell$, and reaches thermal equilibrium. The analytic solution for the temperature distribution in the plate is the quadratic function [26, p.169]

$$u(x) = u_0 - (u_0 - u_\ell)\left(\frac{x}{\ell}\right) + \frac{q'''}{k}\frac{x(\ell - x)}{2}. \tag{3.3}$$

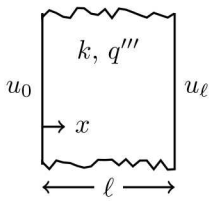

The problem is run in BISON on the domain $\boldsymbol{X} \in [0, 1]$ using the dirichlet boundary conditions $u(0) = u_0 = 100\,\mathrm{K}$ and $u(1) = u_\ell = 0\,\mathrm{K}$. Steady state heat conduction is considered with constant thermal conductivity $k = 12\,\mathrm{W/m/K}$ and volumetric heat generation $q''' = 1200\,\mathrm{W/m^3}$. The exact and computed solutions are shown in Fig. 3.1 for four different meshes and two finite element types (linear: `EDGE2`; quadratic: `EDGE3`).

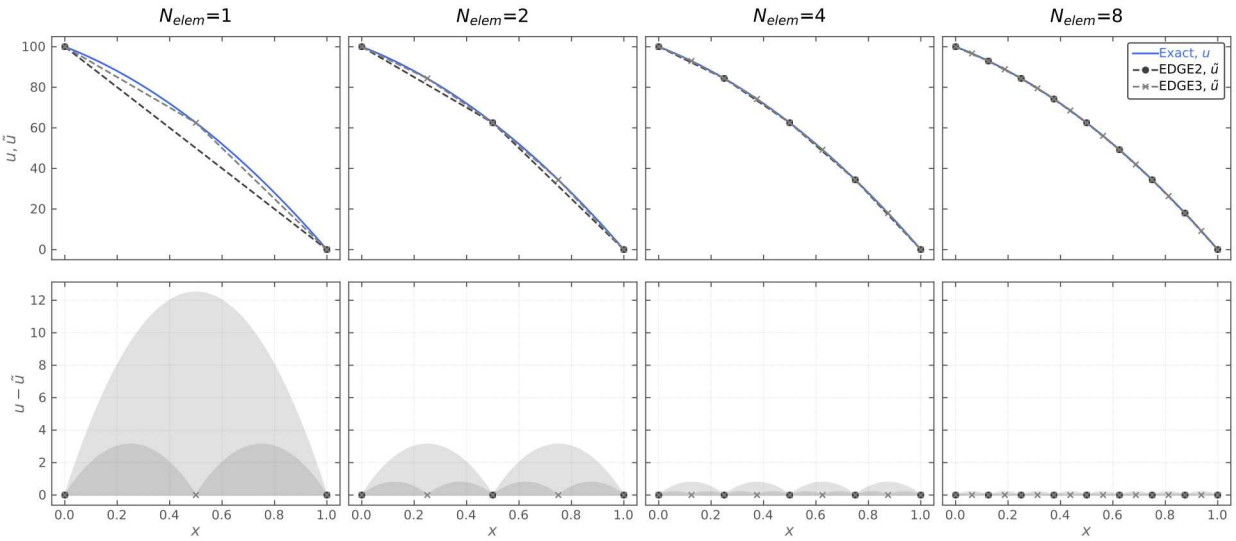

Figure 3.1: Temperature distribution and residuals for Prob. 3.1. Results are shown for the first four meshes. *First row*: exact and FE solutions using 1D elements. *Second row*: residuals between the exact and computed solutions.

A convergence study is conducted with a refinement factor of two (i.e., $r_x = 2$). The computed norms for each element type are plotted and tabulated in Fig. 3.2. In the asymptotic region, the linear FE solution converges to the exact solution second order, which matches with the formal order of accuracy. The quadratic solution instantly converges to the exact solution within numerical error due to the quadratic shape of Eq. 3.3.

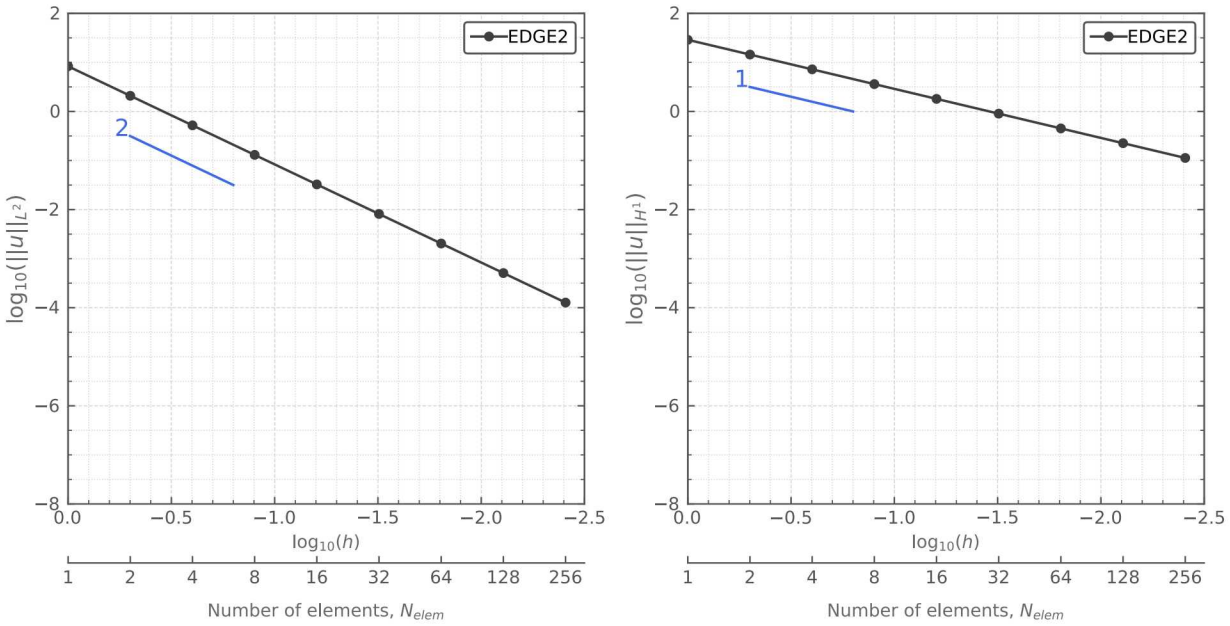

No. Elems	h	**Linear** ($p=1$) $\|\|u\|\|_{L_2}$	**Linear** ($p=1$) $\|\|u\|\|_{H_1}$	**Quadratic** ($p=2$) $\|\|u\|\|_{L_2}$	**Quadratic** ($p=2$) $\|\|u\|\|_{H_1}$
		elem_type=EDGE2		elem_type=EDGE3	
1	1.000000	8.333×10^{0}	2.887×10^{1}	4.341×10^{-14}	1.271×10^{-13}
2	0.500000	2.083×10^{0}	1.443×10^{1}	5.674×10^{-14}	2.452×10^{-13}
4	0.250000	5.208×10^{-1}	7.217×10^{0}	2.464×10^{-11}	1.613×10^{-10}
8	0.125000	1.302×10^{-1}	3.608×10^{0}	6.850×10^{-10}	6.277×10^{-9}
16	0.062500	3.255×10^{-2}	1.804×10^{0}	3.332×10^{-12}	5.952×10^{-11}
32	0.031250	8.138×10^{-3}	9.021×10^{-1}	2.105×10^{-7}	7.165×10^{-7}
64	0.015625	2.035×10^{-3}	4.511×10^{-1}	1.032×10^{-6}	4.393×10^{-6}
128	0.007812	5.086×10^{-4}	2.255×10^{-1}	9.953×10^{-9}	3.128×10^{-8}
256	0.003906	1.272×10^{-4}	1.128×10^{-1}	1.212×10^{-7}	3.808×10^{-7}

Figure 3.2: Spatial refinement analysis for Prob. 3.1. Results are computed using 1D elements and a spatial refinement factor $r_x = 2$. The formal order of accuracy is shown for each plot. Results for `EDGE3` are super–convergent and excluded from the plot. *Left plot*: the L_2 norm quantifies convergence of the temperature distribution. *Right plot*: the H_1 norm quantifies convergence of heat flux. *Table*: numerical values used to construct the plots.

Problem 3.2: Plate with temperature dependent thermal conductivity

The thermal conductivity of an infinite plate varies linearly with temperature: $k = k_\ell + \beta(u - u_\ell)$. It is exposed on each side to a constant temperature: $u(0) = u_0$ and $u(\ell) = u_\ell$. The plate is allowed to reach thermal equilibrium and the analytic solution for the temperature distribution is [26, pp.138]

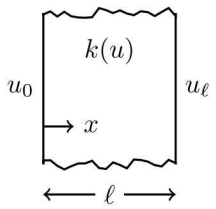

$$u(x) = u_\ell + \left[\frac{k_\ell}{\beta}\sqrt{1 + \beta\frac{(k_0 + k_\ell)}{k_\ell^2}\frac{(\ell - x)}{\ell}(u_0 - u_\ell)} - 1\right]. \qquad (3.4)$$

The problem is run in BISON on the domain $\boldsymbol{X} \in [0, 1]$. Dirichlet boundary conditions are applied: $u(0) = u_0 = 300\,\mathrm{K}$ and $u(1) = u_\ell = 0\,\mathrm{K}$. Steady state heat conduction is considered using a nonlinear thermal conductivity, where $k_\ell = 5\,\mathrm{W/m/K}$. The nonlinearity of the problem is quantified by the variable β; the analytic solution as a function of β is shown in Fig. 3.3. Two cases are examined in this study: (I) $\beta = 0.001$ and (II) $\beta = 0.1$.

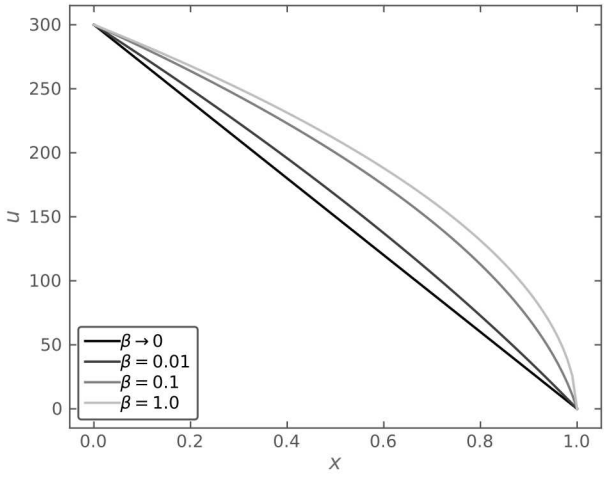

Figure 3.3: The exact solution of Prob. 3.2 as a function of space and β

Case I ($\beta = 0.001$): The exact and computed solutions are shown in Fig. 3.4a for four different meshes and two FE types (linear: `EDGE2`; quadratic: `EDGE3`). A convergence study is conducted with a refinement factor of two (i.e., $r_x = 2$). The computed norms for each element type are plotted and tabulated in Fig. 3.5. The formal order of accuracy is two for linear FEs and three for quadratic FEs. In the asymptotic region, the linear and quadratic FE solutions converge to the exact solution with the correct order of accuracy.

Case II ($\beta = 0.1$): The exact and computed solutions are shown in Fig. 3.4b for four different meshes and two FE types (linear: `EDGE2`; quadratic: `EDGE3`). A convergence study is conducted with a refinement factor of two (i.e., $r_x = 2$). The computed norms for each element type are plotted and tabulated in Fig. 3.6. The formal order of accuracy is two for linear FEs and three for quadratic FEs. In the asymptotic region, the linear and quadratic FE solutions converge to the exact solution with the correct order of accuracy.

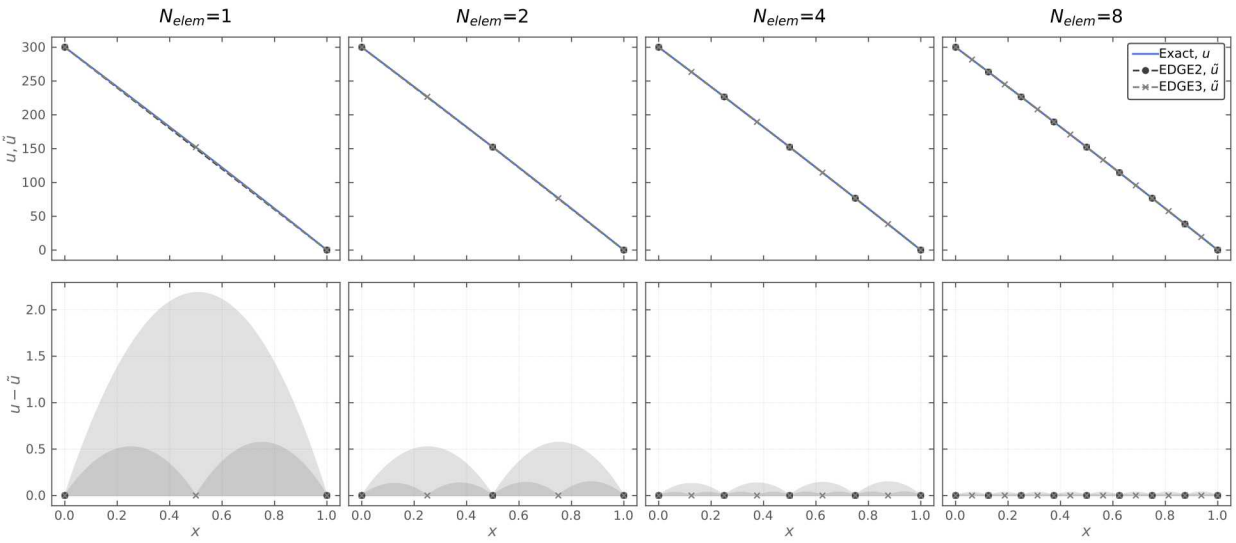

(a) Case I, $\beta = 0.001$

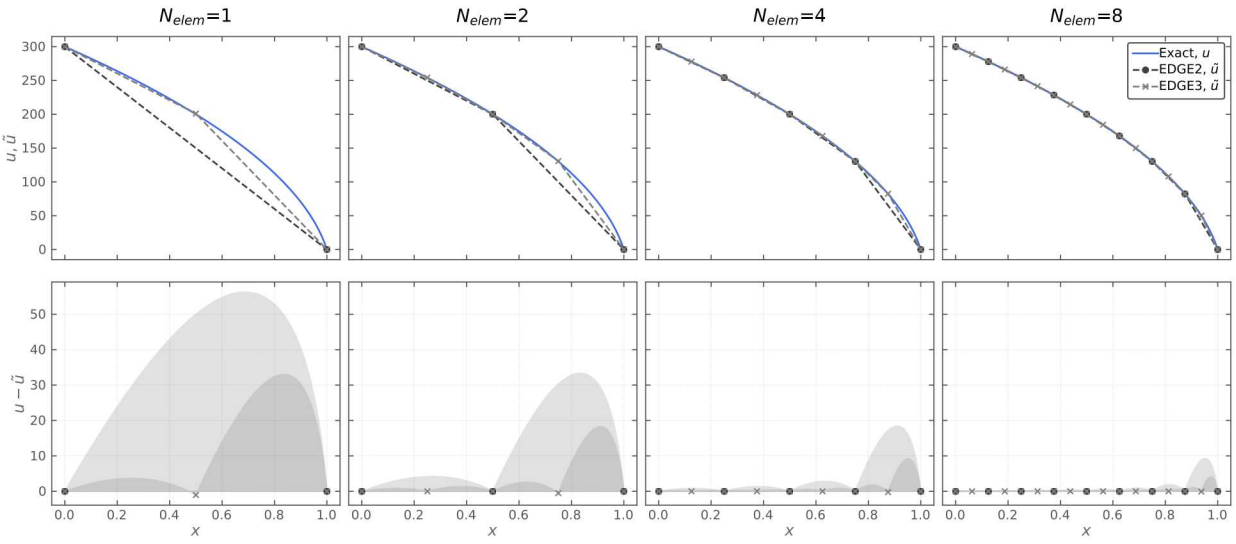

(b) Case II, $\beta = 0.1$

Figure 3.4: Temperature distribution and residuals for Prob. 3.2. Results are shown for the first four meshes. *First row*: exact and FE solutions using 1D elements. *Second row*: residuals between the exact and computed solutions.

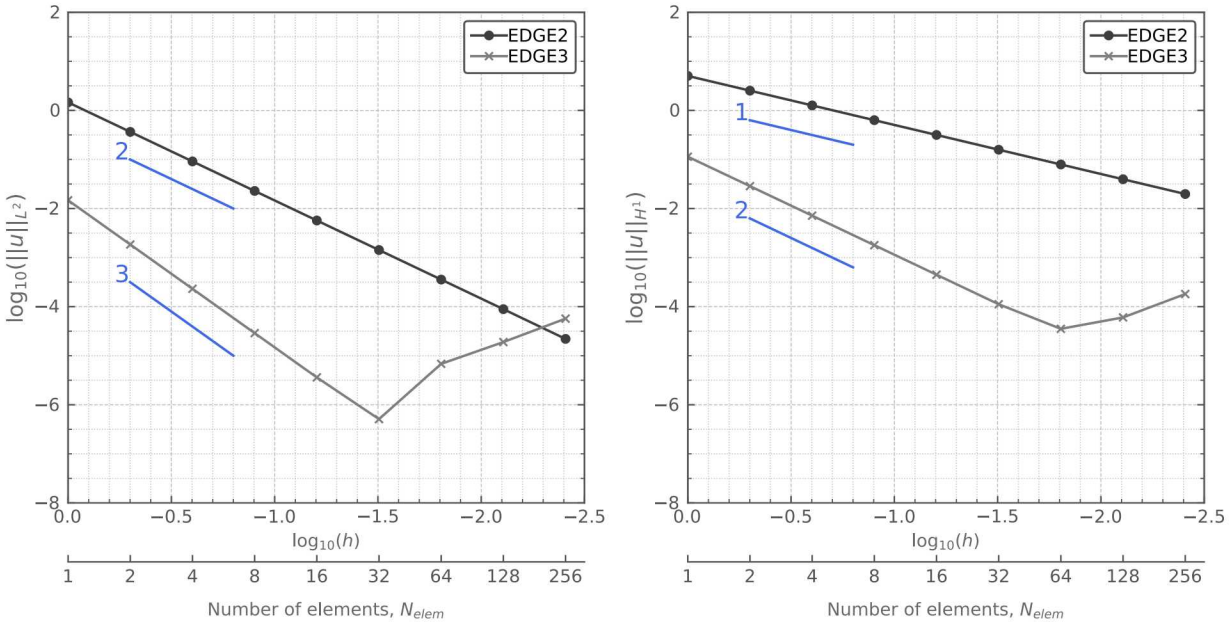

No. Elems	h	**Linear** ($p=1$) $\|\|u\|\|_{L_2}$	**Linear** ($p=1$) $\|\|u\|\|_{H_1}$	**Quadratic** ($p=2$) $\|\|u\|\|_{L_2}$	**Quadratic** ($p=2$) $\|\|u\|\|_{H_1}$
		elem_type=EDGE2		elem_type=EDGE3	
1	1.000000	1.457×10^{0}	5.042×10^{0}	1.470×10^{-2}	1.137×10^{-1}
2	0.500000	3.647×10^{-1}	2.526×10^{0}	1.846×10^{-3}	2.859×10^{-2}
4	0.250000	9.120×10^{-2}	1.264×10^{0}	2.310×10^{-4}	7.156×10^{-3}
8	0.125000	2.280×10^{-2}	6.319×10^{-1}	2.888×10^{-5}	1.790×10^{-3}
16	0.062500	5.701×10^{-3}	3.160×10^{-1}	3.610×10^{-6}	4.470×10^{-4}
32	0.031250	1.425×10^{-3}	1.580×10^{-1}	5.097×10^{-7}	1.120×10^{-4}
64	0.015625	3.560×10^{-4}	7.899×10^{-2}	6.827×10^{-6}	3.500×10^{-6}
128	0.007812	8.881×10^{-5}	3.950×10^{-2}	1.896×10^{-5}	6.000×10^{-5}
256	0.003906	2.200×10^{-5}	1.975×10^{-2}	5.694×10^{-5}	1.810×10^{-4}

Figure 3.5: Spatial refinement analysis for Prob. 3.2 (Case I, $\beta = 0.001$). Results are computed using 1D elements and a spatial refinement factor $r_x = 2$. The formal order of accuracy is shown for each plot. *Left plot*: the L_2 norm quantifies convergence of the temperature distribution. *Right plot*: the H_1 norm quantifies convergence of the heat flux. *Table*: numerical values used to construct the plots.

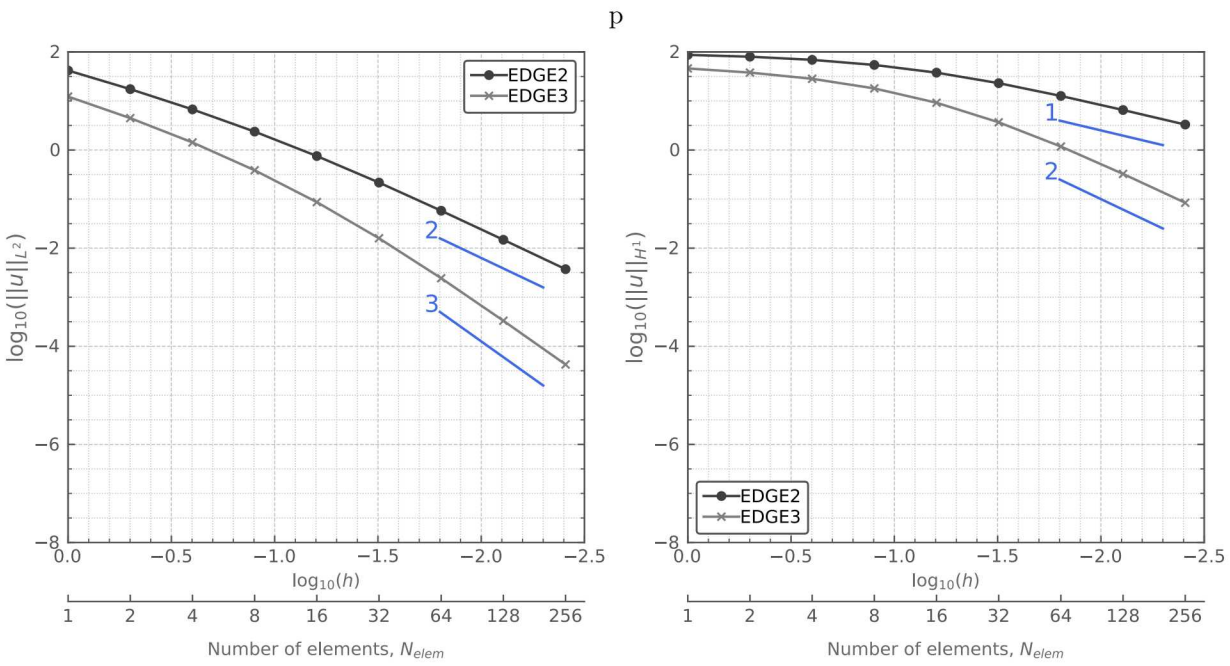

No. Elems	h	**Linear** ($p = 1$) $\|\|u\|\|_{L_2}$	**Linear** ($p = 1$) $\|\|u\|\|_{H_1}$	**Quadratic** ($p = 2$) $\|\|u\|\|_{L_2}$	**Quadratic** ($p = 2$) $\|\|u\|\|_{H_1}$
		elem_type=EDGE2		elem_type=EDGE3	
1	1.000000	4.179×10^{1}	8.687×10^{1}	1.229×10^{1}	4.595×10^{1}
2	0.500000	1.741×10^{1}	7.983×10^{1}	4.466×10^{0}	3.788×10^{1}
4	0.250000	6.728×10^{0}	6.889×10^{1}	1.426×10^{0}	2.833×10^{1}
8	0.125000	2.372×10^{0}	5.423×10^{1}	3.869×10^{-1}	1.802×10^{1}
16	0.062500	7.541×10^{-1}	3.777×10^{1}	8.670×10^{-2}	9.197×10^{0}
32	0.031250	2.171×10^{-1}	2.305×10^{1}	1.590×10^{-2}	3.674×10^{0}
64	0.015625	5.790×10^{-2}	1.265×10^{1}	2.437×10^{-3}	1.178×10^{0}
128	0.007812	1.481×10^{-2}	6.541×10^{0}	3.310×10^{-4}	3.258×10^{-1}
256	0.003906	3.728×10^{-3}	3.303×10^{0}	4.300×10^{-5}	8.411×10^{-2}

Figure 3.6: Spatial refinement analysis for Prob. 3.2 (Case II, $\beta = 0.1$). Results are computed using 1D elements and a spatial refinement factor $r_x = 2$. The formal order of accuracy is shown for each plot. *Left plot*: the L_2 norm quantifies the convergence of the temperature distribution. *Right plot*: the H_1 norm quantifies the convergence of heat flux. *Table*: numerical values used to construct the plots.

Problem 3.3: Plate with temperature dependent thermal conductivity and internal heating

The thermal conductivity of an infinite plate varies linearly with temperature: $k = k_\ell(1+\beta u)$. It has a constant internal heat generation and is exponsed on each side to a constant temperature: $u(0) = u_0$ and $u(\ell) = u_\ell$. The plate is allowed to reach thermal equilibrium and the analytic solution for the temperature distribution is [27, pages 129–132]

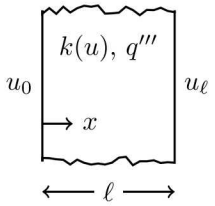

$$u(x) = u_\ell + \frac{1}{\beta}\left[\sqrt{1+\left(\frac{\beta q'''\ell^2}{k_\ell}\right)\left(1-\left(\frac{x}{\ell}\right)^2\right)} - 1\right]. \qquad (3.5)$$

The problem is run in BISON on the domain $\boldsymbol{X} \in [0,1]$. A Neumann boundary condition is applied to the left face and Dirichlet to the right: $(du/dx)_{x=0} = 0$ and $u(1) = u_\ell = 0\,\mathrm{K}$. Steady state conduction is considered using a nonlinear thermal conductivity, where $k_\ell = 1\,\mathrm{W/m/K}$. The analytic solution as a function of β is shown in Fig. 3.7. The external heat source is $q''' = 1200\,\mathrm{W/m^3}$. Two cases are examined: (I) $\beta = 0.001$ and (II) $\beta = 0.1$.

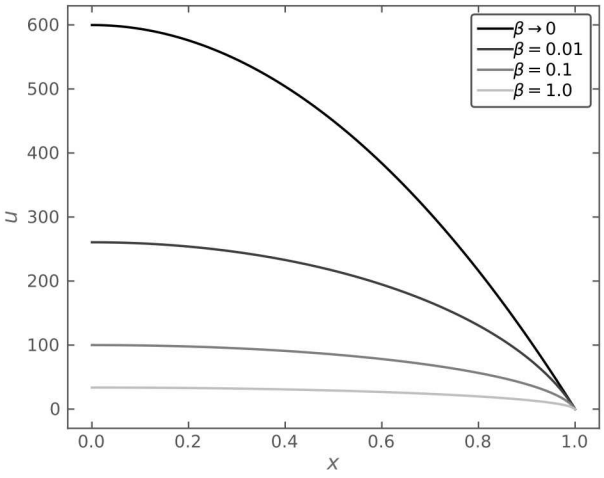

Figure 3.7: The exact solution of Prob. 3.3 as a function of space and β

Case I ($\beta = 0.001$): The exact and computed solutions are shown in Fig. 3.8a for four different meshes and two FE types (linear: `EDGE2`; quadratic: `EDGE3`). A convergence study is conducted with a refinement factor of two (i.e., $r_x = 2$). The computed norms for each element type are plotted and tabulated in Fig. 3.9. The formal order of accuracy is two for linear FEs and three for quadratic FEs. In the asymptotic region, the linear and quadratic FE solutions converge to the exact solution with the correct order of accuracy.

Case II ($\beta = 0.1$): The exact and computed solutions are shown in Fig. 3.8b for four different meshes and two FE types (linear: `EDGE2`; quadratic: `EDGE3`). A convergence study is conducted with a refinement factor of two (i.e., $r_x = 2$). The computed norms for each element type are plotted and tabulated in Fig. 3.10. The formal order of accuracy is two for linear FEs and three for quadratic FEs. In the asymptotic region, the linear and quadratic FE solutions converge to the exact solution with the correct order of accuracy.

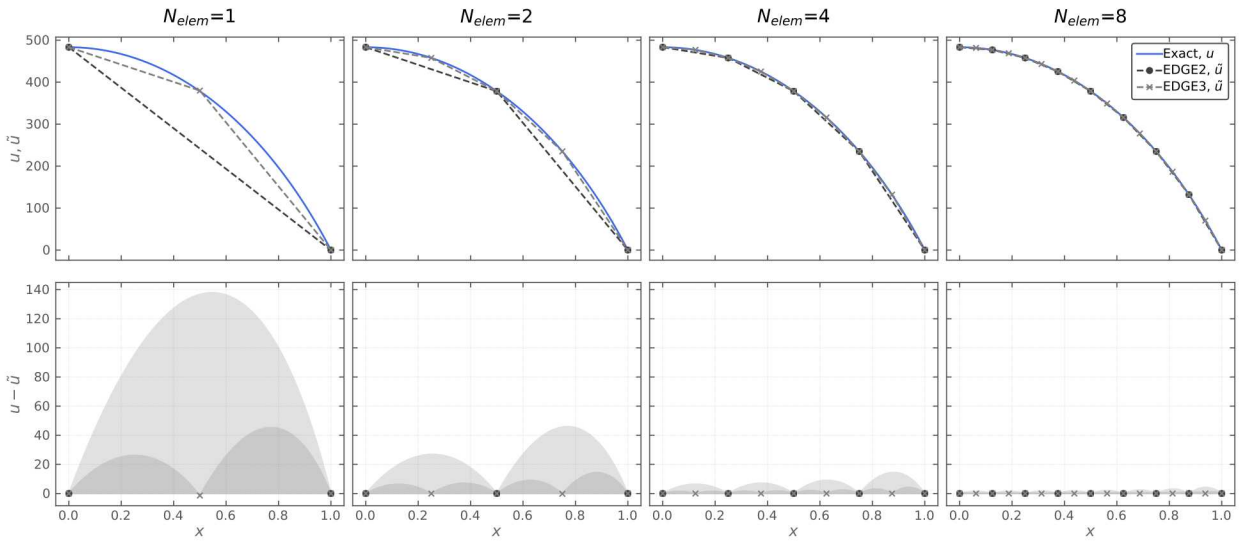

(a) Case I, $\beta = 0.001$

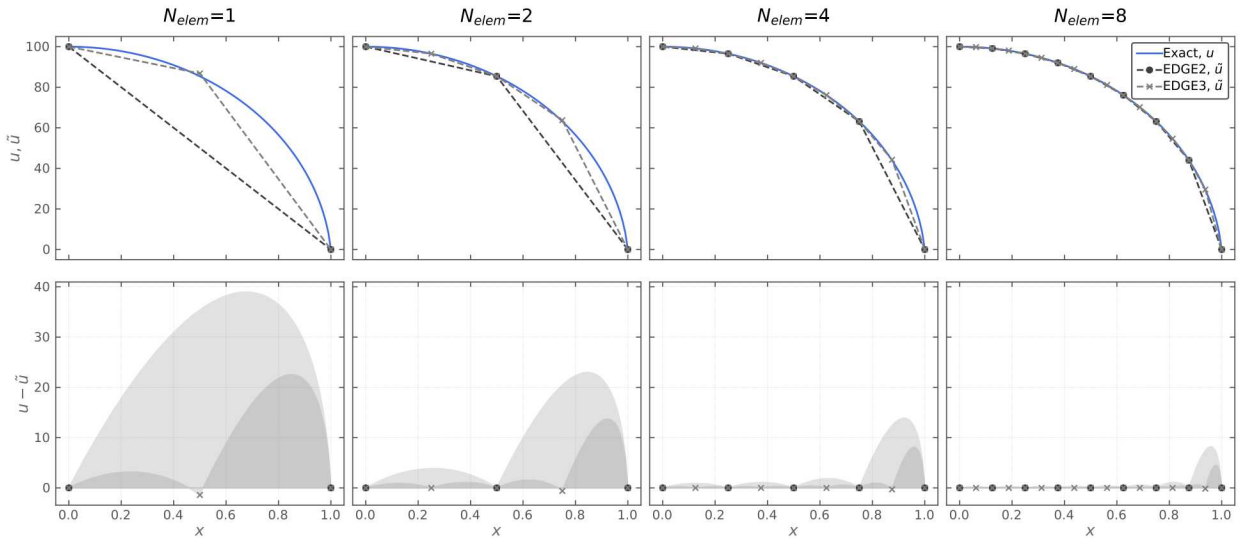

(b) Case II, $\beta = 0.1$

Figure 3.8: Temperature distribution and residuals for Prob. 3.3. Results are shown for the first four meshes. *First row*: exact and FE solutions using 1D elements. *Second row*: residuals between the exact and computed solutions.

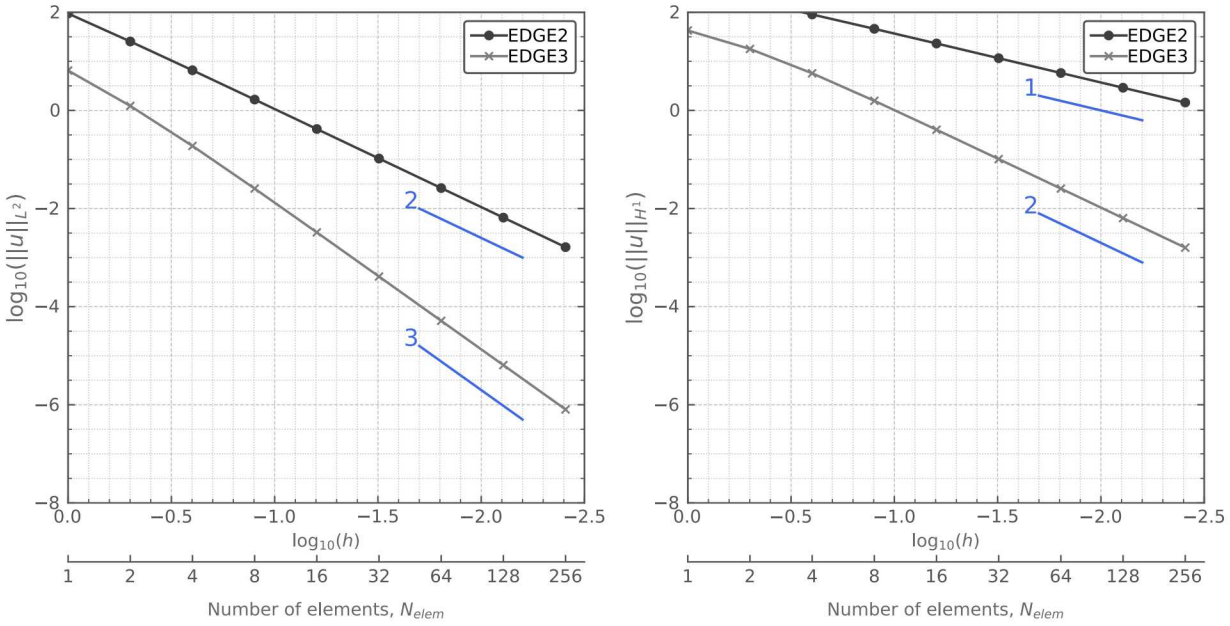

No. Elems	h	**Linear** ($p=1$) $\|\|u\|\|_{L_2}$	**Linear** ($p=1$) $\|\|u\|\|_{H_1}$	**Quadratic** ($p=2$) $\|\|u\|\|_{L_2}$	**Quadratic** ($p=2$) $\|\|u\|\|_{H_1}$
		elem_type=EDGE2		elem_type=EDGE3	
1	1.000000	9.425×10^{1}	3.060×10^{2}	6.495×10^{0}	4.257×10^{1}
2	0.500000	2.537×10^{1}	1.711×10^{2}	1.233×10^{0}	1.787×10^{1}
4	0.250000	6.570×10^{0}	9.023×10^{1}	1.885×10^{-1}	5.707×10^{0}
8	0.125000	1.663×10^{0}	4.597×10^{1}	2.548×10^{-2}	1.568×10^{0}
16	0.062500	4.172×10^{-1}	2.311×10^{1}	3.263×10^{-3}	4.037×10^{-1}
32	0.031250	1.044×10^{-1}	1.157×10^{1}	4.106×10^{-4}	1.017×10^{-1}
64	0.015625	2.611×10^{-2}	5.788×10^{0}	5.141×10^{-5}	2.548×10^{-2}
128	0.007812	6.527×10^{-3}	2.894×10^{0}	6.429×10^{-6}	6.374×10^{-3}
256	0.003906	1.632×10^{-3}	1.447×10^{0}	8.037×10^{-7}	1.594×10^{-3}

Figure 3.9: Spatial refinement analysis for Prob. 3.3 (Case I, $\beta = 0.001$). Results are computed using 1D elements and a spatial refinement factor $r_x = 2$. The formal order of accuracy is shown for each plot. *Left plot*: the L_2 norm quantifies convergence of the temperature distribution. *Right plot*: the H_1 norm quantifies convergence of the heat flux. *Table*: numerical values used to construct the plots.

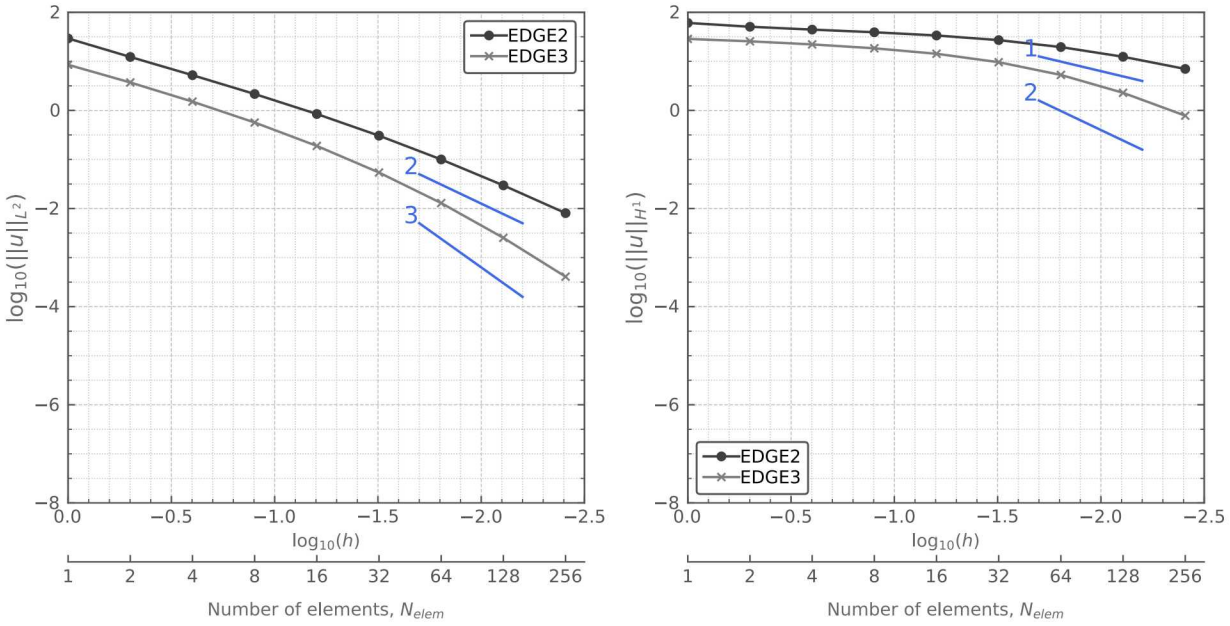

No. Elems	h	**Linear** ($p=1$) $\|\|u\|\|_{L_2}$	**Linear** ($p=1$) $\|\|u\|\|_{H_1}$	**Quadratic** ($p=2$) $\|\|u\|\|_{L_2}$	**Quadratic** ($p=2$) $\|\|u\|\|_{H_1}$
		elem_type=EDGE2		elem_type=EDGE3	
1	1.000000	2.928×10^{1}	6.067×10^{1}	8.514×10^{0}	2.864×10^{1}
2	0.500000	1.229×10^{1}	5.067×10^{1}	3.706×10^{0}	2.558×10^{1}
4	0.250000	5.220×10^{0}	4.432×10^{1}	1.511×10^{0}	2.212×10^{1}
8	0.125000	2.158×10^{0}	3.914×10^{1}	5.659×10^{-1}	1.843×10^{1}
16	0.062500	8.444×10^{-1}	3.365×10^{1}	1.888×10^{-1}	1.425×10^{1}
32	0.031250	3.050×10^{-1}	2.705×10^{1}	5.410×10^{-2}	9.597×10^{0}
64	0.015625	9.997×10^{-2}	1.954×10^{1}	1.292×10^{-2}	5.280×10^{0}
128	0.007812	2.962×10^{-2}	1.240×10^{1}	2.525×10^{-3}	2.283×10^{0}
256	0.003906	8.062×10^{-3}	7.001×10^{0}	4.080×10^{-4}	7.809×10^{-1}

Figure 3.10: Spatial refinement analysis for Prob. 3.3 (Case II, $\beta = 0.1$). Results are computed using 1D elements and a spatial refinement factor $r_x = 2$. The formal order of accuracy is shown for each plot. *Left plot*: the L_2 norm quantifies convergence of the temperature distribution. *Right plot*: the H_1 norm quantifies convergence of the heat flux. *Table*: numerical values used to construct the plots.

Problem 3.4: Rectangular adiabatic plate

A two-dimensional thin adiabatic plate has a thermal conductivity $k = 1$ and no external heat source. It is defined on the domain $x \in [0, L]$ and $y \in [0, l]$. It is exposed on each face to an arbitrary temperature: $u(x, l) = f_1(x)$, $u(x, 0) = f_2(x)$, $u(L, y) = g_1(y)$, and $u(0, y) = g_2(y)$. For this specific case, the two-dimensional steady state temperature distribution can be solved analytically as [28, pp.128–131]

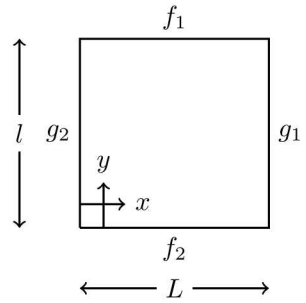

$$u(x, y) = u_{(1)} + u_{(2)} + u_{(3)} + u_{(4)}, \tag{3.6}$$

where

$$u_{(1)} = \frac{2}{L} \sum_{n=1}^{\infty} \frac{\sinh\left(n\pi y/L\right)}{\sinh\left(n\pi l/L\right)} \sin\left(\frac{n\pi x}{L}\right) \int_0^L f_1(x) \sin\left(\frac{n\pi x}{L}\right) dx, \tag{3.7a}$$

$$u_{(2)} = \frac{2}{L} \sum_{n=1}^{\infty} \frac{\sinh\left(n\pi (l-y)/L\right)}{\sinh\left(n\pi l/L\right)} \sin\left(\frac{n\pi x}{L}\right) \int_0^L f_2(x) \sin\left(\frac{n\pi x}{L}\right) dx, \tag{3.7b}$$

$$u_{(3)} = \frac{2}{l} \sum_{n=1}^{\infty} \frac{\sinh\left(n\pi y/l\right)}{\sinh\left(n\pi L/l\right)} \sin\left(\frac{n\pi y}{l}\right) \int_0^l g_1(y) \sin\left(\frac{n\pi y}{l}\right) dy, \tag{3.7c}$$

$$u_{(4)} = \frac{2}{l} \sum_{n=1}^{\infty} \frac{\sinh\left(n\pi (L-x)/l\right)}{\sinh\left(n\pi L/l\right)} \sin\left(\frac{n\pi y}{l}\right) \int_0^l g_2(y) \sin\left(\frac{n\pi y}{l}\right) dy. \tag{3.7d}$$

The top and bottom surfaces are exposed to a constant temperature $f_1(x) = f_2(x) = 1\,\mathrm{K}$. The left and right surfaces are exposed to a constant temperature $g_1(y) = g_2(y) = 0\,\mathrm{K}$. With these specific choices of boundary condition, the solution reduces to

$$\begin{aligned} u(x, y) &= \frac{4}{\pi} \left[\frac{\cosh\left(\frac{\pi}{L}\left[\frac{l}{2} - y\right]\right)}{\cosh\left(\frac{\pi}{2}\frac{l}{L}\right)} \sin\left(\frac{\pi x}{L}\right) + \frac{1}{3} \frac{\cosh\left(\frac{3\pi}{L}\left[\frac{l}{2} - y\right]\right)}{\cosh\left(\frac{3\pi}{2}\frac{l}{L}\right)} \sin\left(\frac{3\pi x}{L}\right) + \ldots \right], \\ &= \frac{4}{\pi} \sum_{i=1}^{N} \frac{1}{(2i-1)} \frac{\cosh\left(\frac{(2i-1)\pi}{L}\left[\frac{l}{2} - y\right]\right)}{\cosh\left(\frac{(2i-1)\pi}{2}\frac{l}{L}\right)} \sin\left(\frac{(2i-1)\pi x}{L}\right). \end{aligned} \tag{3.8}$$

This problem is solved in BISON using the diffusion module on the domain $\boldsymbol{X} \in [0, 1]^2$. Dirichlet boundary conditions are applied to each surface: $f_1(x) = f_2(x) = 1\,\mathrm{K}$ and $g_1(y) = g_2(y) = 0\,\mathrm{K}$. Steady state heat conduction is considered through the homogeneous solid. For comparison to the analytic solution, the first 100 terms of the infinite summation in Eq. 3.8 sufficiently characterize the analytic solution. This approximate analytic solution is shown in Fig. 3.11 on the square domain. The temperature gradually transitions from the hotter temperature at the top and bottom surfaces to the cooler temperature at the left and right surfaces.

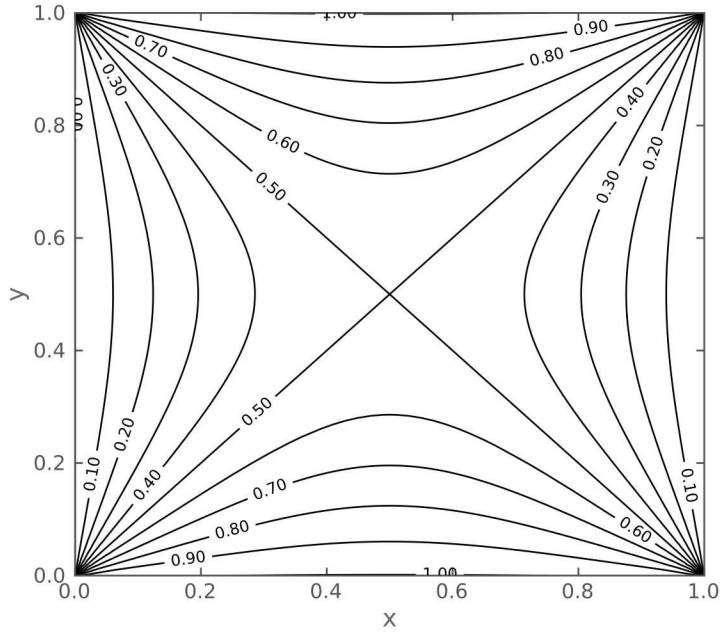

Figure 3.11: Isotherms of the approximate solution of Prob. 3.4 computed using the first 100 terms of Eq. 3.8

Fig. 3.12 shows the convergence of two FE choices as the two-dimensional mesh is refined (`QUAD4` and `TRI3`). The triangular FE results in a solution that more accurately approximates the analytic solution. This is due to shape of the analytic solution, which cannot be easily fit using square elements. In Fig. 3.12, it can also be observed that the largest source of error for both meshes is in the upper right corner. This error is not related to the selection of FE types, but rather is due to the numerical approximation to the mathematical problem. This particular problem is an elliptic boundary value problem (BVP), which is known to have corner singularities in two- or three-dimensional domains [33, 34, 35]. Such singularities can be the result of non-smoothness of the domain (corners, edges, etc.), abrupt changes of a boundary condition from one type to another, or discontinuities in the solution or model coefficients [36]. The singularity is expected to impact the observed order of accuracy [37]; therefore, a convergence plot isn't included for this problem.

Fig. 3.13 shows a comparison of the two-dimensional solutions with 32×32 elements using a variety of FE types (linear: `QUAD4,TRI3`; quadratic: `QUAD8,QUAD9,TRI6`). Regardless of the chosen FE shape, the BISON solution has the correct shape, indicating that each two-dimensional FE option is implemented correctly.

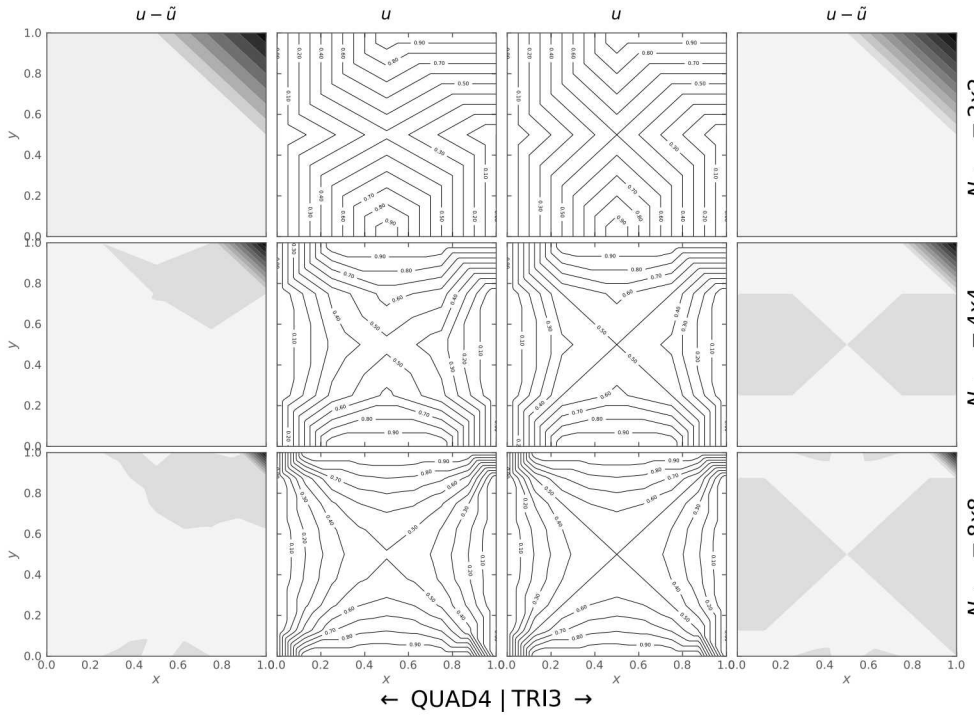

Figure 3.12: Temperature distributions and residuals for Prob. 3.4 with different meshes (left: `QUAD4`; right: `TRI3`). *Center columns*: the FE solutions using a variety of 2D meshes. *Outside columns*: residuals between the approximate solution and the computed solutions, where darker colors indicate a less accurate computed solution.

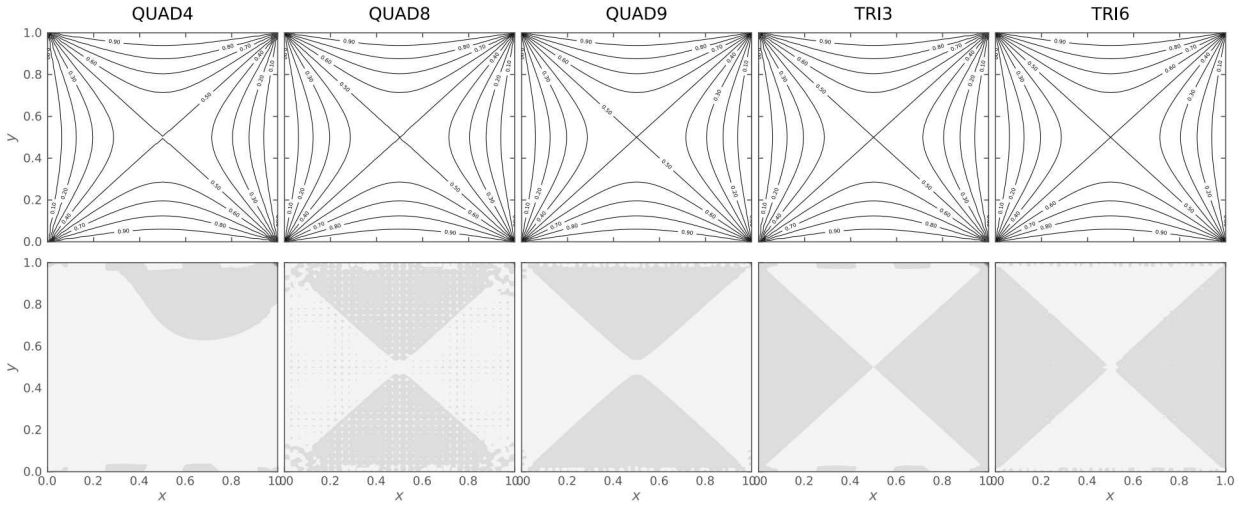

Figure 3.13: Temperature distributions and residuals for Prob. 3.4 with different FE types. Results are shown for five FE types. *First row*: the FE solutions using 32×32 2D elements. *Second row*: residuals between the approximate solution and the computed solutions, where darker colors indicate a less accurate computed solution.

Problem 3.5: Hollow cylinder with Dirichlet boundary conditions

An infinitely long hollow cylinder with inner radius r_i and outer radius r_o has a constant thermal conductivity k. It is allowed to reach thermal equilibrium while being exposed constant temperatures on its inside and outside faces: $u(r_i) = u_i$ and $u(r_o) = u_o$. The analytical solution for the temperature distribution in the cylinder is [26, pp.133]

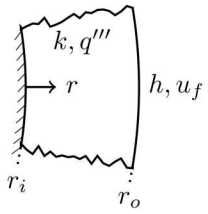

$$u(r) = \frac{u_o \ln(r_i) - u_i \ln(r_o)}{\ln(r_i/r_o)} + \frac{(u_i - u_o)}{\ln(r_i/r_o)} \ln(r). \tag{3.9}$$

The problem is solved in BISON on the domain $\boldsymbol{X} \in [0.2, 1]$ using Dirichlet boundary conditions $u(0.2) = u_i = 300\,\mathrm{K}$ and $u(1) = u_o = 0\,\mathrm{K}$. Steady state heat conduction is considered through the solid with constant thermal conductivity $k = 5\,\mathrm{W/m/K}$. The exact and computed solutions are shown in Fig. 3.14 for four different meshes and two finite element types (linear: `EDGE2`; quadratic: `EDGE3`).

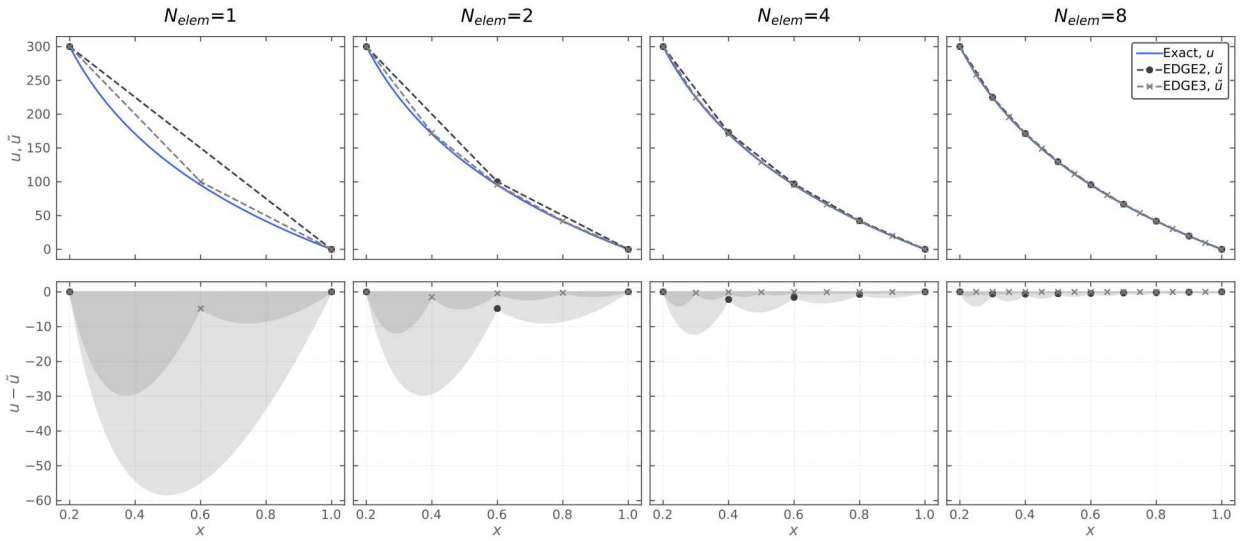

Figure 3.14: Temperature distribution and residuals for Prob. 3.5. Results are shown for the first four meshes. *First row*: exact and FE solutions using 1D elements. *Second row*: residuals between the exact solution and computed solutions.

A convergence study is conducted with a refinement factor of two (i.e., $r_r = 2$). The computed norms for each element type are plotted and tabulated in Fig. 3.15. The formal order of accuracy is two for linear FEs and three for quadratic FEs. In the asymptotic region, the linear and quadratic FE solutions converge to the exact solution with the correct order of accuracy.

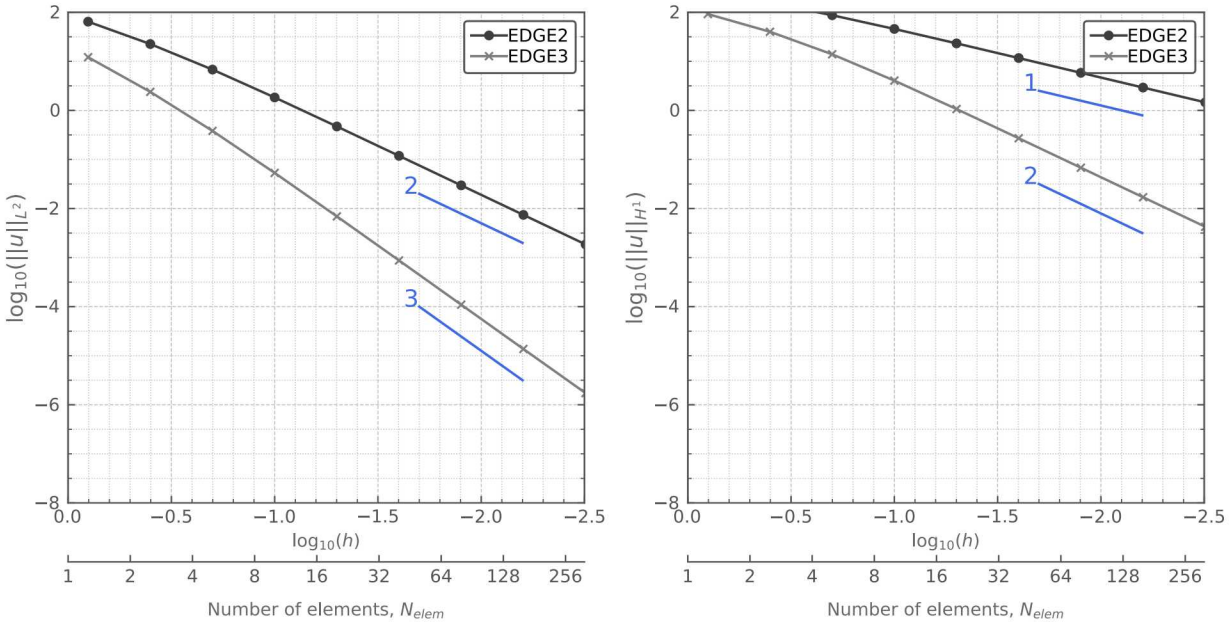

No. Elems	h	**Linear** ($p=1$) $\|\|u\|\|_{L_2}$	**Linear** ($p=1$) $\|\|u\|\|_{H_1}$	**Quadratic** ($p=2$) $\|\|u\|\|_{L_2}$	**Quadratic** ($p=2$) $\|\|u\|\|_{H_1}$
		elem_type=EDGE2		elem_type=EDGE3	
1	0.800000	6.430×10^{1}	2.512×10^{2}	1.212×10^{1}	9.195×10^{1}
2	0.400000	2.252×10^{1}	1.546×10^{2}	2.386×10^{1}	4.007×10^{1}
4	0.200000	6.787×10^{0}	8.703×10^{1}	3.820×10^{-1}	1.392×10^{1}
8	0.100000	1.835×10^{0}	4.572×10^{1}	5.325×10^{-2}	4.045×10^{0}
16	0.050000	4.705×10^{-1}	2.323×10^{1}	6.915×10^{-3}	1.066×10^{0}
32	0.025000	1.184×10^{-1}	1.166×10^{1}	8.740×10^{-4}	2.704×10^{-1}
64	0.012500	2.966×10^{-2}	5.838×10^{0}	1.100×10^{-4}	6.788×10^{-2}
128	0.006250	7.419×10^{-3}	2.920×10^{0}	1.400×10^{-5}	1.699×10^{-2}
256	0.003125	1.855×10^{-3}	1.460×10^{0}	2.000×10^{-6}	4.247×10^{-3}

Figure 3.15: Spatial refinement analysis for Prob. 3.5. Results are computed using 1D elements and a spatial refinement factor ($r_r = 2$). The formal order of accuracy is shown for each plot. *Left plot*: the L_2 norm quantifies convergence of the temperature distribution. *Right plot*: the H_1 norm quantifies convergence of the heat flux. *Table*: numerical values used to construct the plots.

Problem 3.6: Hollow cylinder with temperature dependent thermal conductivity

The thermal conductivity of an infinitely long hollow tube varies linearly with temperature: $k_o = k_o + \beta(u - u_o)$. The tube inside radius is r_i and outside radius is r_o. It is exposed on the inner and outer surfaces to constant temperatures $u(r_i) = u_i$ and $u(r_o) = u_o$. In thermal equilibrium, the analytic solution for the temperature distribution is [26, pp.138]

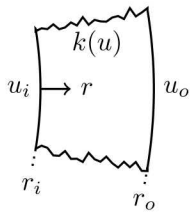

$$u(r) = u_o + \frac{k_o}{\beta}\left[\sqrt{1 + \beta\frac{(k_i + k_o)}{k_o^2}\frac{\ln(r/r_o)}{\ln(r_i/r_o)}(u_i - u_o)} - 1\right]. \qquad (3.10)$$

The problem is solved in BISON on the domain $\boldsymbol{X} \in [0.2, 1]$ using Dirichlet boundary conditions $u(0.2) = u_i = 300\,\mathrm{K}$ and $u(1) = u_o = 0\,\mathrm{K}$. Steady state heat conduction is considered using a nonlinear thermal conductivity where $k_o = 5\,\mathrm{W/m/K}$. The nonlinearity of the problem is quantified by the variable β; the analytic solution as a function of β is shown in Fig. 3.16. Two cases are examined in this study: (I) $\beta = 0.001$ and (III) $\beta = 0.1$.

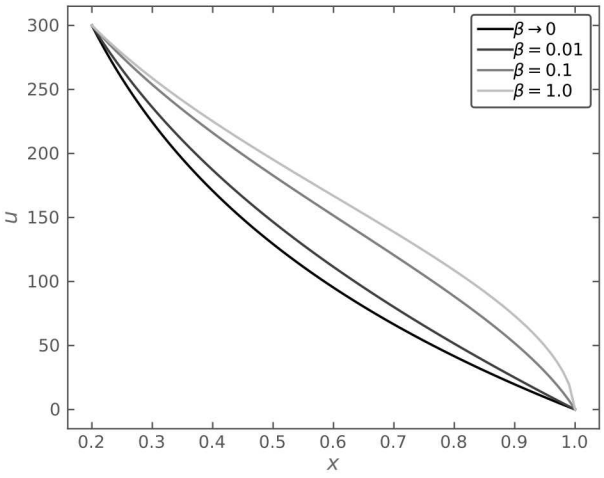

Figure 3.16: The exact solution, $u = u(r)$ in response to varied β term.

Case I ($\beta = 0.001$): The exact and computed solutions are shown in Fig. 3.17a for four different meshes and two FE types (linear: `EDGE2`; quadratic: `EDGE3`). A convergence study is conducted with a refinement factor of two (i.e., $r_r = 2$). The computed norms for each element type are plotted and tabulated in Fig. 3.18. The formal order of accuracy is two for linear FEs and three for quadratic FEs. In the asymptotic region, the linear and quadratic FE solutions converge to the exact solution with the correct order of accuracy.

Case II ($\beta = 0.1$): The exact and computed solutions are shown in Fig. 3.17b for four different meshes and two FE types (linear: `EDGE2`; quadratic: `EDGE3`). A convergence study is conducted with a refinement factor of two (i.e., $r_r = 2$). The computed norms for each element type are plotted and tabulated in Fig. 3.19. The formal order of accuracy is two for linear FEs and three for quadratic FEs. In the asymptotic region, the linear and quadratic FE solutions converge to the exact solution with the correct order of accuracy.

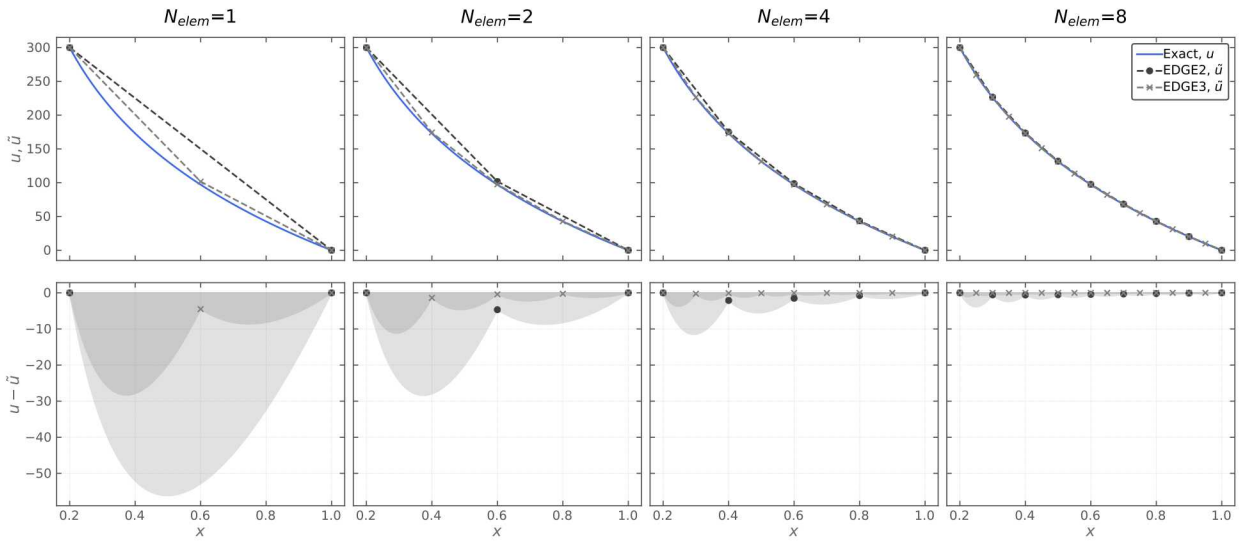

(a) Case I, $\beta = 0.001$

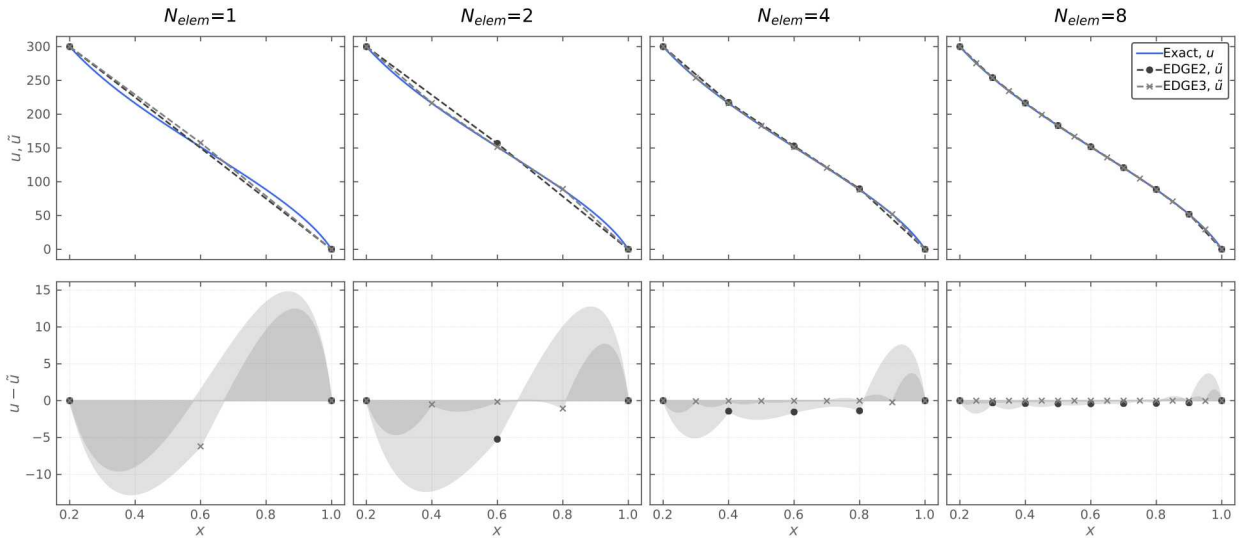

(b) Case II, $\beta = 0.1$

Figure 3.17: Temperature distribution and residuals for Prob. 3.6. Results are shown for the first four meshes. *First row*: exact and FE solutions using 1D elements. *Second row*: residuals between the exact and computed solutions.

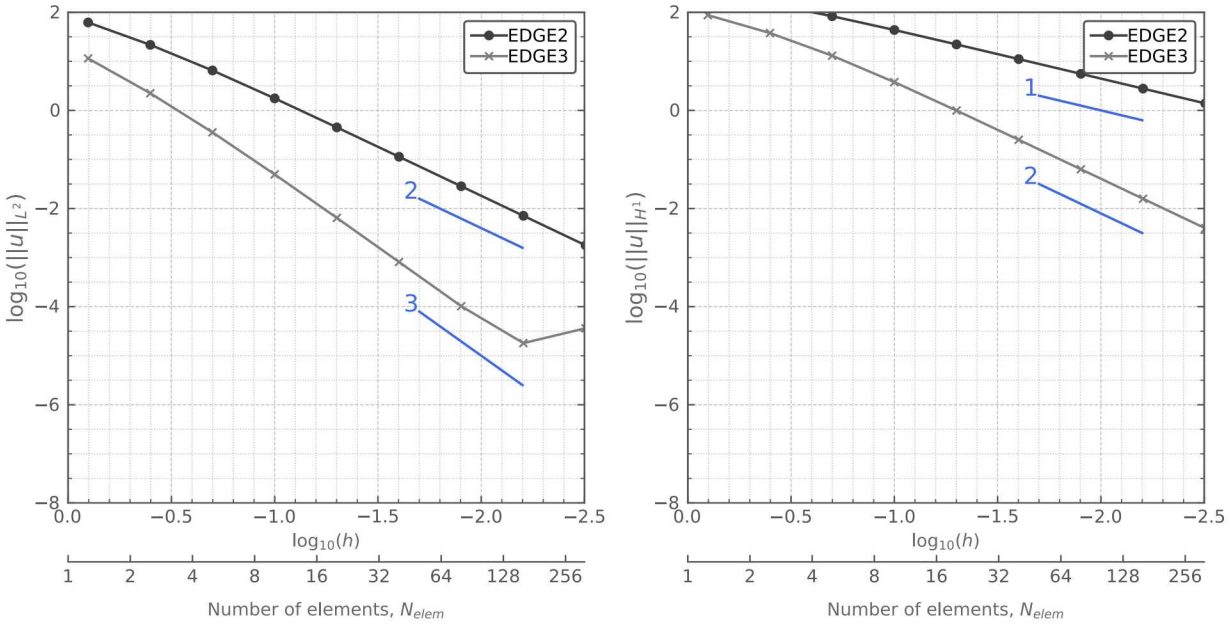

No. Elems	h	**Linear** ($p=1$) $\|\|u\|\|_{L_2}$	**Linear** ($p=1$) $\|\|u\|\|_{H_1}$	**Quadratic** ($p=2$) $\|\|u\|\|_{L_2}$	**Quadratic** ($p=2$) $\|\|u\|\|_{H_1}$
		elem_type=EDGE2		elem_type=EDGE3	
1	0.800000	6.195×10^{1}	2.430×10^{2}	1.146×10^{1}	8.740×10^{1}
2	0.400000	2.166×10^{1}	1.484×10^{1}	2.237×10^{0}	3.773×10^{1}
4	0.200000	6.513×10^{0}	8.313×10^{1}	3.568×10^{-1}	1.302×10^{1}
8	0.100000	1.758×10^{0}	4.357×10^{1}	4.963×10^{-2}	3.772×10^{0}
16	0.050000	4.507×10^{-1}	2.212×10^{1}	6.439×10^{-3}	9.924×10^{-1}
32	0.025000	1.134×10^{-1}	1.110×10^{1}	8.140×10^{-4}	2.518×10^{-1}
64	0.012500	2.841×10^{-2}	5.558×10^{0}	1.020×10^{-4}	6.318×10^{-2}
128	0.006250	7.106×10^{-3}	2.780×10^{0}	1.800×10^{-5}	1.581×10^{-2}
256	0.003125	1.777×10^{-3}	1.390×10^{0}	3.600×10^{-5}	3.956×10^{-3}

Figure 3.18: Spatial refinement analysis for Prob. 3.6 (Case I, $\beta = 0.001$). Results are computed using 1D elements and a spatial refinement factor $r_r = 2$. The formal order of accuracy is shown for each plot. *Left plot*: the L_2 norm quantifies convergence of the temperature distribution. *Right plot*: the H_1 norm quantifies convergence of the heat flux. *Table*: numerical values used to construct the plots.

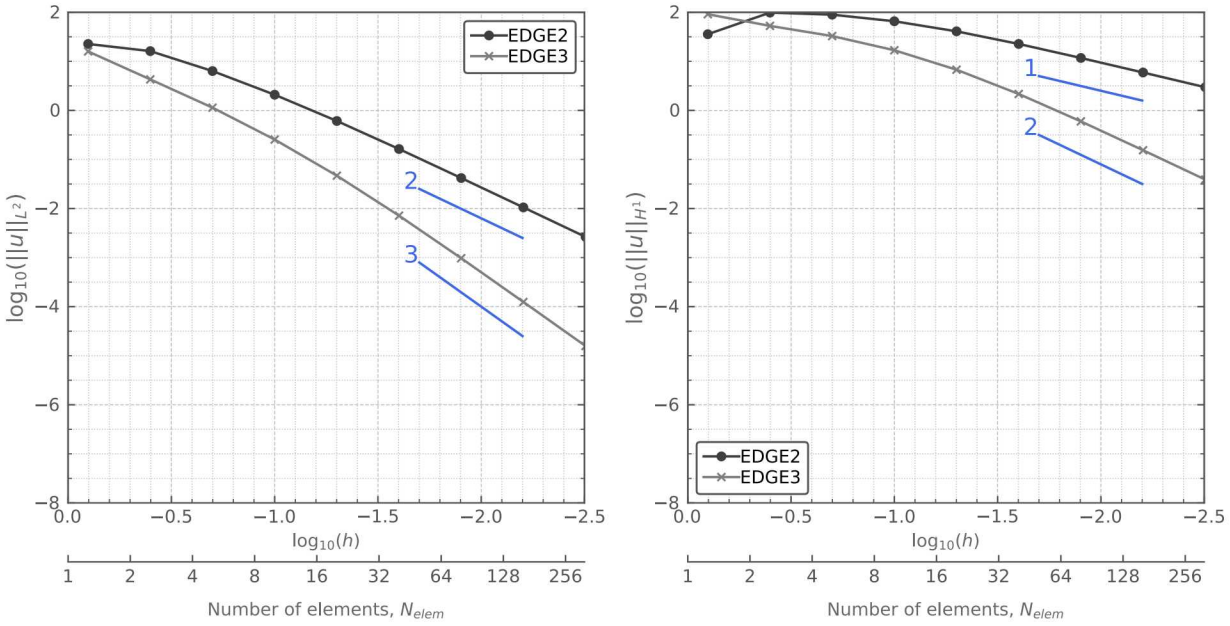

No. Elems	h	**Linear** ($p = 1$) $\|\|u\|\|_{L_2}$	**Linear** ($p = 1$) $\|\|u\|\|_{H_1}$	**Quadratic** ($p = 2$) $\|\|u\|\|_{L_2}$	**Quadratic** ($p = 2$) $\|\|u\|\|_{H_1}$
		elem_type=EDGE2		elem_type=EDGE3	
1	0.800000	2.258×10^{1}	3.570×10^{1}	1.592×10^{1}	9.123×10^{1}
2	0.400000	1.615×10^{1}	9.836×10^{1}	4.283×10^{0}	5.276×10^{1}
4	0.200000	6.337×10^{0}	8.935×10^{1}	1.137×10^{0}	3.275×10^{1}
8	0.100000	2.087×10^{0}	6.556×10^{1}	2.547×10^{-1}	1.682×10^{1}
16	0.050000	6.088×10^{-1}	4.086×10^{1}	4.671×10^{-2}	6.743×10^{0}
32	0.025000	1.632×10^{-1}	2.260×10^{1}	7.154×10^{-3}	2.161×10^{0}
64	0.012500	4.182×10^{-2}	1.171×10^{1}	9.710×10^{-4}	5.972×10^{-1}
128	0.006250	1.053×10^{-2}	5.916×10^{0}	1.250×10^{-4}	1.541×10^{-1}
256	0.003125	2.638×10^{-3}	2.966×10^{0}	1.600×10^{-5}	3.885×10^{-2}

Figure 3.19: Spatial refinement analysis for Prob. 3.6 (Case I, $\beta = 0.001$). Results are computed using 1D elements and a spatial refinement factor $r_r = 2$. The formal order of accuracy is shown for each plot. *Left plot*: the L_2 norm quantifies convergence of the temperature distribution. *Right plot*: the H_1 norm quantifies convergence of the heat flux. *Table*: numerical values used to construct the plots.

Problem 3.7: Hollow cylinder with temperature dependent thermal conductivity and internal heating

The thermal conductivity of an infinitely long hollow cylinder varies linearly with temperature: $k = k_0(1 + \beta u)$. The tube inside radius is r_i and outside radius is r_o. It has a constant internal heat generation q''' and is exposed to a constant temperature on both surfaces: $u(r_i) = u_i$ and $u(r_o) = u_o$. If the cylinder reaches thermal equilibrium, the analytic solution for the temperature distribution is [28, pp.194]

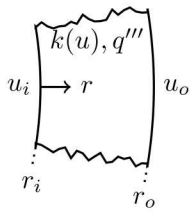

$$u(r) = u_0 + \frac{1}{\beta}\left(\sqrt{1 + \frac{q'''\beta}{2k_0}\left[(r_o^2 - r^2) - \frac{(r_o^2 - r_i^2)}{\ln(r_o/r_i)}\ln\left(\frac{r_o}{r}\right)\right]} - 1\right). \quad (3.11)$$

The problem is solved in BISON on the domain $\boldsymbol{X} \in [0.2, 1]$ using Dirichlet boundary conditions $u(0.2) = u_i = 0\,\mathrm{K}$ and $u(1) = u_o = 0\,\mathrm{K}$. Steady state heat conduction is considered using a non-linear thermal conductivity where $k_o = 1\,\mathrm{W/m/K}$. The nonlinearity of the problem is quantified by the variable β; the analytic solution as a function of β is shown in Fig. 3.20. Two cases are examined in this study: (I) $\beta = 0.001$ and (III) $\beta = 0.1$.

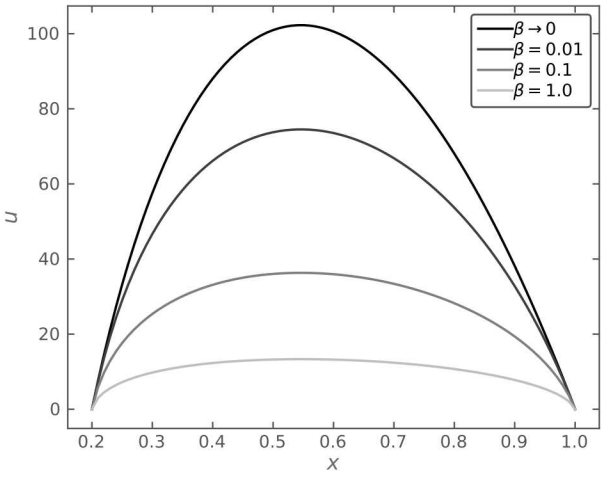

Figure 3.20: The exact solution of Prob. 3.7 as a function of space and time

Case I ($\beta = 0.001$): The exact and computed solutions are shown in Fig. 3.21a for four different meshes and two FE types (linear: `EDGE2`; quadratic: `EDGE3`). A convergence study is conducted with a refinement factor of two (i.e., $r_r = 2$). The computed norms for each element type are plotted and tabulated in Fig. 3.22. The formal order of accuracy is two for linear FEs and three for quadratic FEs. In the asymptotic region, the linear and quadratic FE solutions converge to the exact solution with the correct order of accuracy.

Case II ($\beta = 0.1$): The exact and computed solutions are shown in Fig. 3.21b for four different meshes and two FE types (linear: `EDGE2`; quadratic: `EDGE3`). A convergence study is conducted with a refinement factor of two (i.e., $r_r = 2$). The computed norms for each element type are plotted and tabulated in Fig. 3.23. The formal order of accuracy is two for linear FEs and three for quadratic FEs. In the asymptotic region, the linear and quadratic FE solutions converge to the exact solution with the correct order of accuracy.

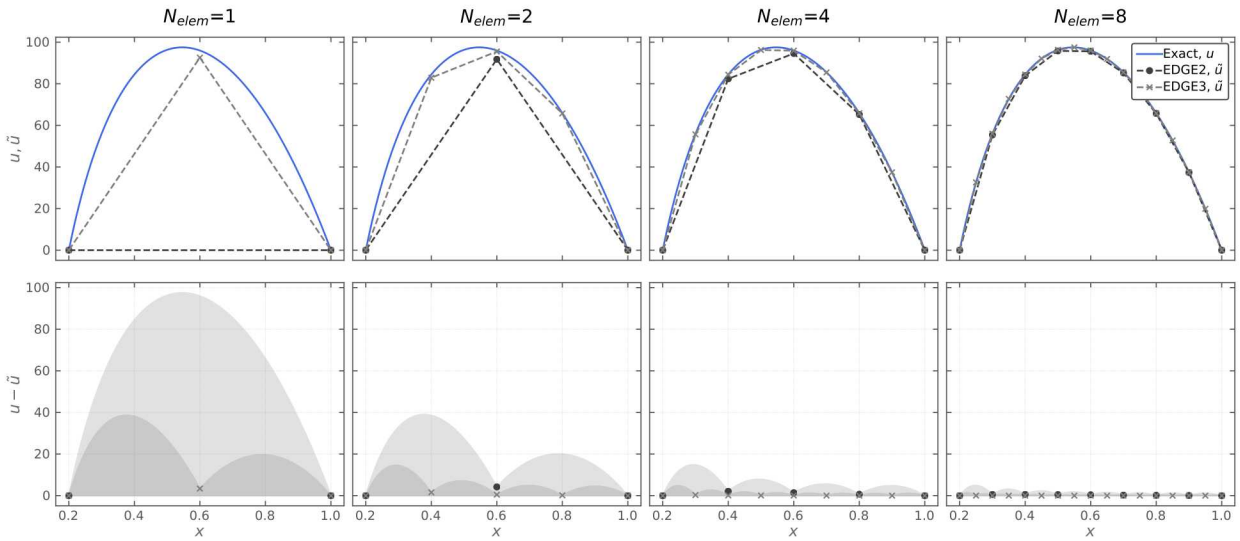

(a) Case I, $\beta = 0.001$

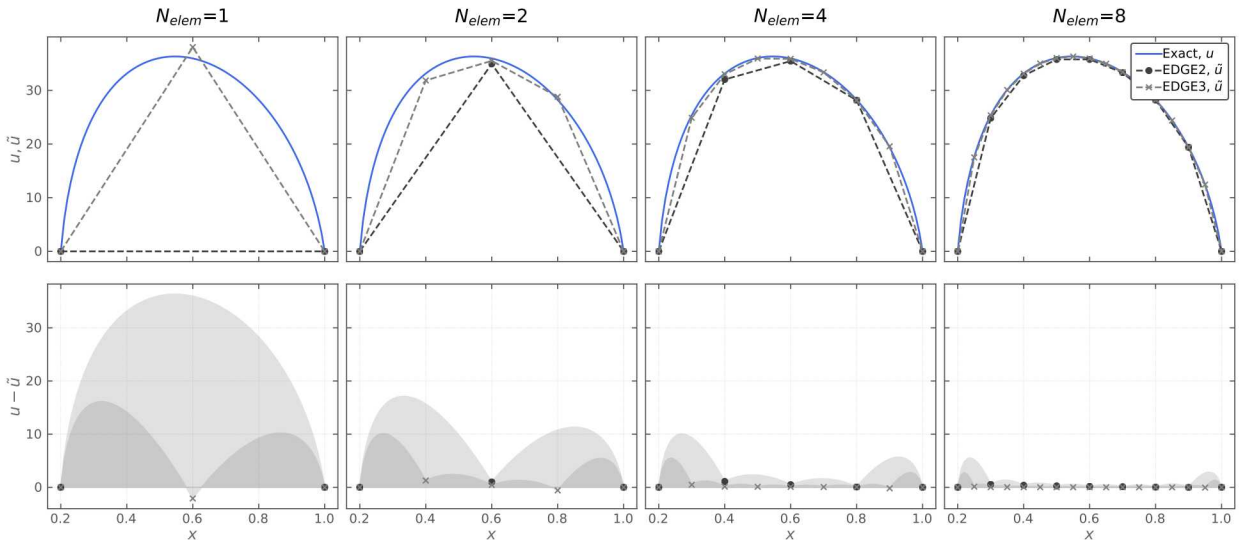

(b) Case II, $\beta = 0.1$

Figure 3.21: Temperature distribution and residuals for Prob. 3.7. Results are shown for the first four meshes. *First row*: exact and FE solutions using 1D elements. *Second row*: residuals between the exact and computed solutions.

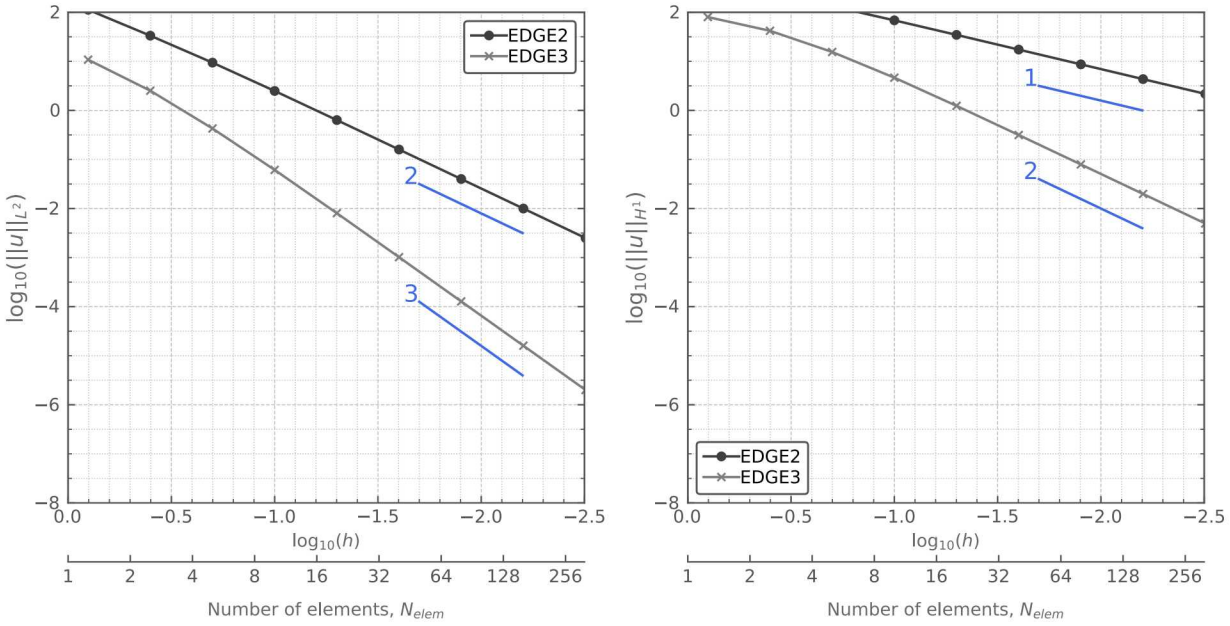

No. Elems	h	**Linear** ($p=1$) $\|\|u\|\|_{L^2}$	**Linear** ($p=1$) $\|\|u\|\|_{H^1}$	**Quadratic** ($p=2$) $\|\|u\|\|_{L^2}$	**Quadratic** ($p=2$) $\|\|u\|\|_{H^1}$
		elem_type=EDGE2		elem_type=EDGE3	
1	0.800000	1.124×10^{2}	4.528×10^{2}	1.080×10^{1}	7.985×10^{1}
2	0.400000	3.333×10^{1}	2.491×10^{2}	2.518×10^{0}	4.191×10^{1}
4	0.200000	9.404×10^{0}	1.328×10^{2}	4.281×10^{-1}	1.550×10^{1}
8	0.100000	2.489×10^{0}	6.848×10^{1}	6.123×10^{-2}	4.640×10^{0}
16	0.050000	6.344×10^{-1}	3.460×10^{1}	8.033×10^{-3}	1.237×10^{0}
32	0.025000	1.595×10^{-1}	1.735×10^{1}	1.019×10^{-3}	3.151×10^{-1}
64	0.012500	3.992×10^{-2}	8.681×10^{0}	1.280×10^{-4}	7.917×10^{-2}
128	0.006250	9.984×10^{-3}	4.341×10^{0}	1.600×10^{-5}	1.982×10^{-2}
256	0.003125	2.496×10^{-3}	2.171×10^{0}	2.000×10^{-6}	4.956×10^{-3}

Figure 3.22: Spatial refinement analysis for Prob. 3.7 (Case I, $\beta = 0.001$). Results are computed using 1D elements and a spatial refinement factor $r_r = 2$. The formal order of accuracy is shown for each plot. *Left plot*: the L_2 norm quantifies convergence of the temperature distribution. *Right plot*: the H_1 norm quantifies convergence of the heat flux. *Table*: numerical values used to construct the plots.

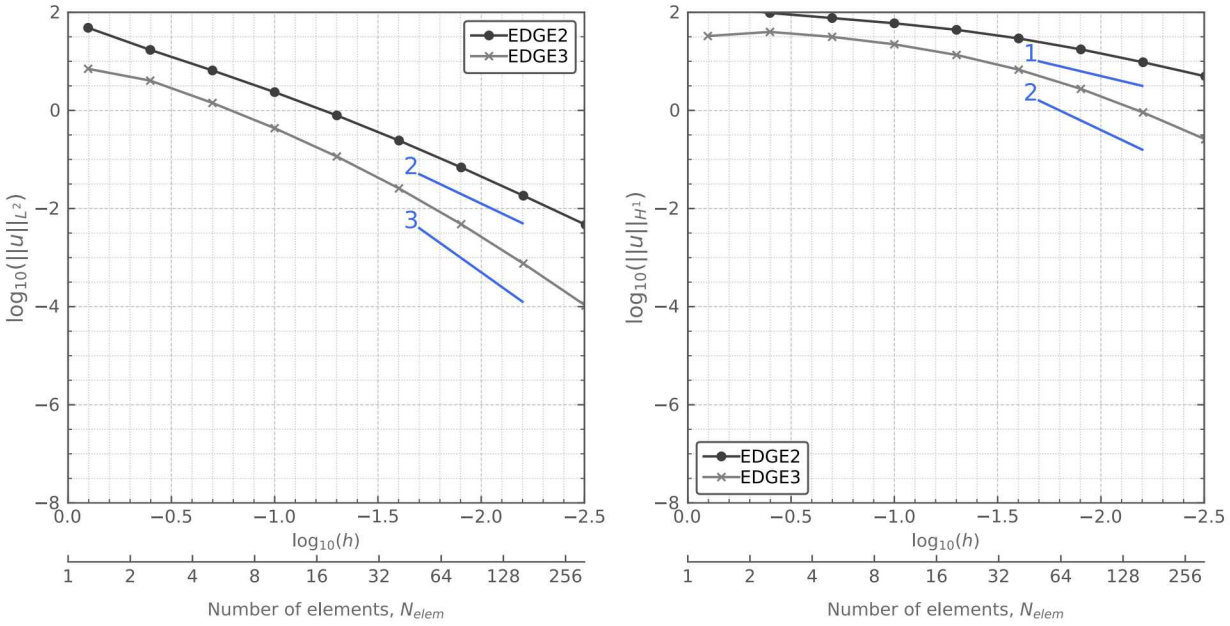

No. Elems	h	**Linear** ($p = 1$) $\|\|u\|\|_{L_2}$	**Linear** ($p = 1$) $\|\|u\|\|_{H_1}$	**Quadratic** ($p = 2$) $\|\|u\|\|_{L_2}$	**Quadratic** ($p = 2$) $\|\|u\|\|_{H_1}$
		elem_type=EDGE2		elem_type=EDGE3	
1	0.800000	4.822×10^{1}	1.292×10^{2}	7.034×10^{0}	3.279×10^{1}
2	0.400000	1.711×10^{1}	9.679×10^{1}	4.041×10^{0}	3.979×10^{1}
4	0.200000	6.511×10^{0}	7.625×10^{1}	1.418×10^{0}	3.153×10^{1}
8	0.100000	2.356×10^{0}	5.965×10^{1}	4.340×10^{-1}	2.221×10^{1}
16	0.050000	7.896×10^{-1}	4.390×10^{1}	1.148×10^{-1}	1.348×10^{1}
32	0.025000	2.428×10^{-1}	2.930×10^{1}	2.567×10^{-2}	6.763×10^{0}
64	0.012500	6.877×10^{-2}	1.753×10^{1}	4.795×10^{-3}	2.742×10^{0}
128	0.006250	1.826×10^{-2}	9.582×10^{0}	7.560×10^{-4}	9.077×10^{-1}
256	0.003125	4.670×10^{-3}	4.958×10^{0}	1.050×10^{-4}	2.577×10^{-1}

Figure 3.23: Spatial refinement analysis for Prob. 3.7 (Case I, $\beta = 0.001$). Results are computed using 1D elements and a spatial refinement factor $r_r = 2$. The formal order of accuracy is shown for each plot. *Left plot*: the L_2 norm quantifies convergence of the temperature distribution. *Right plot*: the H_1 norm quantifies convergence of the heat flux. *Table*: numerical values used to construct the plots.

Problem 3.8: Hollow cylinder with internal heating and outside convection boundary

An infinitely long hollow cylinder with inner radius r_i and outer radius r_o has thermal conductivity k and internal heat generation q'''. The inside surface is insulated and the outside surface is exposed to a fluid temperature u_f and heat transfer coefficient h. If the cylinder is in thermal equilibrium, the analytic solution for the temperature distribution is [29, p.2-33]

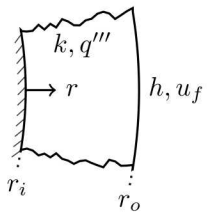

$$u(r) = u_f + \frac{q''' r_o^2}{4k}\left(\frac{2k}{h r_o}\left[1 - r_i^2\right] + 1 - \left(\frac{r}{r_o}\right)^2 + 2r_i^2 \ln\left(\frac{r}{r_o}\right)\right). \quad (3.12)$$

The problem is solved in BISON on the domain $\boldsymbol{X} \in [0.2, 1]$. The boundary conditions are Neumann and convective: $(du/dx)_{r=0.2} = 0$ and $q_o'' = h(u_f - u_o)$. The fluid temperature and heat transfer coefficient are $u_f = 100\,\mathrm{K}$ and $h = 10\,\mathrm{W/m^2/K}$. The constant thermal conductivity is $k = 1\,\mathrm{W/m/K}$ and volumetric heat generation is $q''' = 1200\,\mathrm{W/m^3}$. The exact and computed solutions are shown in Fig. 3.24 for four different meshes and two finite element types (linear: `EDGE2`; quadratic: `EDGE3`).

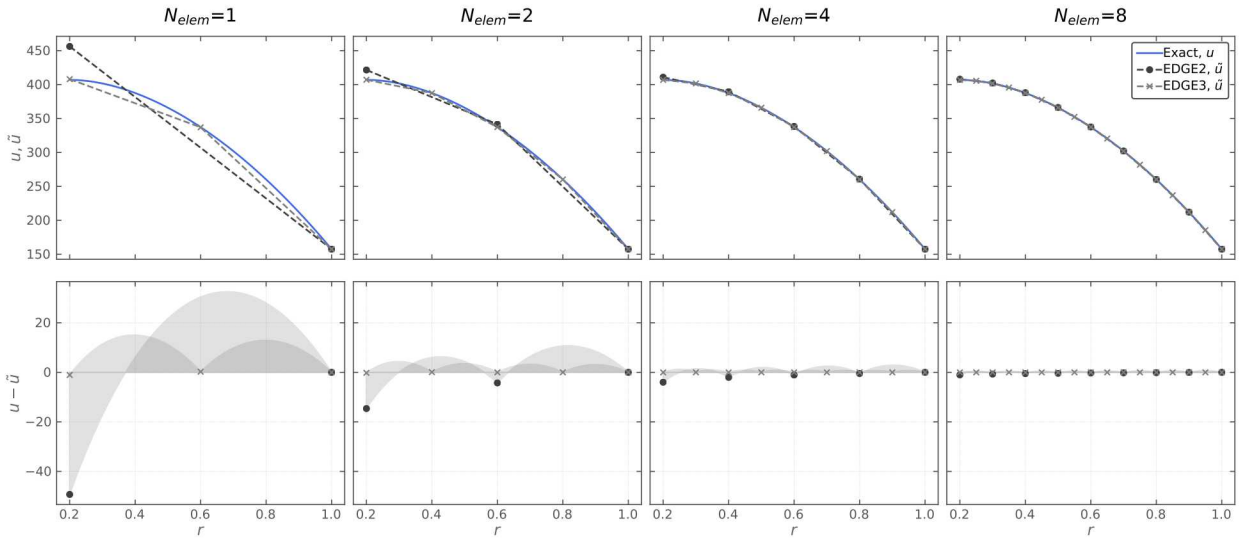

Figure 3.24: Temperature distribution and residuals for Prob. 3.8. Results are shown for the first four meshes. *First row*: exact and FE solutions using 1D elements. *Second row*: residuals between the exact solution and computed solutions.

A convergence study is conducted with a refinement factor of two (i.e., $r_r = 2$). The computed norms for each element type are plotted and tabulated in Fig. 3.25. The formal order of accuracy is two for linear FEs and three for quadratic FEs. In the asymptotic region, the linear and quadratic FE solutions converge to the exact solution with the correct order of accuracy.

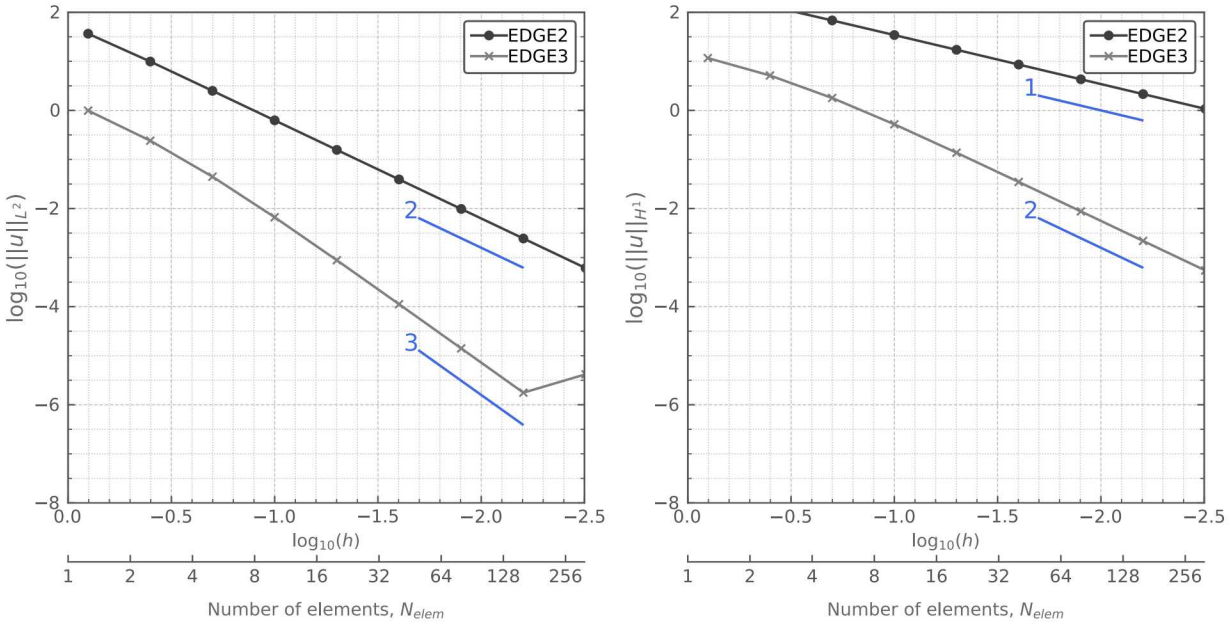

No. Elems	h	**Linear** ($p=1$) $\|\|u\|\|_{L_2}$	**Linear** ($p=1$) $\|\|u\|\|_{H_1}$	**Quadratic** ($p=2$) $\|\|u\|\|_{L_2}$	**Quadratic** ($p=2$) $\|\|u\|\|_{H_1}$
		elem_type=EDGE2		elem_type=EDGE3	
1	0.800000	3.656×10^{1}	2.511×10^{2}	9.894×10^{-1}	1.165×10^{1}
2	0.400000	9.900×10^{0}	1.336×10^{2}	2.411×10^{-1}	5.145×10^{0}
4	0.200000	2.504×10^{0}	6.821×10^{1}	4.453×10^{-2}	1.792×10^{0}
8	0.100000	6.267×10^{-1}	3.432×10^{1}	6.642×10^{-3}	5.207×10^{-1}
16	0.050000	1.567×10^{-1}	1.719×10^{1}	8.830×10^{-4}	1.372×10^{-1}
32	0.025000	3.918×10^{-2}	8.600×10^{0}	1.120×10^{-4}	3.482×10^{-2}
64	0.012500	9.794×10^{-3}	4.300×10^{0}	1.400×10^{-5}	8.739×10^{-3}
128	0.006250	2.448×10^{-3}	2.150×10^{0}	2.000×10^{-6}	2.187×10^{-3}
256	0.003125	6.120×10^{-4}	1.075×10^{0}	4.000×10^{-6}	5.470×10^{-4}

Figure 3.25: Spatial refinement analysis for Prob. 3.8. Results are computed using 1D elements and a spatial refinement factor $r_r = 2$. The formal order of accuracy is shown for each plot. *Left plot*: the L_2 norm quantifies convergence of the temperature distribution. *Right plot*: the H_1 norm quantifies convergence of the heat flux. *Table*: numerical values used to construct the plots.

Problem 3.9: Hollow cylinder with internal heating and inside convection boundary

An infinitely long hollow cylinder with inner radius r_i and outer radius r_o has a thermal conductivity k and internal heat generation q'''. The outside surface is insulated and the inside surface is exposed to a fluid at temperature u_f and heat transfer coefficient h. If the cylinder is in thermal equilibrium, the analytic solution for the temperature distribution is [29]

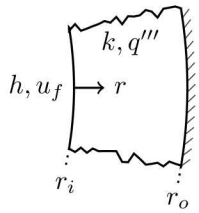

$$u(r) = u_f + \frac{q''' r_i^2}{4k}\left(\frac{2k}{h r_i}\left[\left(\frac{r_o}{r_i}\right)^2 - 1\right] + 1 - \left(\frac{r}{r_i}\right)^2 + 2\left(\frac{r_o}{r_i}\right)^2 \ln\left(\frac{r}{r_i}\right)\right). \tag{3.13}$$

The problem is solved in BISON on the domain $\boldsymbol{X} \in [0.2, 1]$. The boundary conditions are convective and Neumann: $q_o'' = h(u_f - u_i)$ and $(du/dx)_{r=1} = 0$. The fluid temperature and heat transfer coefficient are $u_f = 100\,\mathrm{K}$ and $h = 10\,\mathrm{W/m^2/K}$. The constant thermal conductivity is $k = 1\,\mathrm{W/m/K}$ and the volumetric heat generation is $q''' = 1200\,\mathrm{W/m^3}$. The exact and computed solutions are shown in Fig. 3.26 for four different meshes and two finite element types (linear: `EDGE2`; quadratic: `EDGE3`).

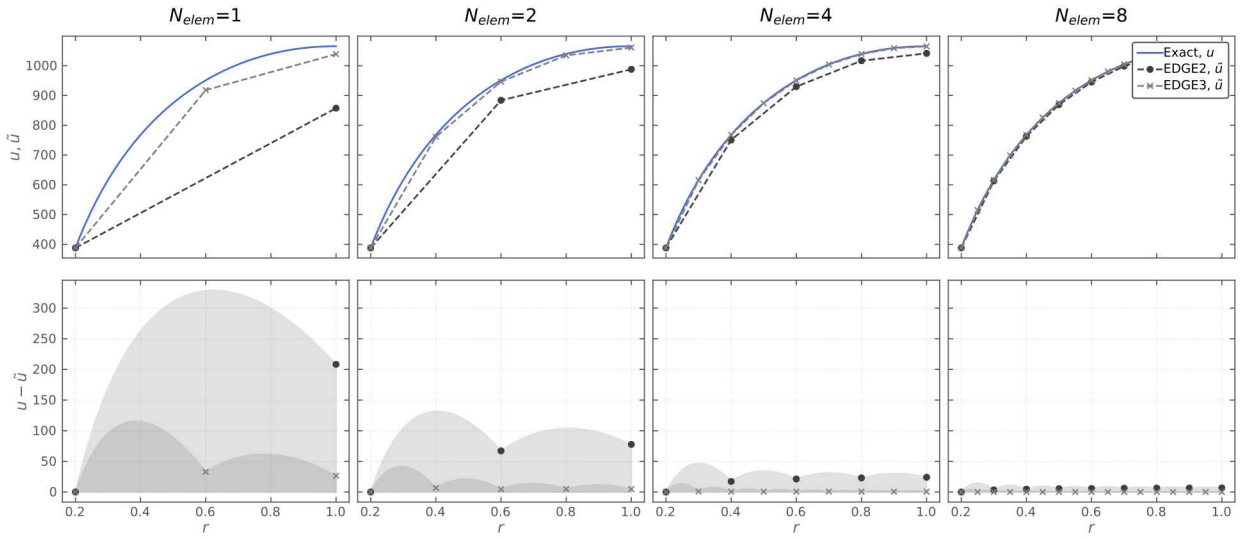

Figure 3.26: Temperature distribution and residuals for Prob. 3.9. Results are shown for the first four meshes. *First row*: exact and FE solutions using 1D elements. *Second row*: residuals between the exact solution and computed solutions.

A convergence study is conducted with a refinement factor of two (i.e., $r_r = 2$). The computed norms for each element type are plotted and tabulated in Fig. 3.27. The formal order of accuracy is two for linear FEs and three for quadratic FEs. In the asymptotic region, the linear and quadratic FE solutions converge to the exact solution with the correct order of accuracy.

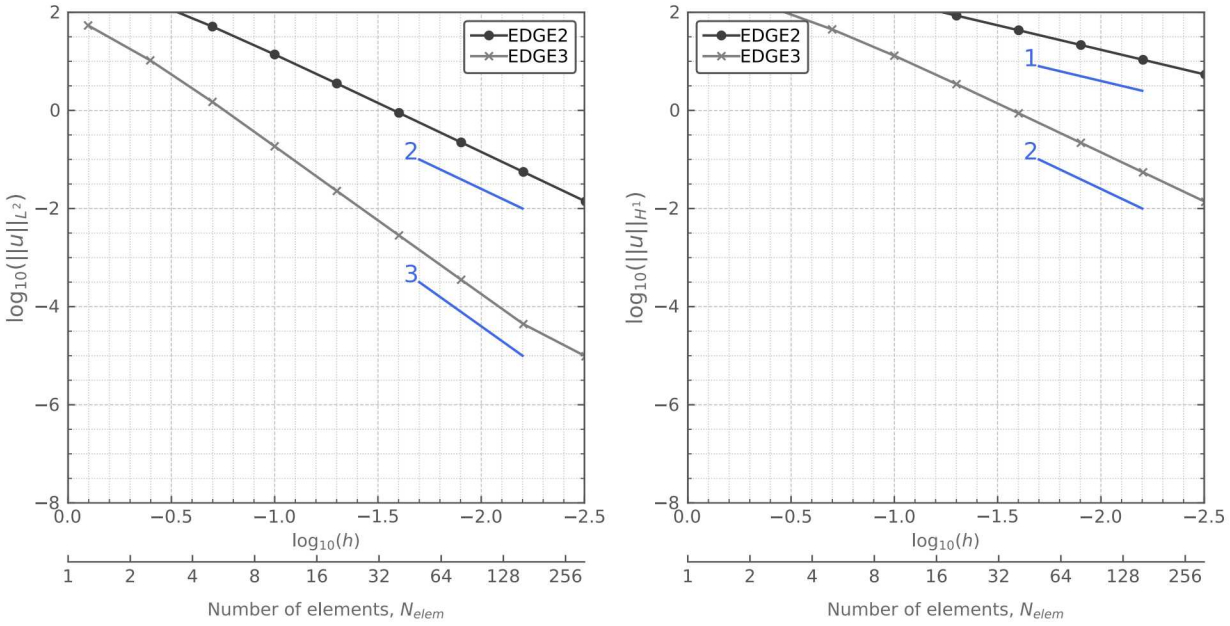

No. Elems	h	**Linear** ($p=1$) $\|\|u\|\|_{L_2}$	**Linear** ($p=1$) $\|\|u\|\|_{H_1}$	**Quadratic** ($p=2$) $\|\|u\|\|_{L_2}$	**Quadratic** ($p=2$) $\|\|u\|\|_{H_1}$
		elem_type=EDGE2		elem_type=EDGE3	
1	0.800000	4.774×10^{2}	9.463×10^{2}	5.387×10^{1}	2.912×10^{2}
2	0.400000	1.690×10^{2}	5.780×10^{2}	1.046×10^{1}	1.286×10^{2}
4	0.200000	5.106×10^{1}	3.226×10^{2}	1.490×10^{0}	4.479×10^{1}
8	0.100000	1.379×10^{1}	1.687×10^{2}	1.852×10^{-1}	1.302×10^{1}
16	0.050000	3.534×10^{0}	8.556×10^{1}	2.278×10^{-2}	3.430×10^{0}
32	0.025000	8.893×10^{-1}	4.295×10^{1}	2.831×10^{-3}	8.705×10^{-1}
64	0.012500	2.227×10^{-1}	2.150×10^{1}	3.530×10^{-4}	2.185×10^{-1}
128	0.006250	5.570×10^{-2}	1.075×10^{1}	4.400×10^{-5}	5.467×10^{-2}
256	0.003125	1.393×10^{-2}	5.376×10^{0}	1.000×10^{-5}	1.367×10^{-2}

Figure 3.27: Spatial refinement analysis for Prob. 3.9. Results are computed using 1D elements and a spatial refinement factor $r_r = 2$. The formal order of accuracy is shown for each plot. *Left plot*: the L_2 norm quantifies convergence of the temperature distribution. *Right plot*: the H_1 norm quantifies convergence of the heat flux. *Table*: numerical values used to construct the plots.

Problem 3.10: Short solid cylinder

A two-dimensional short cylinder with length L and radius R has a thermal conductivity $k = 1$ and no internal heating. It is exposed on each surface to a constant temperature: $u(R, z) = u_1$, $u(r, 0) = u_1$, and $u(r, L) = u_2$. In thermal equilibrium, the analytic solution for the temperature distribution is [28, pp.133–134]

$$u(r, z) = u_1 + 2(u_2 - u_1) \sum_{n=1}^{\infty} \frac{\sinh(\lambda_n / R) z}{\lambda_n \sinh(\lambda_n L / R) J_1(\lambda_n)} J_0\left(\lambda_n \frac{r}{R}\right), \quad (3.14)$$

where λ_n are the consecutive roots of the equation $J_0(\lambda R) = 0$.

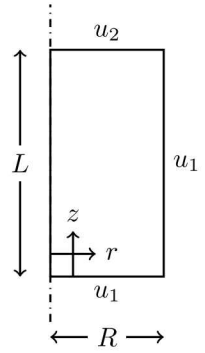

This problem is solved in BISON on the domain $r \in [0, 1]$ and $z \in [0, 1]$. Dirichlet boundary conditions are applied to each surface: $u(R, z) = u(r, 0) = u_1 = 0\,\mathrm{K}$ and $u(r, L) = u_2 = 200\,\mathrm{K}$.

Fig. 3.29 shows the convergence of five FE choices as the two-dimensional mesh is refined. All five FE choices result in similar shapes. Currently, Bessel functions are not implemented as a function option in BISON when computing norms between the computed and analytic solution. For this reason, norms are calculated between successively refined solutions instead of between the computed and analytic solution. Therefore, this problem is a *solution verification* problem, rather than a code verification problem. The local norm at the middle of the domain is calculated for successive refinements and is shown in Fig. 3.28.

The linear FEs `QUAD4` and `TRI3` display the correct second order convergence. The quadratic FEs `QUAD8` and `TRI6` have the correct third order convergence. The `QUAD9` FEs have super-convergent behavior.

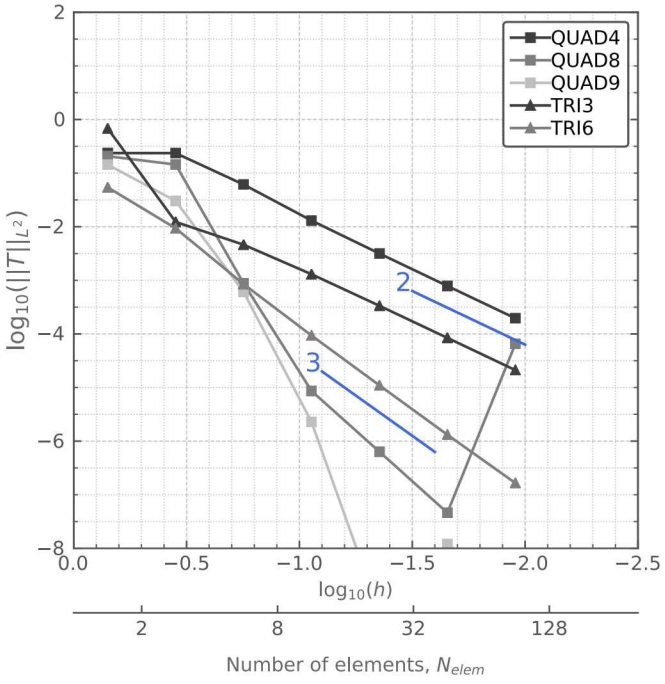

Figure 3.28: Spatial refinement analysis for Prob. 3.10. Results are computed using 2D elements and a spatial refinement factor $r_r = 2$. The formal order of accuracy is shown for each plot.

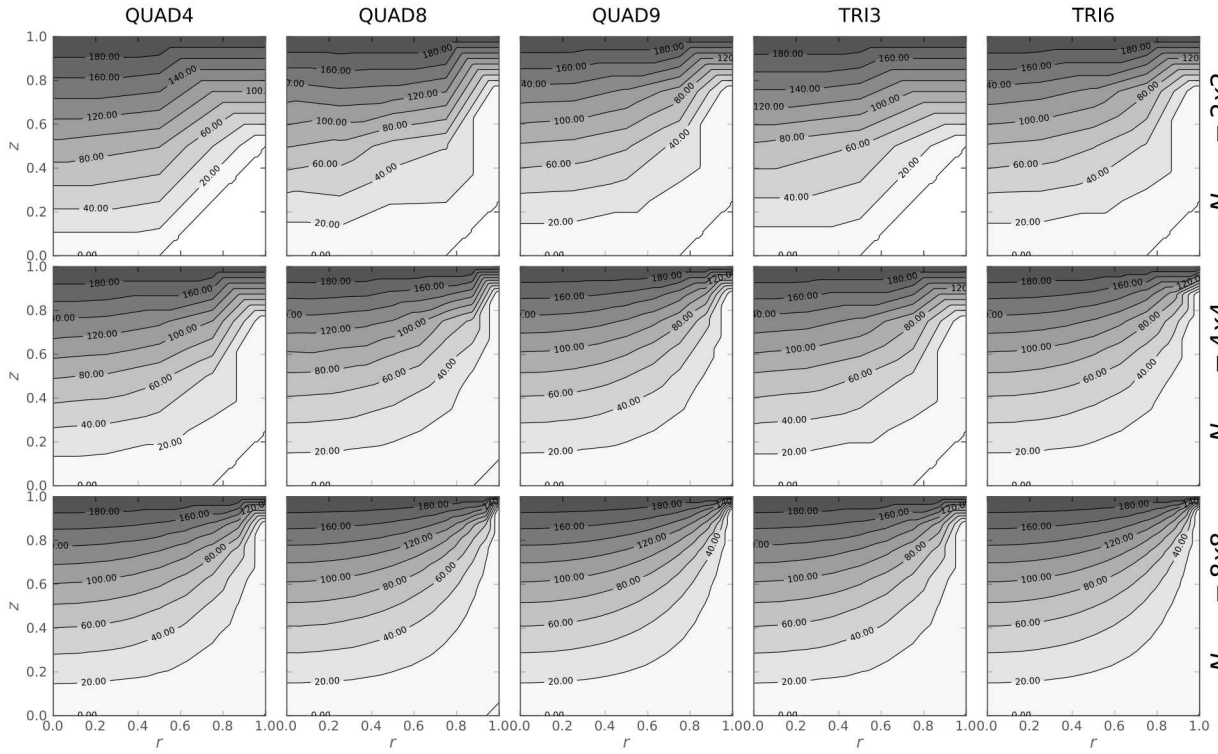

Figure 3.29: Temperature distribution for Prob. 3.10 with three different meshes and five FE types. Darker colors indicate higher temperatures.

Problem 3.11: Solid sphere with internal heating

A solid sphere with radius R has thermal conductivity k and internal heat generation q'''. The outside surface is exposed to a fluid at temperature u_f with heat transfer coefficient h. If the sphere is in thermal equilibrium, the analytic solution for the temperature distribution is [29, 30]

$$u(r) = u_f + \frac{q''' R^2}{4k}\left[1 - \left(\frac{r}{R}\right)^2 + \frac{2k}{hR}\right]. \tag{3.15}$$

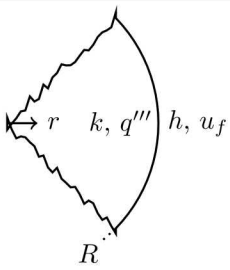

The problem is solved in BISON on the domain $\boldsymbol{X} \in [0, 1]$. The center of the sphere uses a Neumann boundary condition (finiteness requirement) and the surface has a convective boundary condition: $(du/dr)_{r=0} = 0$ and $q''_o = h(u_f - u_o)$. The fluid temperature and heat transfer coefficient are $u_f = 500\,\mathrm{K}$ and $h = 1\,\mathrm{W/m^2/K}$. Steady state heat conduction is considered with constant thermal conductivity $k = 1\,\mathrm{W/m/K}$ and volumetric heat generation $q''' = 1200\,\mathrm{W/m^3}$. The exact and computed solutions are shown in Fig. 3.30 for four different meshes and two finite element types (linear: `EDGE2`; quadratic: `EDGE3`).

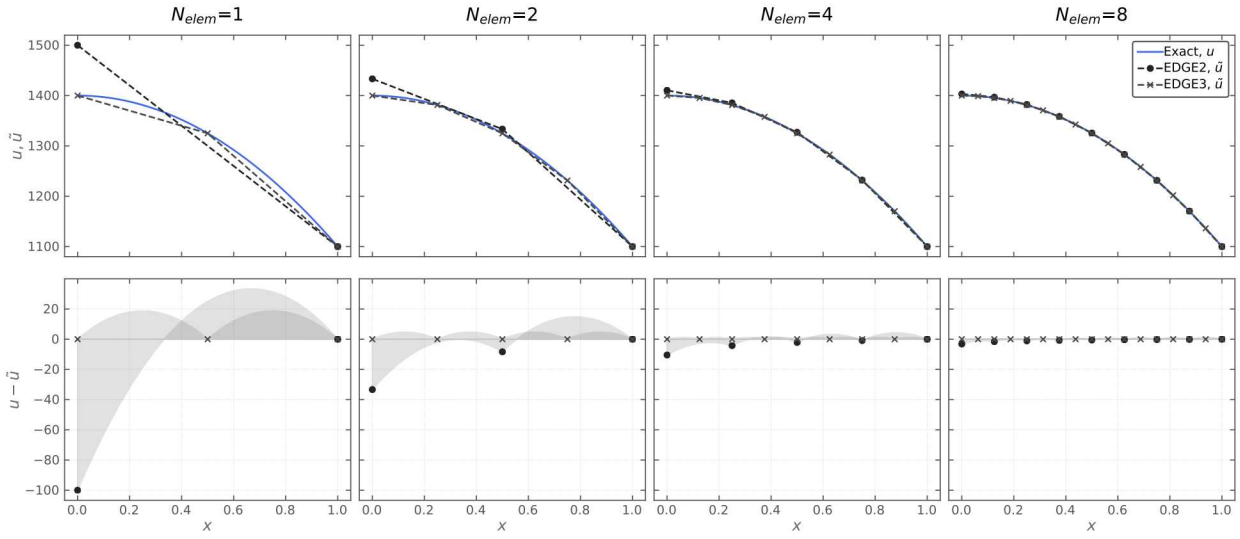

Figure 3.30: Temperature distribution and residuals for Prob. 3.11. Results are shown for the first four meshes. *First row*: exact and FE solutions using 1D elements. *Second row*: residuals between the exact solution and computed solutions.

A convergence study is conducted with a refinement factor of two (i.e., $r_r = 2$). The computed norms for each element type are plotted and tabulated in Fig. 3.31. The formal order of accuracy is two for linear FEs and three for quadratic FEs. In the asymptotic region, the linear and quadratic FE solutions converge to the exact solution with the correct order of accuracy.

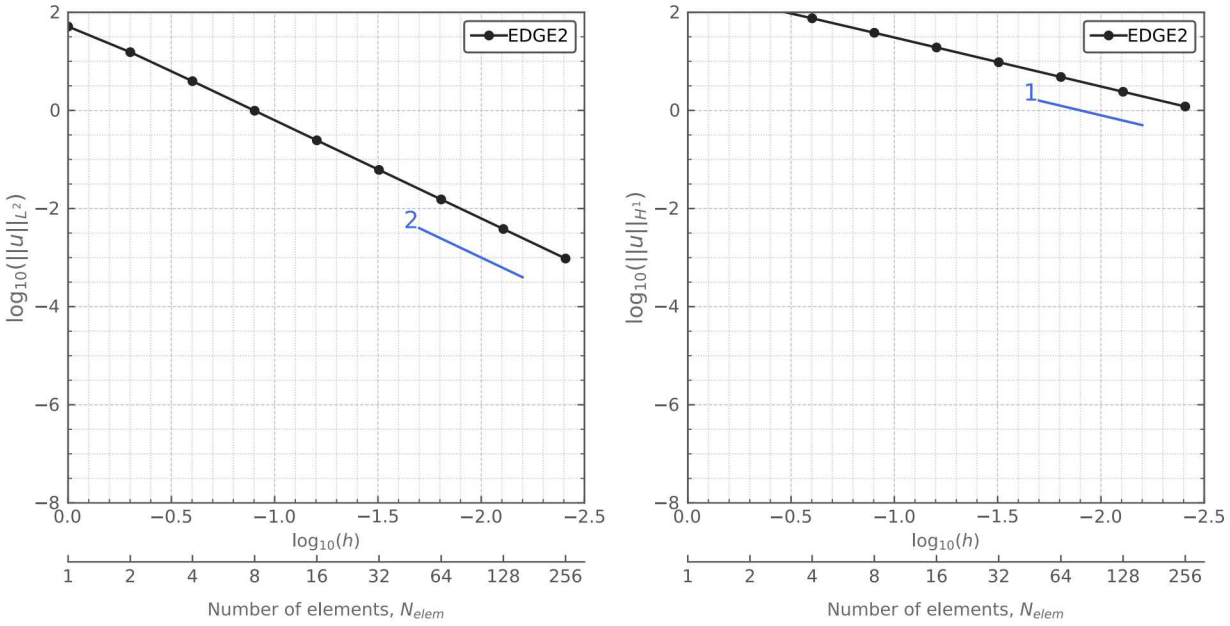

No. Elems	h	**Linear** ($p=1$) $\|\|u\|\|_{L_2}$	**Linear** ($p=1$) $\|\|u\|\|_{H_1}$	**Quadratic** ($p=2$) $\|\|u\|\|_{L_2}$	**Quadratic** ($p=2$) $\|\|u\|\|_{H_1}$
		elem_type=EDGE2		elem_type=EDGE3	
1	1.000000	5.117×10^{1}	2.507×10^{2}	1.897×10^{-9}	6.419×10^{-10}
2	0.500000	1.537×10^{1}	1.447×10^{2}	3.843×10^{-9}	8.229×10^{-9}
4	0.250000	3.941×10^{0}	7.540×10^{1}	4.728×10^{-8}	1.028×10^{-7}
8	0.125000	9.845×10^{-1}	3.817×10^{1}	2.322×10^{-8}	2.108×10^{-7}
16	0.062500	2.454×10^{-1}	1.916×10^{1}	3.548×10^{-8}	1.151×10^{-6}
32	0.031250	6.126×10^{-2}	9.589×10^{0}	1.317×10^{-9}	1.250×10^{-9}
64	0.015625	1.531×10^{-2}	4.796×10^{0}	2.603×10^{-8}	1.542×10^{-8}
128	0.007812	3.825×10^{-3}	2.398×10^{0}	1.925×10^{-7}	1.218×10^{-7}
256	0.003906	9.560×10^{-4}	1.199×10^{0}	1.532×10^{-6}	9.137×10^{-7}

Figure 3.31: Spatial refinement analysis for Prob. 3.11. Results are computed using 1D elements and a spatial refinement factor $r_r = 2$. The formal order of accuracy is shown for each plot. *Left plot*: the L_2 norm quantifies convergence of the temperature distribution. *Right plot*: the H_1 norm quantifies convergence of the heat flux. *Table*: numerical values used to construct the plots.

Problem 3.12: Spherical shell with Dirichlet conditions

A spherical shell with inner radius r_i and outer radius r_o has a constant thermal conductivity k. Both surfaces are exposed to constant temperatures: $u(i) = u_i$ and $u(r_o) = u_o$. If the spherical shell is in thermal equilibrium, the analytic solution for the temperature distribution is [26, pp.136]

$$u(r) = -\frac{1}{r}\left(\frac{u_i - u_o}{\frac{1}{r_o} - \frac{1}{r_i}}\right) + \frac{\frac{u_o}{r_i} - \frac{u_i}{r_o}}{\frac{1}{r_i} - \frac{1}{r_o}}. \tag{3.16}$$

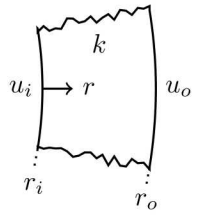

The problem is solved in BISON on the domain $\boldsymbol{X} \in [0.2, 1]$ using Dirichlet boundary conditions: $u(r_i) = u_i = 300\,\mathrm{K}$ and $u(r_o) = u_o = 0\,\mathrm{K}$. Steady state heat conduction is considered in the solid with constant thermal conductivity $k = 5\,\mathrm{W/m/K}$. The exact and computed solutions are shown in Fig. 3.32 for four different meshes and two finite element types (linear: `EDGE2`; quadratic: `EDGE3`).

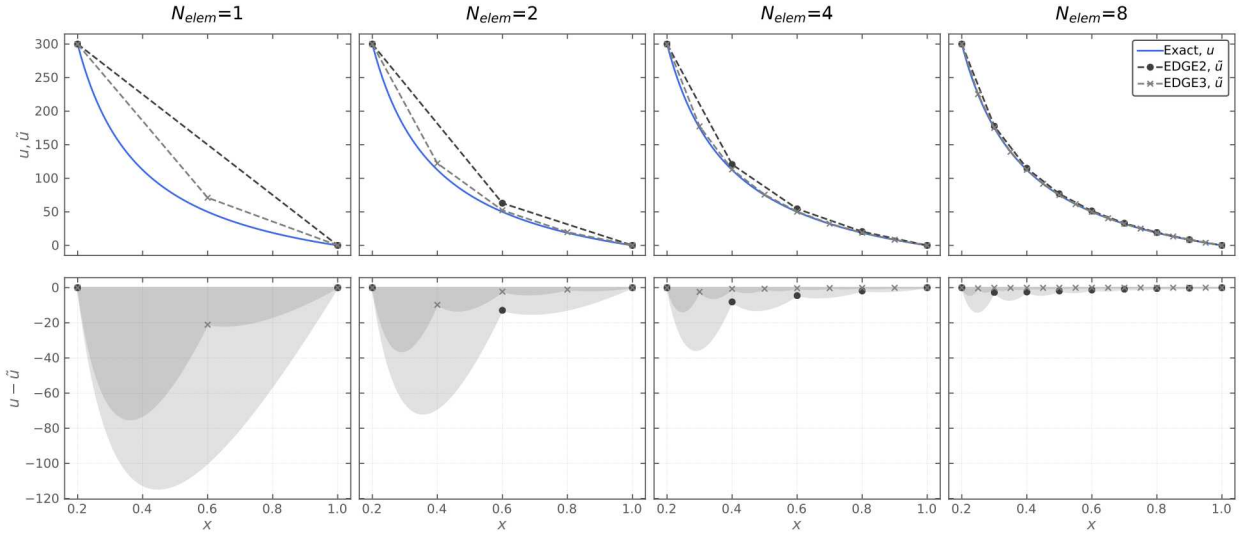

Figure 3.32: Temperature distribution and residuals for Prob. 3.12. Results are shown for the first four meshes. *First row*: exact and FE solutions using 1D elements. *Second row*: residuals between the exact solution and computed solutions.

A convergence study is conducted with a refinement factor of two (i.e., $r_r = 2$). The computed norms for each element type are plotted and tabulated in Fig. 3.33. The formal order of accuracy is two for linear FEs and three for quadratic FEs. In the asymptotic region, the linear and quadratic FE solutions converge to the exact solution with the correct order of accuracy.

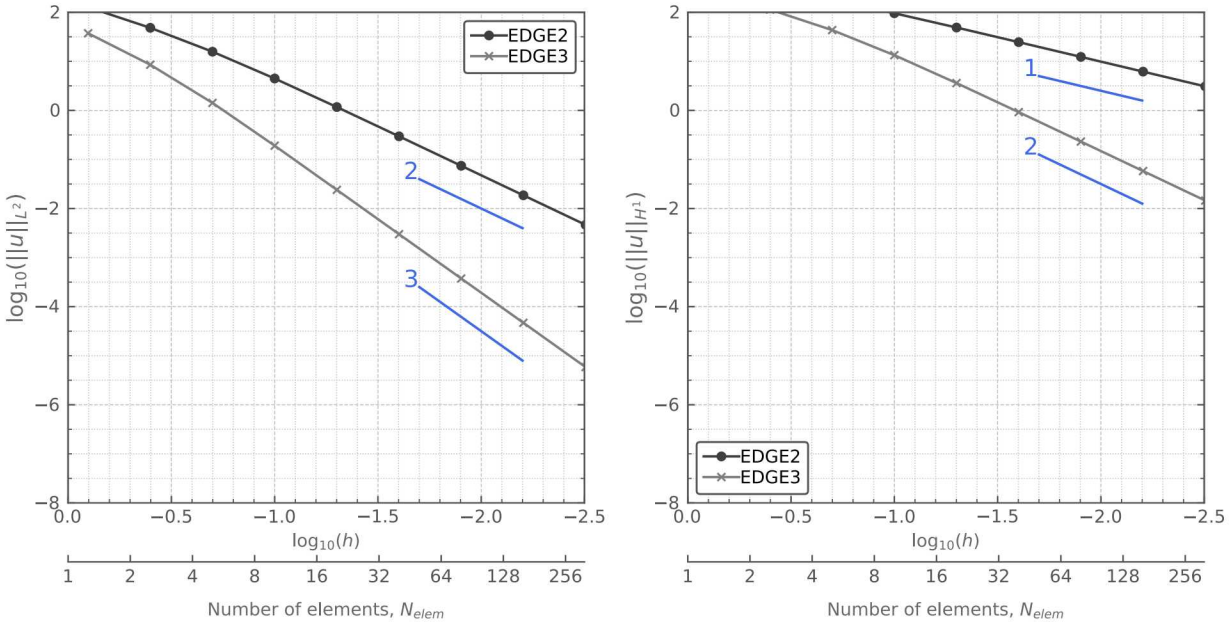

No. Elems	h	**Linear** ($p=1$) $\|\|u\|\|_{L_2}$	**Linear** ($p=1$) $\|\|u\|\|_{H_1}$	**Quadratic** ($p=2$) $\|\|u\|\|_{L_2}$	**Quadratic** ($p=2$) $\|\|u\|\|_{H_1}$
		elem_type=EDGE2		elem_type=EDGE3	
1	0.800000	1.268×10^{2}	5.171×10^{2}	3.728×10^{1}	2.369×10^{2}
2	0.400000	4.820×10^{1}	3.110×10^{2}	8.522×10^{0}	1.135×10^{2}
4	0.200000	1.572×10^{1}	1.782×10^{2}	1.422×10^{0}	4.334×10^{1}
8	0.100000	4.467×10^{0}	9.540×10^{1}	1.909×10^{-1}	1.335×10^{1}
16	0.050000	1.169×10^{0}	4.888×10^{1}	2.401×10^{-2}	3.603×10^{0}
32	0.025000	2.961×10^{-1}	2.461×10^{1}	2.999×10^{-3}	9.214×10^{-1}
64	0.012500	7.429×10^{-2}	1.233×10^{1}	3.750×10^{-4}	2.317×10^{-1}
128	0.006250	1.859×10^{-2}	6.167×10^{0}	4.700×10^{-5}	5.802×10^{-2}
256	0.003125	4.648×10^{-3}	3.084×10^{0}	6.000×10^{-6}	1.451×10^{-2}

Figure 3.33: Spatial refinement analysis for Prob. 3.12. Results are computed using 1D elements and a spatial refinement factor $r_r = 2$. The formal order of accuracy is shown for each plot. *Left plot*: the L_2 norm quantifies convergence of the temperature distribution. *Right plot*: the H_1 norm quantifies convergence of the heat flux. *Table*: numerical values used to construct the plots.

Problem 3.13: Spherical shell with temperature dependent thermal conductivity

A spherical shell with inside radius r_i and outside radius r_o has a thermal conductivity that varies linearly with temperature: $k = k_o + \beta(u - u_o)$. The inside and outside surfaces of the shell are exposed to constant temperatures: $u(r_i) = u_i$ and $u(r_o) = u_o$. In thermal equilibrium, the analytic solution for the temperature distribution is [26, pp.139]

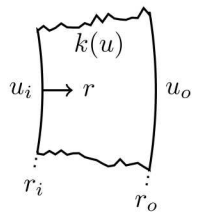

$$u(r) = u_o + \frac{k_o}{\beta}\left[\sqrt{1 + \beta\frac{(k_i + k_o)}{k_o^2}\frac{\left(\frac{1}{r} - \frac{1}{r_o}\right)}{\left(\frac{1}{r_i} - \frac{1}{r_o}\right)}(u_i - u_o)} - 1\right]. \qquad (3.17)$$

The problem is solved in BISON on the domain $\boldsymbol{X} \in [0.2, 1]$. Dirichlet boundary conditions are applied: $u(0.2) = u_i = 300\,\mathrm{K}$ and $u(1) = u_o = 0\,\mathrm{K}$. Steady state heat conduction is considering using a nonlinear thermal conductivity, where $k_o = 5\,\mathrm{W/m/K}$. The nonlinearity of the problem is quantified by β; the analytic solution as a function of β is shown in Fig. 3.34. Two cases are examined in this study: (I) $\beta = 0.001$ and (II) $\beta = 0.1$.

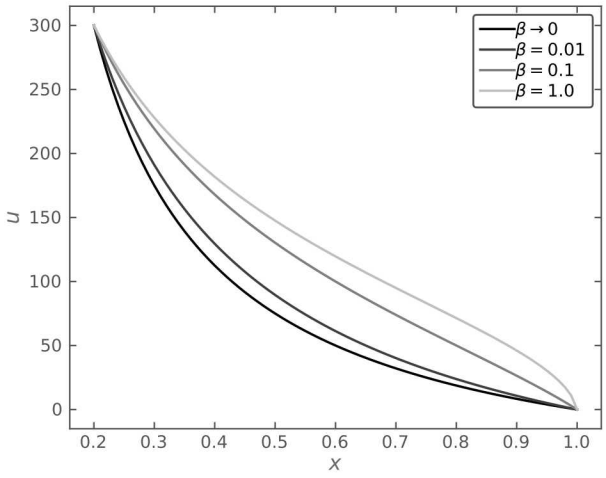

Figure 3.34: The exact solution for Prob. 3.13 as a function of space and β.

Case I ($\beta = 0.001$): The exact and computed solutions are shown in Fig. 3.35a for four different meshes and two FEs types (linear: `EDGE2`; quadratic: `EDGE3`). A convergence study is conducted with a refinement factor of two (i.e., $r_r = 2$). The computed norms for each element type are plotted and tabulated in Fig. 3.36. The formal order of accuracy is two for linear FEs and three for quadratic FEs. In the asymptotic region, the linear and quadratic FE solutions converge to the exact solution with the correct order of accuracy.

Case II ($\beta = 0.1$): The exact and computed solutions are shown in Fig. 3.35b for four different meshes and two FEs types (linear: `EDGE2`; quadratic: `EDGE3`). A convergence study is conducted with a refinement factor of two (i.e., $r_r = 2$). The computed norms for each element type are plotted and tabulated in Fig. 3.37. The formal order of accuracy is two for linear FEs and three for quadratic FEs. In the asymptotic region, the linear and quadratic FE solutions converge to the exact solution with the correct order of accuracy.

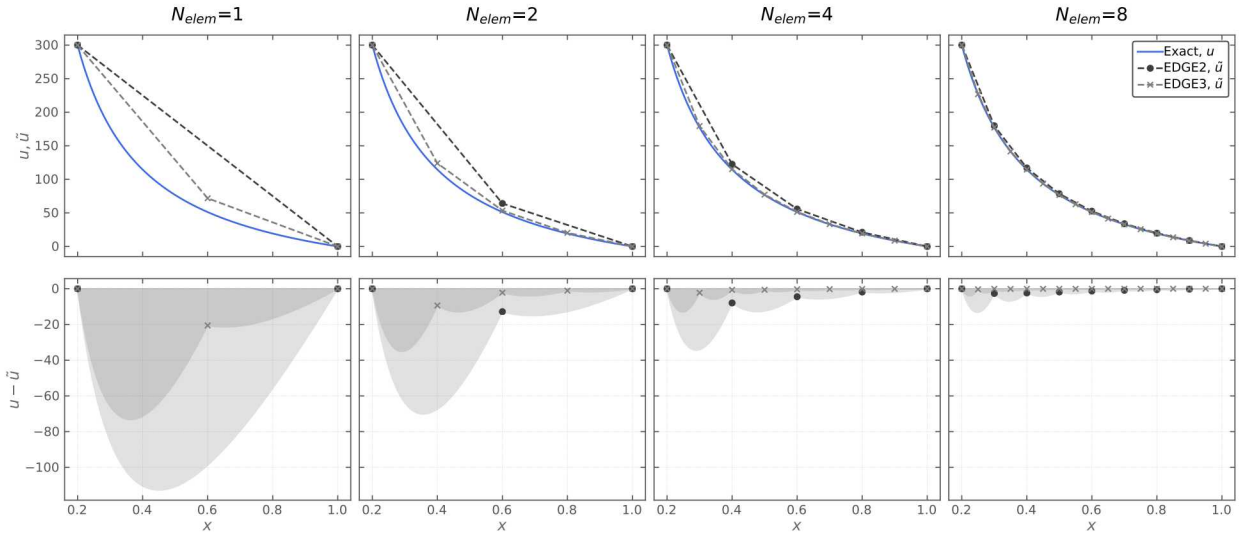

(a) Case I, $\beta = 0.001$

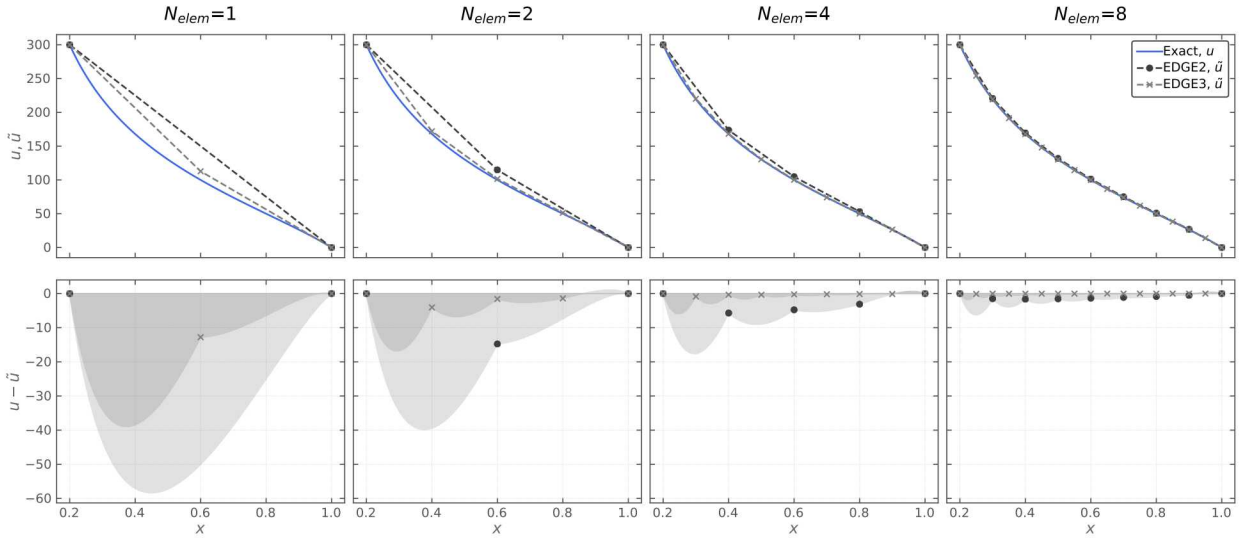

(b) Case II, $\beta = 0.1$

Figure 3.35: Temperature distribution and residuals for Prob. 3.13. Results are shown for the first four meshes. *First row*: exact and FE solutions using 1D elements. *Second row*: residuals between the exact and computed solutions.

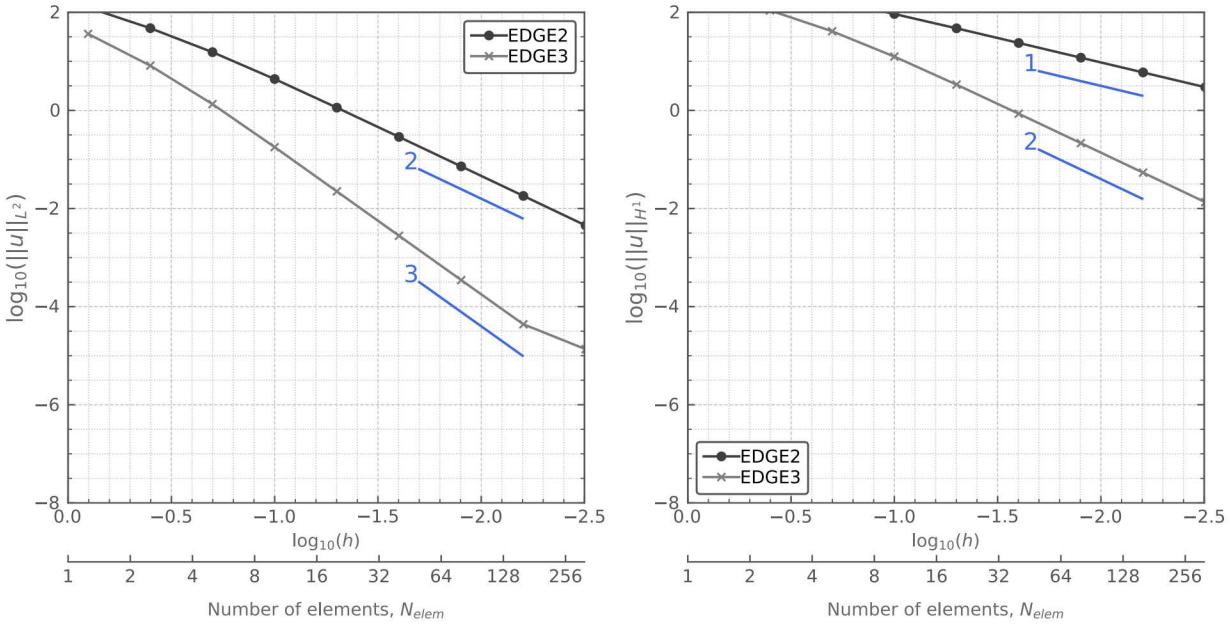

No. Elems	h	**Linear** ($p=1$) $\|\|u\|\|_{L_2}$	**Linear** ($p=1$) $\|\|u\|\|_{H_1}$	**Quadratic** ($p=2$) $\|\|u\|\|_{L_2}$	**Quadratic** ($p=2$) $\|\|u\|\|_{H_1}$
		elem_type=EDGE2		elem_type=EDGE3	
1	0.800000	1.250×10^{2}	5.124×10^{2}	3.625×10^{1}	2.315×10^{2}
2	0.400000	4.737×10^{1}	3.054×10^{2}	8.164×10^{0}	1.090×10^{2}
4	0.200000	1.537×10^{1}	1.733×10^{2}	1.343×10^{0}	4.096×10^{1}
8	0.100000	4.353×10^{0}	9.218×10^{1}	1.784×10^{-1}	1.248×10^{1}
16	0.050000	1.137×10^{0}	4.711×10^{1}	2.232×10^{-2}	3.350×10^{0}
32	0.025000	2.879×10^{-1}	2.370×10^{1}	2.784×10^{-3}	8.553×10^{-1}
64	0.012500	7.222×10^{-2}	1.187×10^{1}	3.480×10^{-4}	2.150×10^{-1}
128	0.006250	1.807×10^{-2}	5.937×10^{0}	4.400×10^{-5}	5.382×10^{-2}
256	0.003125	4.519×10^{-3}	2.969×10^{0}	1.400×10^{-5}	1.346×10^{-2}

Figure 3.36: Spatial refinement analysis for Prob. 3.13 (Case I, $\beta = 0.001$). Results are computed using 1D elements and a spatial refinement factor $r_x = 2$. The formal order of accuracy is shown for each plot. *Left plot*: the L_2 norm quantifies convergence of the temperature distribution. *Right plot*: the H_1 norm quantifies convergence of the heat flux. *Table*: numerical values used to construct the plots.

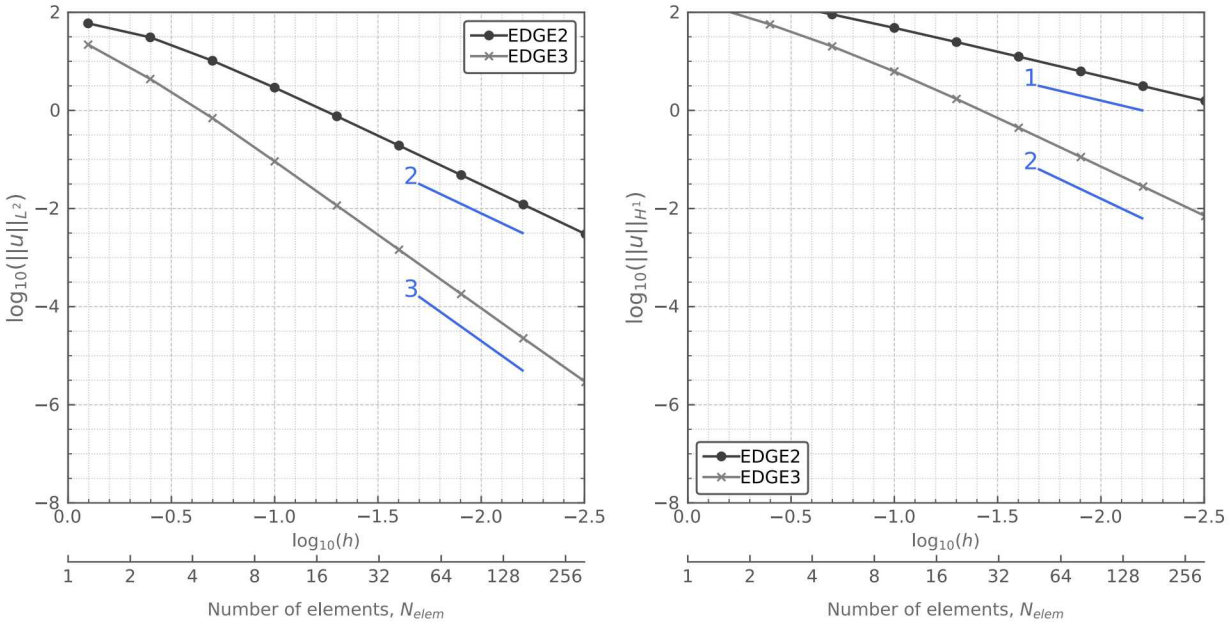

No. Elems	h	**Linear** ($p=1$) $\|\|u\|\|_{L_2}$	**Linear** ($p=1$) $\|\|u\|\|_{H_1}$	**Quadratic** ($p=2$) $\|\|u\|\|_{L_2}$	**Quadratic** ($p=2$) $\|\|u\|\|_{H_1}$
		elem_type=EDGE2		elem_type=EDGE3	
1	0.800000	5.938×10^{1}	2.750×10^{2}	2.187×10^{1}	1.396×10^{2}
2	0.400000	3.084×10^{1}	1.626×10^{2}	4.363×10^{0}	5.658×10^{1}
4	0.200000	1.028×10^{1}	9.029×10^{1}	6.955×10^{-1}	2.016×10^{1}
8	0.100000	2.908×10^{0}	4.802×10^{1}	9.144×10^{-2}	6.208×10^{0}
16	0.050000	7.583×10^{-1}	2.467×10^{1}	1.151×10^{-2}	1.710×10^{0}
32	0.025000	1.918×10^{-1}	1.245×10^{1}	1.445×10^{-3}	4.427×10^{-1}
64	0.012500	4.811×10^{-2}	6.238×10^{0}	1.810×10^{-4}	1.118×10^{-1}
128	0.006250	1.204×10^{-2}	3.121×10^{0}	2.300×10^{-5}	2.803×10^{-2}
256	0.003125	3.010×10^{-3}	1.561×10^{0}	3.000×10^{-6}	7.011×10^{-3}

Figure 3.37: Spatial refinement analysis for Prob. 3.13 (Case II, $\beta = 0.1$). Results are computed using 1D elements and a spatial refinement factor $r_x = 2$. The formal order of accuracy is shown for each plot. *Left plot*: the L_2 norm quantifies the convergence of the temperature distribution. *Right plot*: the H_1 norm quantifies the convergence of heat flux. *Table*: numerical values used to construct the plots.

Problem 3.14: Solid sphere with spatially dependent internal heating

A solid sphere with radius R has a constant thermal conductivity k and a spatially dependent internal heating $q''' = q'''_o\left(1 - \beta r^2/R^2\right)$. It is exposed to a constant temperature on its surface $u(R) = u_R$. The sphere reaches thermal equilibrium and the analytic solution for the temperature distribution is [29, 31]

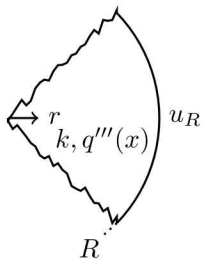

$$u(r) = u_R + \frac{q'''_0 R^2}{6k}\left\{\left[1 - \left(\frac{r}{R}\right)^2\right] - \frac{3\beta}{10}\left[1 - \left(\frac{r}{R}\right)^4\right]\right\}. \tag{3.18}$$

The problem is solved in BISON on the domain $\boldsymbol{X} \in [0, 1]$. The center of the sphere uses a Neumann boundary condition (finiteness requirement) and the surface has a Dirichlet condition: $(du/dr)_{r=0} = 0$ and $u(1) = u_R = 300\,\mathrm{K}$. Steady state heat conduction is considered in the sphere with constant thermal conductivity $k = 1\,\mathrm{W/m/K}$. The exact and computed solutions are shown in Fig. 3.38 for four different meshes and two finite element types (linear: `EDGE2`; quadratic: `EDGE3`).

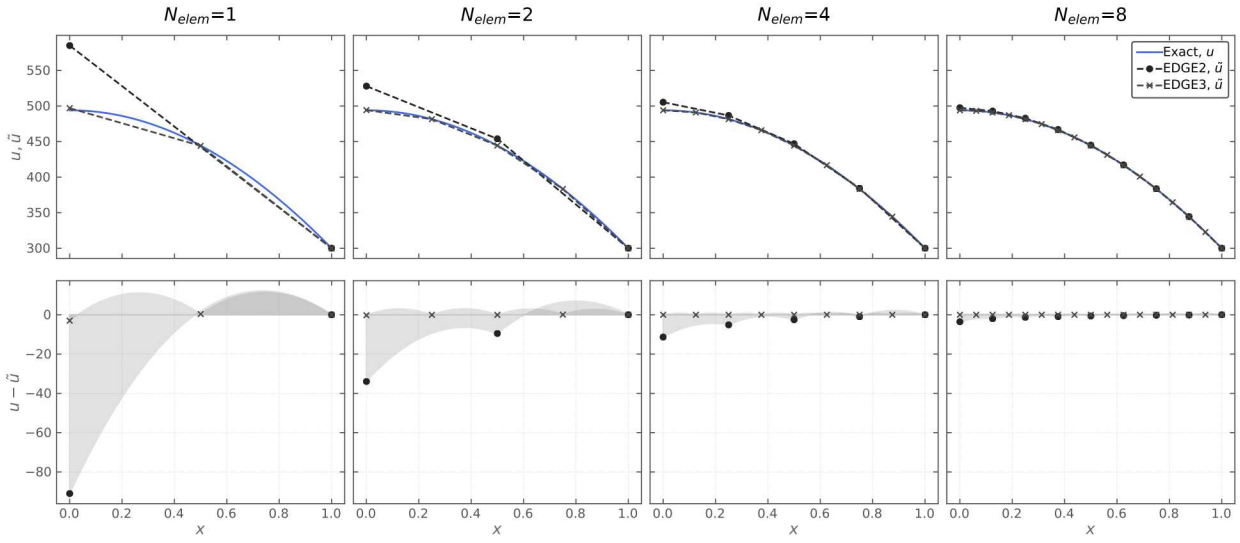

Figure 3.38: Temperature distribution and residuals for Prob. 3.14. Results are shown for the first four meshes. *First row*: exact and FE solutions using 1D elements. *Second row*: residuals between the exact solution and computed solutions.

A convergence study is conducted with a refinement factor of two (i.e., $r_r = 2$). The computed norms for each element type are plotted and tabulated in Fig. 3.39. The formal order of accuracy is two for linear FEs and three for quadratic FEs. In the asymptotic region, the linear and quadratic FE solutions converge to the exact solution with the correct order of accuracy.

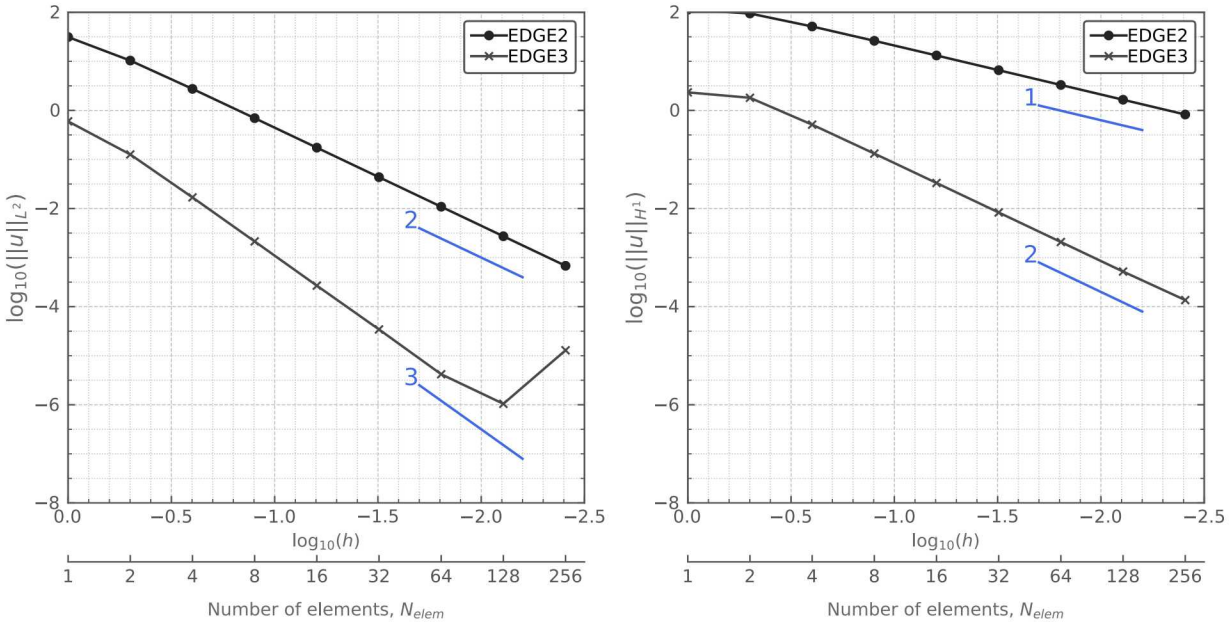

No. Elems	h	**Linear** ($p=1$) $\|\|u\|\|_{L_2}$	**Linear** ($p=1$) $\|\|u\|\|_{H_1}$	**Quadratic** ($p=2$) $\|\|u\|\|_{L_2}$	**Quadratic** ($p=2$) $\|\|u\|\|_{H_1}$
		elem_type=EDGE2		elem_type=EDGE3	
1	1.000000	3.125×10^{1}	1.126×10^{2}	0.598×10^{-1}	2.330×10^{0}
2	0.500000	1.036×10^{1}	9.440×10^{1}	1.265×10^{-1}	1.807×10^{0}
4	0.250000	2.744×10^{0}	5.132×10^{1}	1.685×10^{-2}	5.122×10^{-1}
8	0.125000	6.942×10^{-1}	2.620×10^{1}	2.136×10^{-3}	1.317×10^{-1}
16	0.062500	1.740×10^{-1}	1.317×10^{1}	2.680×10^{-4}	3.316×10^{-2}
32	0.031250	4.351×10^{-2}	6.594×10^{0}	3.400×10^{-5}	8.304×10^{-3}
64	0.015625	1.088×10^{-2}	3.298×10^{0}	4.000×10^{-6}	2.077×10^{-3}
128	0.007812	2.719×10^{-3}	1.649×10^{0}	1.000×10^{-6}	5.190×10^{-4}
256	0.003906	6.800×10^{-4}	8.246×10^{-1}	1.300×10^{-5}	1.360×10^{-4}

Figure 3.39: Spatial refinement analysis for Prob. 3.14. Results are computed using 1D elements and a spatial refinement factor $r_r = 2$. The formal order of accuracy is shown for each plot. *Left plot*: the L_2 norm quantifies convergence of the temperature distribution. *Right plot*: the H_1 norm quantifies convergence of the heat flux. *Table*: numerical values used to construct the plots.

Problem 3.15: Solid sphere with internal heating and convective boundary condition

A solid sphere with radius R has a constant thermal conductivity k and internal heating q'''. It is exposed on its outside surface to a fluid with constant temperature u_f and heat transfer coefficient h. In thermal equilibrium, the analytic temperature distribution is [29, 32]

$$u(r) = u_f + \frac{q''' R^2}{6k}\left[1 - \left(\frac{r}{R}\right)^2 + \frac{2k}{hR}\right]. \tag{3.19}$$

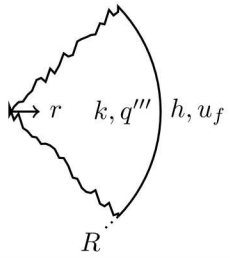

The problem is solved in BISON on the domain $\boldsymbol{X} \in [0, 1]$. The center of the sphere uses a Neumann boundary condition (finiteness requirement) and the surface has a convective boundary condition: $(du/dr)_{r=0} = 0$ and $q''_o = h(u_f - u_o)$. The fluid temperature and heat transfer coefficient are $u_f = 500\,\mathrm{K}$ and $h = 1\,\mathrm{W/m^2/K}$. Steady state heat conduction is considered in the sphere with constant thermal conductivity $k = 1\,\mathrm{W/m/K}$ and internal heating $q''' = 1200\,\mathrm{W/m^3}$. The exact and computed solutions are shown in Fig. 3.40 for four different meshes and two finite element types (linear: `EDGE2`; quadratic: `EDGE3`).

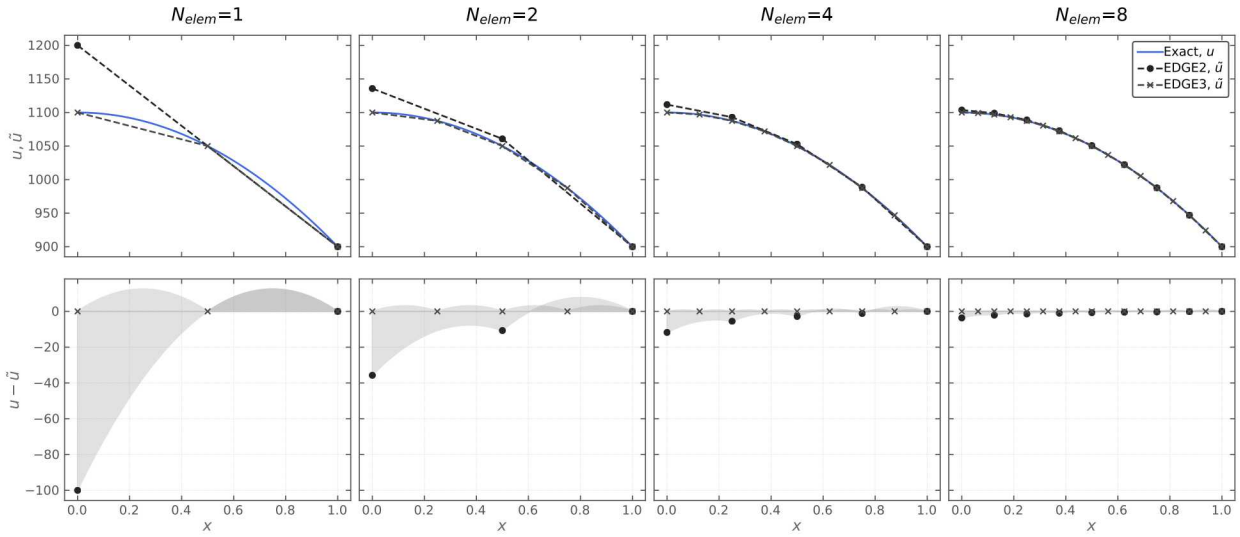

Figure 3.40: Temperature distribution and residuals for Prob. 3.15. Results are shown for the first four meshes. *First row*: exact and FE solutions using 1D elements. *Second row*: residuals between the exact solution and computed solutions.

A convergence study is conducted with a refinement factor of two (i.e., $r_r = 2$). The computed norms for each element type are plotted and tabulated in Fig. 3.41. The formal order of accuracy is two for linear FEs and three for quadratic FEs. In the asymptotic region, the linear FE solutions converges to the exact solution with the correct order of accuracy. The solution computed using quadratic FEs converges immediately to within numerical error due to the quadratic shape of Eq. 3.19.

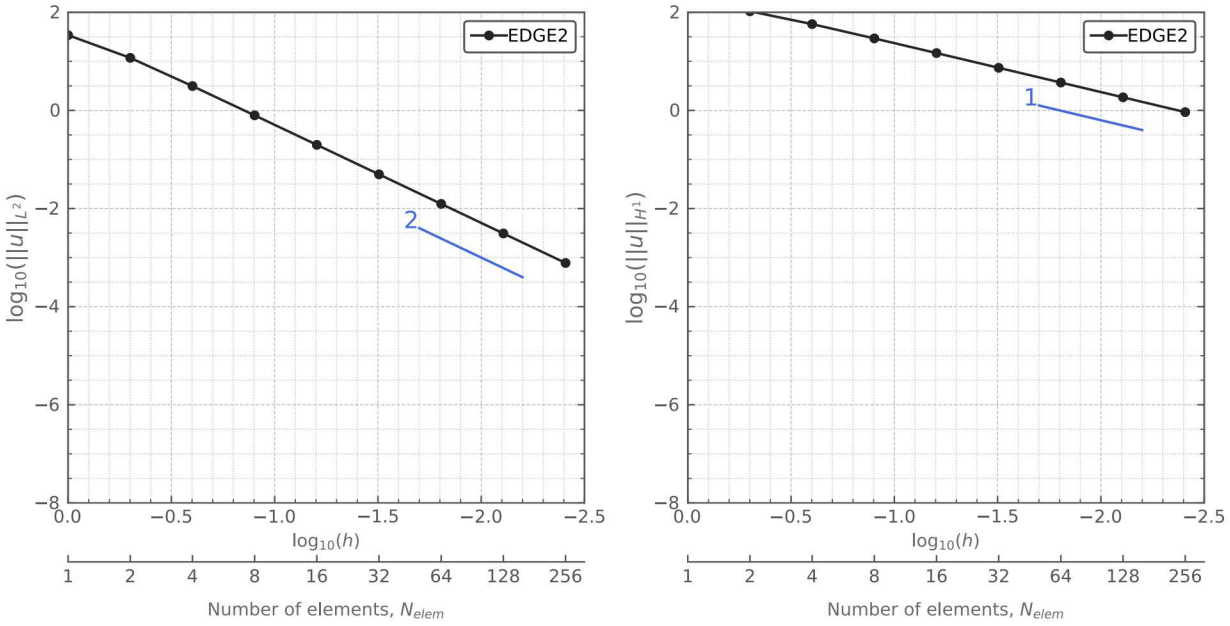

No. Elems	h	**Linear** ($p=1$) $\|\|u\|\|_{L_2}$	**Linear** ($p=1$) $\|\|u\|\|_{H_1}$	**Quadratic** ($p=2$) $\|\|u\|\|_{L_2}$	**Quadratic** ($p=2$) $\|\|u\|\|_{H_1}$
		elem_type=EDGE2		elem_type=EDGE3	
1	1.000000	3.411×10^{1}	1.182×10^{2}	2.879×10^{-9}	9.088×10^{-10}
2	0.500000	1.176×10^{1}	1.047×10^{2}	8.536×10^{-10}	1.056×10^{-8}
4	0.250000	3.127×10^{0}	5.735×10^{1}	1.151×10^{-7}	1.494×10^{-7}
8	0.125000	7.919×10^{-1}	2.932×10^{1}	1.180×10^{-8}	1.495×10^{-7}
16	0.062500	1.985×10^{-1}	1.474×10^{1}	6.380×10^{-12}	6.193×10^{-11}
32	0.031250	4.965×10^{-2}	7.382×10^{0}	9.288×10^{-7}	1.036×10^{-6}
64	0.015625	1.241×10^{-2}	3.692×10^{0}	7.152×10^{-9}	7.016×10^{-9}
128	0.007812	3.104×10^{-3}	1.846×10^{0}	1.020×10^{-7}	7.071×10^{-8}
256	0.003906	7.760×10^{-4}	9.231×10^{-1}	6.153×10^{-6}	4.253×10^{-6}

Figure 3.41: Spatial refinement analysis for Prob. 3.15. Results are computed using 1D elements and a spatial refinement factor $r_r = 2$. The formal order of accuracy is shown for each plot. *Left plot*: the L_2 norm quantifies convergence of the temperature distribution. *Right plot*: the H_1 norm quantifies convergence of the heat flux. *Table*: numerical values used to construct the plots.

Problem 3.16: Spherical shell with internal heating and inside heat flux condition

A spherical shell with inside radius r_i and outside radius r_o has a constant thermal conductivity k and internal heating q'''. It is exposed on its outside surface to a constant temperature $u(r_o) = u_o$ and has a constant heat flux q_i'' applied to its inner surface. The spherical shell reaches thermal equilibrium and the analytic solution for the temperature distribution is ($R = r/r_i$ and $R_o = r_o/r_i$) [29, p.3-10]

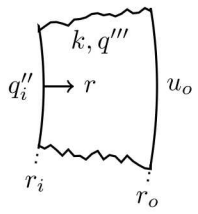

$$u(r) = u_o + \frac{q_i'' r_i}{k}\left[\frac{q''' r_i}{6q_i''}\left(\frac{2(R-R_o)}{RR_o} + R_o^2 - R^2\right) + \frac{R_o - R}{RR_o}\right] \tag{3.20}$$

The problem is solved in BISON on the domain $\boldsymbol{X} \in [0, 1]$. A Neumann boundary condition is used for the inside surface and a Dirichlet condition for the outside surface: $(du/dr)_{r=0.2} = q_i'' = 100\,\mathrm{W/m^2}$ and $u(1) = u_o = 100\,\mathrm{K}$. Steady state heat conduction is considered in the shell with constant thermal conductivity $k = 1\,\mathrm{W/m/K}$ and internal heating $q''' = 1200\,\mathrm{W/m^3}$. The exact and computed solutions are shown in Fig. 3.42 for four different meshes and two finite element types (linear: `EDGE2`; quadratic: `EDGE3`).

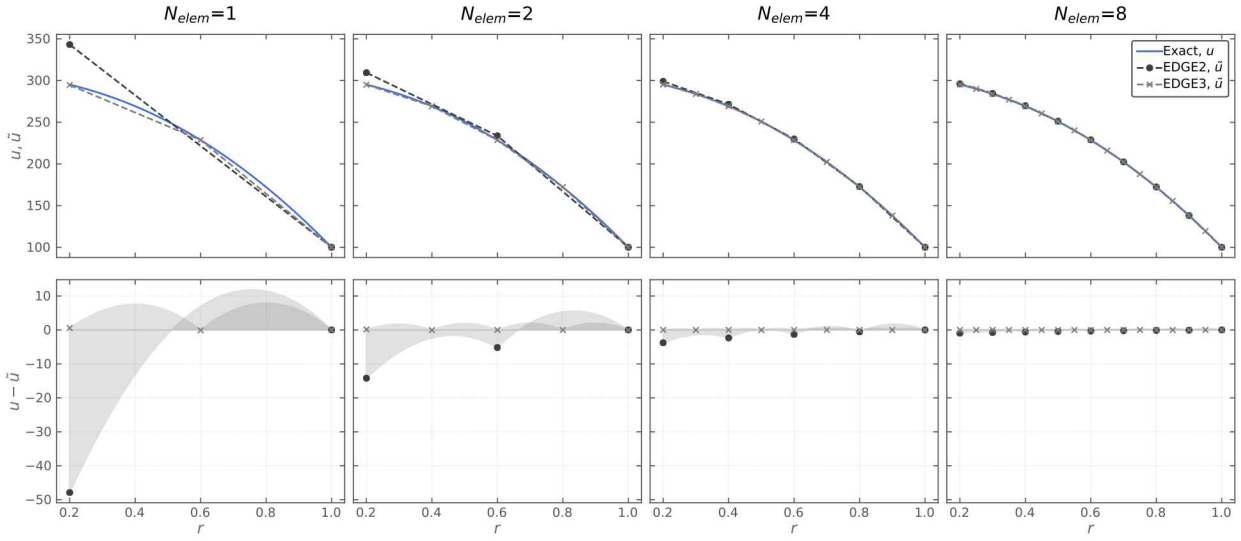

Figure 3.42: Temperature distribution and residuals for Prob. 3.16. Results are shown for the first four meshes. *First row*: exact and FE solutions using 1D elements. *Second row*: residuals between the exact solution and computed solutions.

A convergence study is conducted with a refinement factor of two (i.e., $r_r = 2$). The computed norms for each element type are plotted and tabulated in Fig. 3.43. The formal order of accuracy is two for linear FEs and three for quadratic FEs. In the asymptotic region, the linear and quadratic FE solutions converge to the exact solution with the correct order of accuracy.

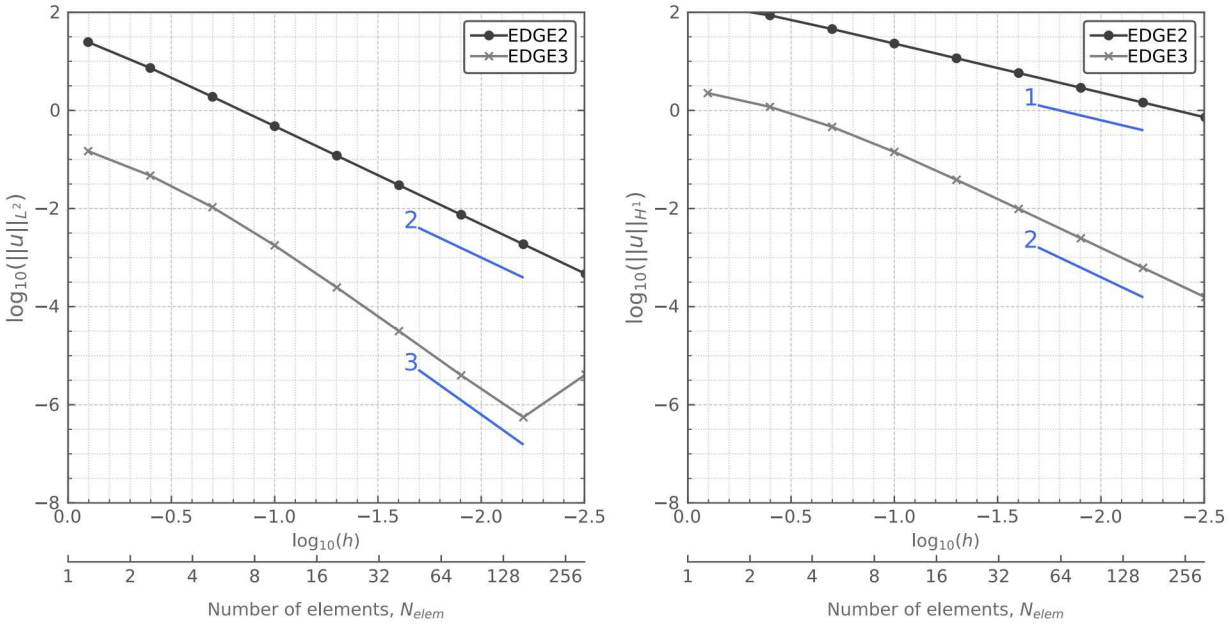

No. Elems	h	**Linear** ($p=1$) $\|\|u\|\|_{L_2}$	**Linear** ($p=1$) $\|\|u\|\|_{H_1}$	**Quadratic** ($p=2$) $\|\|u\|\|_{L_2}$	**Quadratic** ($p=2$) $\|\|u\|\|_{H_1}$
		elem_type=EDGE2		elem_type=EDGE3	
1	0.800000	2.468×10^{1}	1.361×10^{2}	1.477×10^{-1}	2.249×10^{0}
2	0.400000	7.314×10^{0}	8.649×10^{1}	4.699×10^{-2}	1.180×10^{0}
4	0.200000	1.892×10^{0}	4.546×10^{1}	1.065×10^{-2}	4.607×10^{-1}
8	0.100000	4.769×10^{-1}	2.301×10^{1}	1.771×10^{-3}	1.423×10^{-1}
16	0.050000	1.195×10^{-1}	1.154×10^{1}	2.460×10^{-4}	3.843×10^{-2}
32	0.025000	2.989×10^{-2}	5.773×10^{0}	3.200×10^{-5}	9.828×10^{-3}
64	0.012500	7.474×10^{-3}	2.887×10^{0}	3.986×10^{-6}	2.472×10^{-3}
128	0.006250	1.868×10^{-3}	1.444×10^{0}	5.573×10^{-7}	6.190×10^{-4}
256	0.003125	4.670×10^{-4}	7.218×10^{-1}	4.133×10^{-6}	1.550×10^{-4}

Figure 3.43: Spatial refinement analysis for Prob. 3.16. Results are computed using 1D elements and a spatial refinement factor $r_r = 2$. The formal order of accuracy is shown for each plot. *Left plot*: the L_2 norm quantifies convergence of the temperature distribution. *Right plot*: the H_1 norm quantifies convergence of the heat flux. *Table*: numerical values used to construct the plots.

Problem 3.17: MMS for one dimensional conduction

Steady state one-dimensional heat conduction is analyzed using the manufactured solution $u(x) = \sin(a\pi x)$. This simple function is suitable for use in an MMS problem because it is continuous and infinitely differentiable. To find the source term Q that produces the solution u, the steady state heat conduction operator ($k = 1$)—$\mathcal{L} = \nabla \cdot \nabla$—is applied to u. This results in the source term

$$Q = \mathcal{L}(u) = a^2\pi^2 \sin(a\pi x). \tag{3.21}$$

The problem is solved in BISON using the diffusion module on the domain $\boldsymbol{X} \in [0, 1]$. The manufactured solution is shown in Fig. 3.44 with $a = 2$, which is the value used in the BISON implementation. Steady state heat conduction is considered through a homogeneous solid using the external source in Eq. 3.21. MMS studies allow the same problem to be tested using a variety of different boundary conditions. Two cases are examined in this study: (I) Dirichlet–Dirichlet and (II) Dirichlet–Neumann.

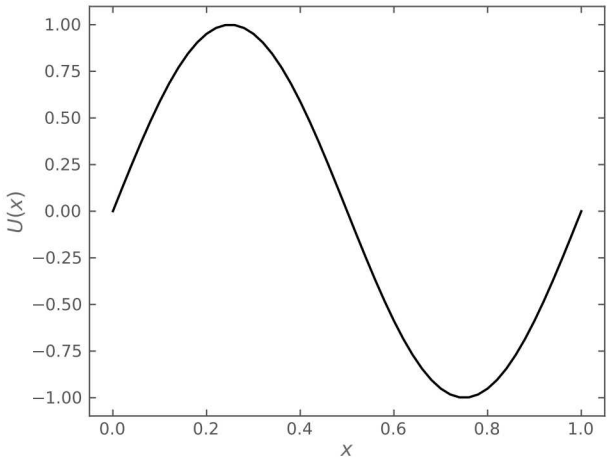

Figure 3.44: The exact solution for MMS Prob. 3.17

Case I (Dirichlet–Dirichlet): Dirichlet boundary conditions are derived from the manufactured solution with $a = 2$. This results in the boundary conditions $u(0) = 0$ and $u(1) = 0$.

Case II (Dirichlet–Neumann): The boundary conditions are derived from the manufactured solution with $a = 2$. This results in the boundary conditions $u(0) = 0$ and $(du/dx)_{x=1} = 2\pi$.

For Case I, the exact and computed solutions are shown in Fig. 3.45 for four different meshes and two finite element types (linear: `EDGE2`; quadratic: `EDGE3`). A convergence study is conducted with a refinement factor of two ($r_x = 2$). The computed norms for each FE type and boundary condition type are plotted in Fig. 3.46 and shown in Table 3.2. The formal order of accuracy is two for linear FEs and three for quadratic FEs. In the asymptotic region for both cases, the linear and quadratic FE solutions converge to the exact solution with the correct order of accuracy.

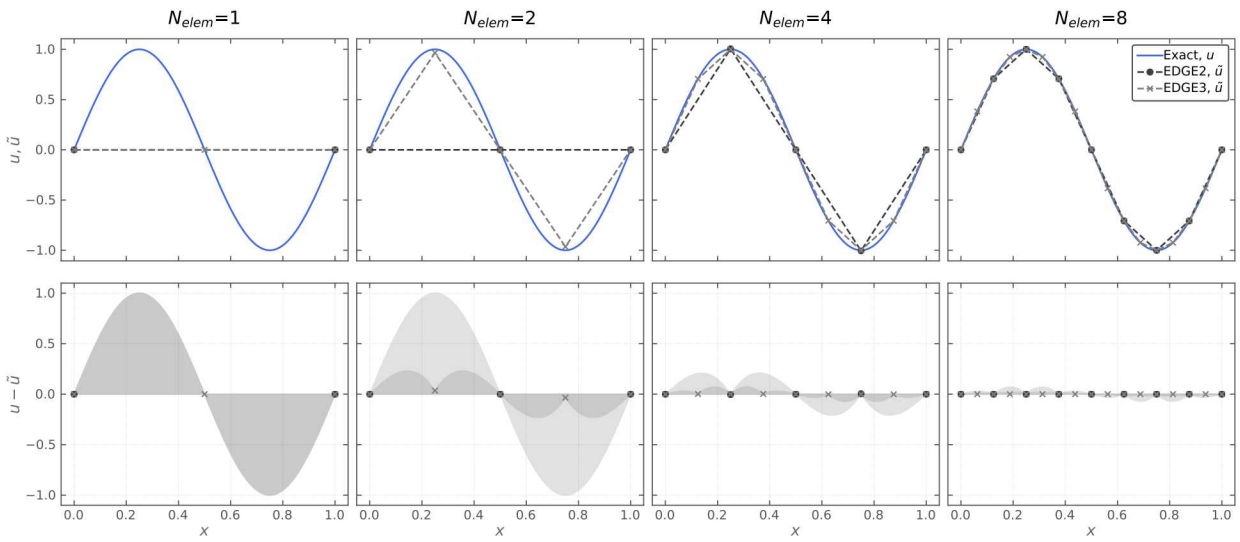

Figure 3.45: Temperature distribution and residuals for Prob. 3.17 (Case I). Results are shown for the first four meshes. *First row*: exact and FE solutions using 1D elements. *Second row*: residuals between the exact and computed solutions.

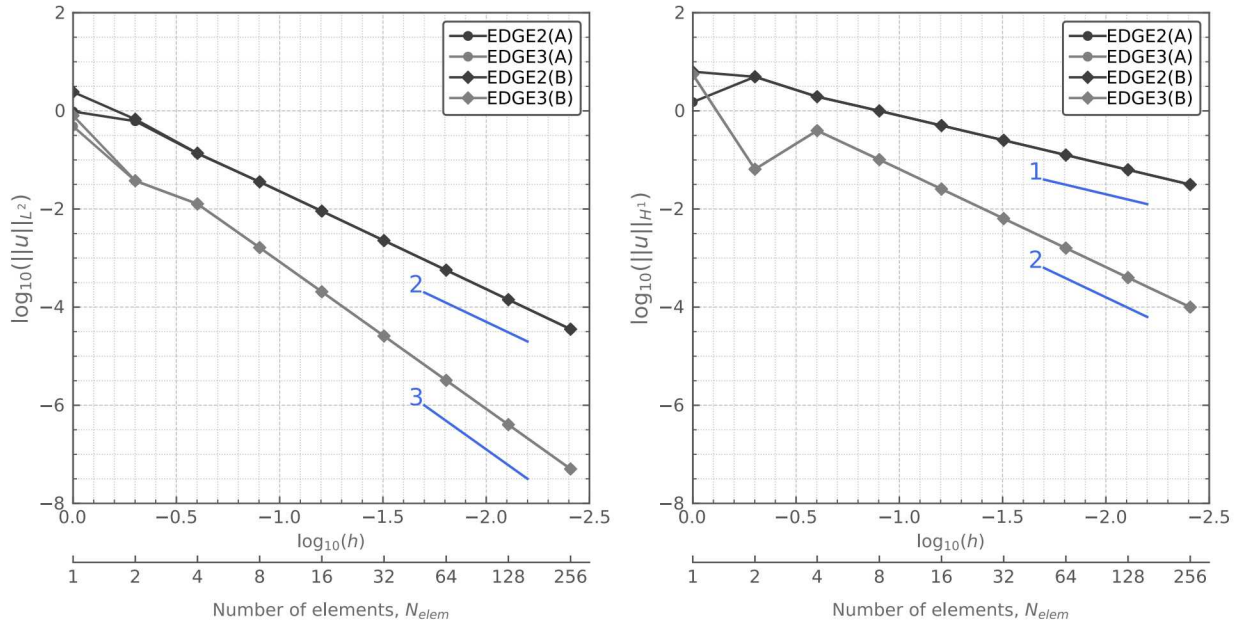

Figure 3.46: Spatial refinement analysis for Prob. 3.17. Results are computed using 1D elements and a spatial refinement factor $r_x = 2$. The formal orders of accuracy are shown. FE types with an A indicate Case I (Dirichlet–Dirichlet) and with a B indicate Case II (Dirichlet–Neumann). *Left plot*: the L_2 norm quantifies convergence of the temperature. *Right plot*: the H_1 norm quantifies convergence of the heat flux.

Table 3.2: Norms calculated for Prob. 3.17. Two norms are computed: (1) L_2 norm quantifies convergence of temperature and (2) H_1 norm quantifies convergence of the heat flux.

No. Elems	h	**Linear** ($p = 1$) $\|\|u\|\|_{L_2}$	$\|\|u\|\|_{H_1}$	**Quadratic** ($p = 2$) $\|\|u\|\|_{L_2}$	$\|\|u\|\|_{H_1}$
		elem_type=EDGE2		elem_type=EDGE3	
Case I (Dirichlet–Dirichlet)					
1	1.000000	9.706×10^{-1}	1.512×10^{0}	4.848×10^{-1}	5.495×10^{0}
2	0.500000	6.162×10^{-1}	4.949×10^{0}	3.743×10^{-2}	6.464×10^{-2}
4	0.250000	1.347×10^{-1}	1.946×10^{0}	1.270×10^{-2}	3.961×10^{-1}
8	0.125000	3.565×10^{-2}	9.987×10^{-1}	1.633×10^{-3}	1.014×10^{-1}
16	0.062500	9.043×10^{-3}	5.026×10^{-1}	2.055×10^{-4}	2.549×10^{-2}
32	0.031250	2.269×10^{-3}	2.517×10^{-1}	2.574×10^{-5}	6.380×10^{-3}
64	0.015625	5.678×10^{-4}	1.259×10^{-1}	3.219×10^{-6}	1.596×10^{-3}
128	0.007812	1.420×10^{-4}	6.296×10^{-2}	4.024×10^{-7}	3.990×10^{-4}
256	0.003906	3.550×10^{-5}	3.148×10^{-2}	5.030×10^{-8}	1.000×10^{-4}
Case II (Dirichlet–Neumann)					
1	1.000000	2.424×10^{0}	6.290×10^{0}	7.993×10^{-1}	5.567×10^{0}
2	0.500000	6.748×10^{-1}	4.953×10^{0}	3.770×10^{-2}	6.479×10^{-2}
4	0.250000	1.371×10^{-1}	1.946×10^{0}	1.270×10^{-2}	3.961×10^{-1}
8	0.125000	3.578×10^{-2}	9.987×10^{-1}	1.633×10^{-3}	1.014×10^{-1}
16	0.062500	9.051×10^{-3}	5.026×10^{-1}	2.055×10^{-4}	2.549×10^{-2}
32	0.031250	2.270×10^{-3}	2.517×10^{-1}	2.574×10^{-5}	6.380×10^{-3}
64	0.015625	5.678×10^{-4}	1.259×10^{-1}	3.219×10^{-6}	1.596×10^{-3}
128	0.007812	1.420×10^{-4}	6.296×10^{-2}	4.024×10^{-7}	3.990×10^{-4}
256	0.003906	3.550×10^{-5}	3.148×10^{-2}	5.030×10^{-8}	1.000×10^{-4}

Problem 3.18: MMS for two dimensional conduction

Steady state two-dimensional heat conduction is analyzed using the manufactured solution $u(x, y) = \sin(a\pi x)\sin(b\pi y)$. This simple function is suitable for use as an MMS problem because it is continuous and infinitely differentiable. To find the source term Q that produces the solution u, the steady state heat conduction operator (with $k = 1$)—$\mathcal{L} = \nabla \cdot \nabla$—is applied to u. This results in the source term

$$Q(x, y) = \mathcal{L}(u) = (a^2 + b^2)\pi^2 \sin(a\pi x)\sin(b\pi y). \tag{3.22}$$

The problem is solved in BISON using the diffusion module on the domain $\boldsymbol{X} \in [0, 1]^2$. The manufactured solution is shown in Fig. 3.47 with $a = b = 2$, which is the value used in the BISON implementation. Dirichlet boundary conditions are derived from the manufactured solution: $u(0, y) = u(1, y) = u(x, 0) = u(x, 1) = 0$. Steady state heat conduction is considered through the homogeneous solid using the external source in Eq. 3.22.

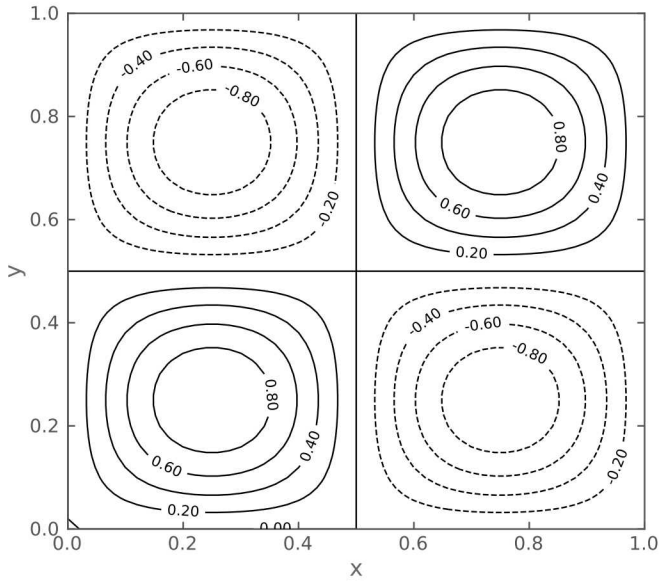

Figure 3.47: The exact solution for Prob. 3.18

Fig. 3.48 shows the convergence of two FE choices as the two-dimensional mesh is refined (`QUAD4` and `TRI3`).

Fig. 3.49 shows a comparison of the two-dimensional solutions with 32×32 elements using a variety of FE types (linear: `QUAD4`, `TRI3`; quadratic: `QUAD8`, `QUAD9`, `TRI6`). Regardless of the chosen FE shape, the BISON solution has the correct shape, indicating that each two-dimensional FE option is implemented correctly.

A convergence study is conducted with a refinement factor of two ($r_x = r_y = 2$). The computed norms for each FE type are plotted in Fig. 3.50. The formal order of accuracy is two for linear FEs and three for quadratic FEs. In the asymptotic region for all FE types, the solutions converge to the exact solution with the correct order of accuracy.

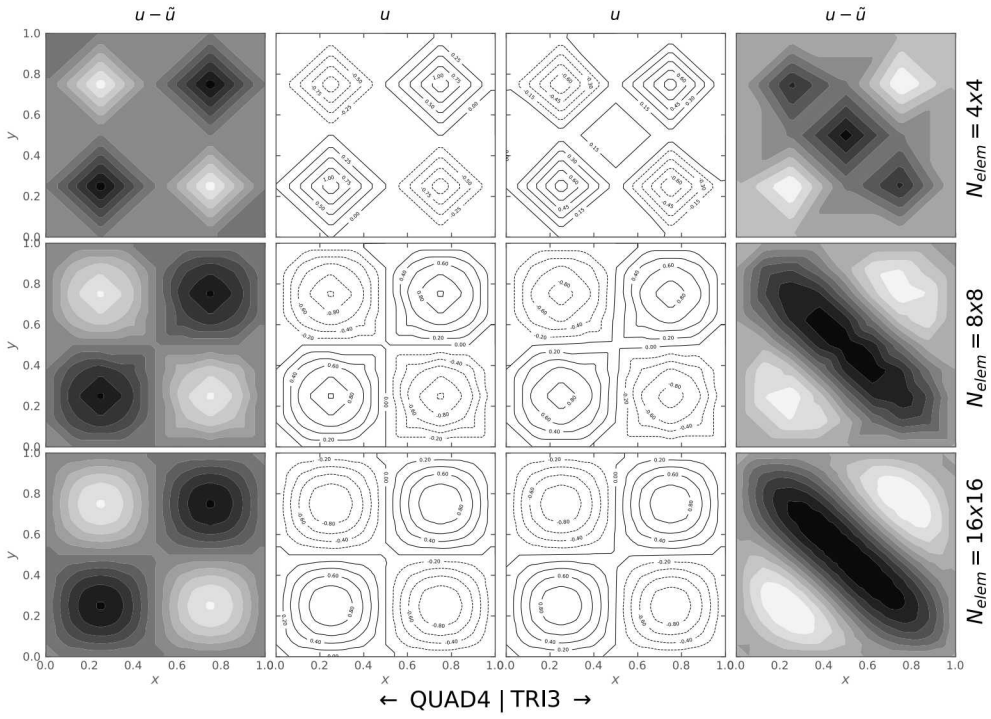

Figure 3.48: Temperature distributions and residuals for Prob. 3.18 with three different meshes (left: `QUAD4`; right: `TRI3`). *Center columns*: the FE solutions using a variety of 2D meshes. *Outside columns*: residuals between the approximate solution and the computed solutions, where darker colors indicate a less accurate computed solution.

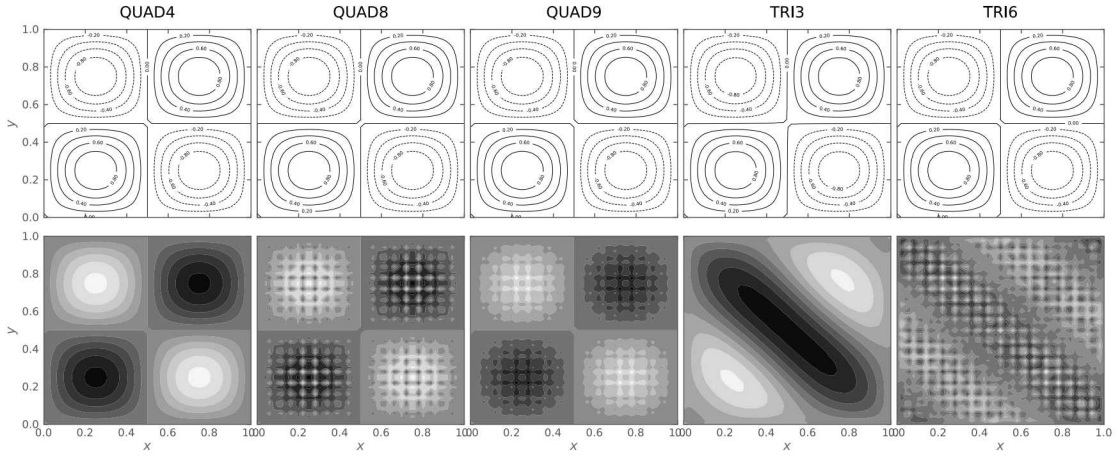

Figure 3.49: Temperature distributions and residuals for Prob. 3.18 with different FE types. Results are shown for five FE types. *First row*: the FE solutions using 32×32 2D elements. *Second row*: residuals between the approximate solution and the computed solutions, where darker colors indicate a less accurate computed solution.

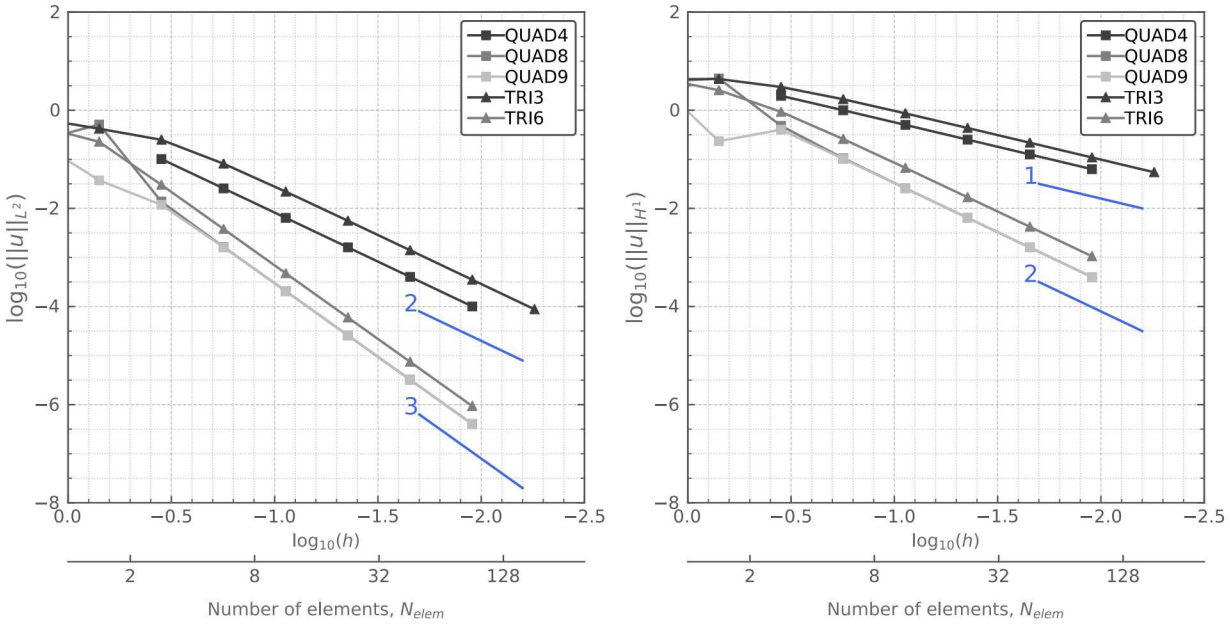

No. Elems	$\sqrt{h}$	**Linear** ($p=1$) $\|\|u\|\|_{L_2}$	**Linear** ($p=1$) $\|\|u\|\|_{H_1}$	**Quadratic** ($p=2$) $\|\|u\|\|_{L_2}$	**Quadratic** ($p=2$) $\|\|u\|\|_{H_1}$	$\|\|u\|\|_{L_2}$	$\|\|u\|\|_{H_1}$
		elem_type=`QUAD4`		elem_type=`QUAD8`		elem_type=`QUAD9`	
1	1.000000	9.421×10^{-1}	2.075×10^{0}	2.350×10^{-1}	3.768×10^{0}	2.350×10^{-1}	3.768×10^{0}
4	0.500000			5.112×10^{-1}	4.442×10^{0}	3.724×10^{-2}	0.235×10^{0}
16	0.250000	1.013×10^{-1}	1.966×10^{0}	1.376×10^{-2}	4.814×10^{-1}	1.181×10^{-2}	4.024×10^{-1}
64	0.125000	2.552×10^{-2}	9.993×10^{-1}	1.636×10^{-3}	1.051×10^{-1}	1.610×10^{-3}	1.018×10^{-1}
256	0.062500	6.413×10^{-3}	5.026×10^{-1}	2.056×10^{-4}	2.569×10^{-2}	2.049×10^{-4}	2.552×10^{-2}
1024	0.031250	1.606×10^{-3}	2.517×10^{-1}	2.574×10^{-5}	6.393×10^{-3}	2.572×10^{-5}	6.382×10^{-3}
4096	0.015625	4.015×10^{-4}	1.259×10^{-1}	3.219×10^{-6}	1.596×10^{-3}	3.218×10^{-6}	1.596×10^{-3}
16384	0.007812	1.004×10^{-4}	6.296×10^{-2}	4.024×10^{-7}	3.990×10^{-4}	4.024×10^{-7}	3.990×10^{-4}
		elem_type=`TRI3`		elem_type=`TRI6`			
2	1.000000	6.824×10^{-1}	4.279×10^{0}	4.874×10^{-1}	4.594×10^{0}		
8	0.500000	4.197×10^{-1}	4.331×10^{0}	2.270×10^{-1}	2.560×10^{0}		
32	0.250000	2.499×10^{-1}	2.983×10^{0}	3.018×10^{-2}	9.251×10^{-1}		
128	0.125000	8.136×10^{-2}	1.674×10^{0}	3.796×10^{-3}	2.585×10^{-1}		
512	0.062500	2.189×10^{-2}	8.632×10^{-1}	4.759×10^{-4}	6.677×10^{-2}		
2048	0.031250	5.578×10^{-3}	4.350×10^{-1}	5.957×10^{-5}	1.684×10^{-2}		
8192	0.015625	1.401×10^{-3}	2.179×10^{-1}	7.451×10^{-6}	4.219×10^{-3}		
32768	0.007812	3.507×10^{-4}	1.090×10^{-1}	9.315×10^{-7}	1.055×10^{-3}		

Figure 3.50: Spatial refinement analysis for Prob. 3.18. Results are computed using 1D elements and a spatial refinement factor $r_x = 2$. The formal order of accuracy is shown for each plot. *Left plot*: the L_2 norm quantifies convergence of the temperature distribution. *Right plot*: the H_1 norm quantifies convergence of the heat flux. *Table*: numerical values used to construct the plots.

Problem 3.19: MMS for transient conduction

Transient one-dimensional heat conduction is analyzed using the manufactured solution $u(x,t) = axt^3$. This simple function is suitable for use as an MMS solution because it is continuous and infinitely differentiable. To find the source term Q that produces the solution u, the transient heat conduction operator (with $k = 1$)—$\mathcal{L} = \partial/\partial t + \nabla \cdot \nabla$—is applied to u. Note that there is no contribution from the spatial derivative, since $d^2u/dx^2 = 0$. This results in the source term

$$Q(x,t) = \mathcal{L}(u) = 3axt^2. \tag{3.23}$$

Note that this MMS problem is inherited from MOOSE. The problem is solved in BISON using the diffusion module on the domain $\boldsymbol{X} \in [0,1]$ and $\boldsymbol{T} \in [0,3]$. A Dirichlet boundary condition and an initial condition are derived from the manufactured solution: $u(0,t) = 0$ and $u(x,0) = 0$. The manufactured solution is shown in Fig. 3.51 with $a = 1$, which is the value used in the BISON implementation. Transient heat conduction is considered through the homogeneous solid using the external source in Eq. 3.23.

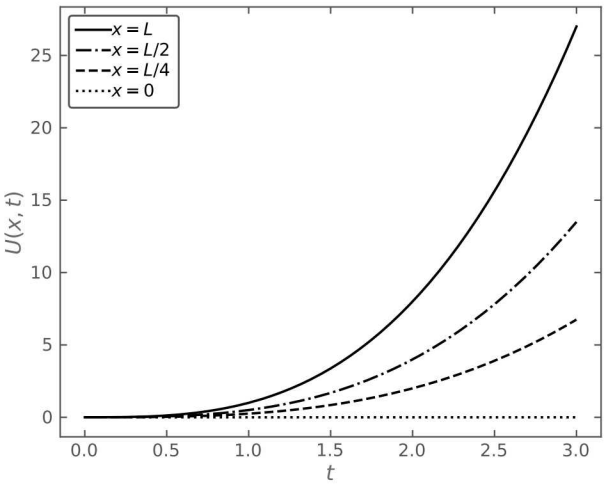

Figure 3.51: The exact solution solution for Prob. 3.19

A convergence study is conducted with a temporal refinement factor of two (i.e., $r_x = 2$). Linear finite elements are used for all cases (`EDGE2`) with 32 FEs. Norms are computed at the final time step; computed norms for each choice of temporal discretization are plotted in Fig. 3.52 and shown in Table 3.3. Since the explicit Euler method requires enforcement of the von Neumann stability limit, no simulations are run with a time step which would result in $Fo < 0.5$. In the asymptotic region, all choices of temporal discretization have the correct order of accuracy.

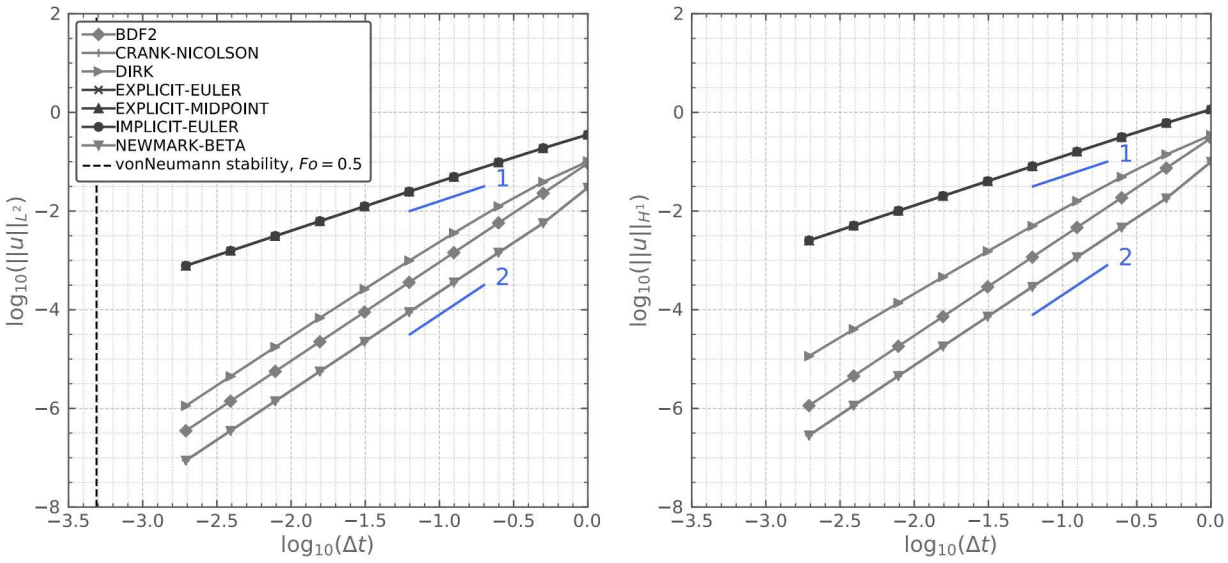

Figure 3.52: Temporal refinement analysis for Prob. 3.19. Results are computed using 1D elements and a temporal refinement factor $r_t = 2$. The von Naumann stability criteria ($Fo = 0.5$) is shown as a vertical dashed line. The formal orders of accuracy are shown. *Left plot*: the L_2 norm quantifies the convergence of the temperature. *Right plot*: the H_1 norm quantifies convergence of the heat flux.

Table 3.3: Norms calculated for Prob. 3.19. Two norms are computed: (1) L_2 norm quantifies convergence of temperature and (2) H_1 norm quantifies convergence of the heat flux.

Δt	Fo	$\|\|u\|\|_{L_2}$	$\|\|u\|\|_{H_1}$	$\|\|u\|\|_{L_2}$	$\|\|u\|\|_{H_1}$
		`explicit-Euler` $(p=1)$		`explicit-midpoint` $(p=1)$	
1.000000	1024	3.540×10^{-1}	1.149×10^{0}	3.540×10^{-1}	1.149×10^{0}
0.500000	512	1.885×10^{-1}	6.119×10^{-1}	1.885×10^{-1}	6.119×10^{-1}
0.250000	256	9.710×10^{-2}	3.153×10^{-1}	9.710×10^{-2}	3.153×10^{-1}
0.125000	128	4.927×10^{-2}	1.600×10^{-1}	4.927×10^{-2}	1.600×10^{-1}
0.062500	64	2.482×10^{-2}	8.056×10^{-2}	2.482×10^{-2}	8.056×10^{-2}
0.031250	32	1.245×10^{-2}	4.043×10^{-2}	1.245×10^{-2}	4.043×10^{-2}
0.015625	16	6.237×10^{-3}	2.025×10^{-2}	6.237×10^{-3}	2.025×10^{-2}
0.007812	8	3.121×10^{-3}	1.013×10^{-2}	3.121×10^{-3}	1.013×10^{-2}
0.003906	4	1.561×10^{-3}	5.069×10^{-3}	1.561×10^{-3}	5.069×10^{-3}
0.001953	2	7.810×10^{-4}	2.535×10^{-3}	7.810×10^{-4}	2.535×10^{-3}
		`implicit-Euler` $(p=1)$		`bdf2` $(p=2)$	
1.000000	1024	3.540×10^{-1}	1.149×10^{0}	9.274×10^{-2}	3.004×10^{-1}
0.500000	512	1.885×10^{-1}	6.119×10^{-1}	2.297×10^{-2}	7.446×10^{-2}
0.250000	256	9.710×10^{-2}	3.153×10^{-1}	5.746×10^{-3}	1.862×10^{-2}
0.125000	128	4.927×10^{-2}	1.600×10^{-1}	1.436×10^{-3}	4.656×10^{-3}
0.062500	64	2.482×10^{-2}	8.056×10^{-2}	3.591×10^{-4}	1.164×10^{-3}
0.031250	32	1.245×10^{-2}	4.043×10^{-2}	8.977×10^{-5}	2.910×10^{-4}
0.015625	16	6.237×10^{-3}	2.025×10^{-2}	2.244×10^{-5}	7.300×10^{-5}
0.007812	8	3.121×10^{-3}	1.013×10^{-2}	5.610×10^{-6}	1.800×10^{-5}
0.003906	4	1.561×10^{-3}	5.069×10^{-3}	1.402×10^{-6}	5.000×10^{-6}
0.001953	2	7.810×10^{-4}	2.535×10^{-3}	3.500×10^{-7}	1.000×10^{-6}
		`Crank-Nicolson` $(p=2)$		`Dirk` $(p=2)$	
1.000000	1024	2.990×10^{-2}	9.943×10^{-2}	1.011×10^{-1}	3.455×10^{-1}
0.500000	512	5.687×10^{-3}	1.810×10^{-2}	3.877×10^{-2}	1.403×10^{-1}
0.250000	256	1.436×10^{-3}	4.638×10^{-3}	1.237×10^{-2}	4.887×10^{-2}
0.125000	128	3.591×10^{-4}	1.163×10^{-3}	3.585×10^{-3}	1.588×10^{-2}
0.062500	64	8.978×10^{-5}	2.910×10^{-4}	9.837×10^{-4}	4.976×10^{-3}
0.031250	32	2.244×10^{-5}	7.274×10^{-5}	2.614×10^{-4}	1.526×10^{-3}
0.015625	16	5.611×10^{-6}	1.819×10^{-5}	6.805×10^{-5}	4.607×10^{-4}
0.007812	8	1.401×10^{-6}	4.542×10^{-6}	1.749×10^{-5}	1.371×10^{-4}
0.003906	4	3.505×10^{-7}	1.135×10^{-6}	4.455×10^{-6}	4.013×10^{-5}
0.001953	2	8.825×10^{-8}	2.860×10^{-7}	1.128×10^{-6}	1.148×10^{-5}
		`newmark-beta` $(p=2)$			
1.000000	1024	2.990×10^{-2}	9.943×10^{-2}		
0.500000	512	5.687×10^{-3}	1.810×10^{-2}		
0.250000	256	1.436×10^{-3}	4.638×10^{-3}		
0.125000	128	3.591×10^{-4}	1.163×10^{-3}		
0.062500	64	8.978×10^{-5}	2.910×10^{-4}		
0.031250	32	2.244×10^{-5}	7.274×10^{-5}		
0.015625	16	5.612×10^{-6}	1.819×10^{-5}		
0.007812	8	1.401×10^{-6}	4.542×10^{-6}		
0.003906	4	3.508×10^{-7}	1.135×10^{-6}		
0.001953	2	8.891×10^{-8}	2.888×10^{-7}		

3.2 Gap Heat Transfer

The previous section considered problems for verification of the basic heat conduction equation in BISON. However, these problems are not representative of fuel in nuclear reactors. Particularly for LWR fuel, nuclear fuel rods consist of column of fuel pellets surrounded by a hollow tube called the *cladding*. To obtain an analytic solution, the fuel is assumed to be located at the center of the cladding and the void is filled with an inert gas [9]. If constant solid properties are considered, temperature jumps across the gap and cladding can be obtained using the identity of continuous heat flux. This allows the formation of an analytic solution that is more representative of typical fuel rods.

The temperature jump across the gap in BISON is computed as a summation of heat transfers: fill gas conductance h_g, contact conductance h_c, and radiative conductance h_r [3, 38, 39, 40, 41, 42]:

$$h_{gap} = h_g + h_c + h_r, \tag{3.24a}$$

where

$$h_g = \begin{cases} \dfrac{k_{gas}}{d + g_1 + g_2} & \text{plane} \\ \dfrac{k_{gas}}{r_1 \left(\ln\left(\frac{r_2}{r_1}\right) + \frac{g_1}{r_1} + \frac{g_2}{r_2} \right)} & \text{cylinder} \\ \dfrac{k_{gas}}{r_1^2 \left(\left[\frac{1}{r_1} - \frac{1}{r_2}\right] + \frac{g_1}{r_1^2} + \frac{g_2}{r_2^2} \right)} & \text{sphere} \end{cases}, \tag{3.24b}$$

$$h_c = C \frac{\Lambda}{r_a} \left(\frac{W}{H} \right), \tag{3.24c}$$

$$h_r = \frac{\sigma_{SB}(T_1^2 + T_2^2)(T_1 + T_2)}{\dfrac{1}{\varepsilon_1} + \left(\dfrac{1}{\varepsilon_2} - 1 \right)}. \tag{3.24d}$$

where k_{gas} is the fill gas thermal conductivity, d is the gap distance, g_i is the temperature jump distance, Λ is the harmonic mean of thermal conductivities of the surrounding solids, r_a is the contact radius that is defined as a function of the surface roughnesses, W is the load on the contact interface, H is the Meyer's hardness of the softer material, σ_{SB} is the Stefan-Boltzmann constant, T_i is temperature, ε_i is the emissivity, and r_i is the radius for the solid bodies $i = 1, 2$ ($r_1 < r_2$).

The problems in this chapter focus on testing the gap heat transfer for an open gap. To simplify the analytic solution, radiative heat transfer is ignored by setting emissivities to zero and temperature jump distances are set to zero through BISON input. Thus, the gap heat transfer reduces to the fill gas conductance h_g:

$$h_{gap} = h_g = \begin{cases} \dfrac{k_{gas}}{d} & \text{plane} \\ \dfrac{k_{gas}}{r_1 \ln\left(\frac{r_2}{r_1}\right)} & \text{cylinder} \\ \dfrac{k_{gas}}{r_1^2\left[\frac{1}{r_1} - \frac{1}{r_2}\right]} & \text{sphere} \end{cases} \tag{3.25}$$

The validation matrix for this physics is shown in Table 3.4. The cylindrical example is taken from [9] and the other two are derived for this report.

Table 3.4: Verification matrix for BISON gap heat transfer

	Reference	Transient		Coordinate System			Dimension			Properties and External Sources						Boundary Conditions		
		Transient	Steady State	Cartesian	Cylindrical	Spherical	x_1	x_2	x_3	k_c	$k(T)$	q'''	$q'''(\vec{x})$	α_c	$\alpha(T)$	Drichlet	Neumann	Convective
Method of Exact Solutions																		
3.20			✓	✓			✓			✓		✓				✓	✓	
3.21	[9]		✓		✓		✓			✓		✓				✓	✓	
3.22			✓			✓	✓			✓		✓				✓	✓	

Problem 3.20: Cartesian gap heat transfer

An infinitely long fuel plate has constant thermal conductivity k and internal heat generation q'''. It is insulated on its left surface and exposed on its right surface to some constant temperature $u(r_{co}) = u_{co}$. The temperature jump across the gap and cladding is

$$u_f - u_{co} = \frac{q'}{x_f h_{gap}} + \frac{q' x_f (x_{co} - x_{ci})}{k_c}, \tag{3.26a}$$

where u_f is the fuel surface temperature, u_{co} is the cladding outside temperature, and k_c is the cladding thermal conductivity. The gap conductance h_{gap} reduces to k_{gas}/d, where k_{gas} is the thermal conductivity of the fill gas. The analytic solution for the temperature distribution in the fuel is

$$u(x) = u_f + \frac{\dot{q}}{2k_f}\left(1 - \frac{x^2}{x_f^2}\right), \tag{3.26b}$$

where x_f is the fuel surface and k_f is the fuel thermal conductivity.

The problem is run in BISON using two blocks: the fuel domain on in $\boldsymbol{X} \in [0, 1.0]$ and the clad domain in $\boldsymbol{X} \in [1.1, 1.2]$. The domain between the two blocks is filled with an inert gas with a predefined gas thermal conductivity. Neumann and Dirichlet boundary conditions are applied: $(du/dx)_{x=0} = 0$ and $u(x_{co}) = u_0$. Steady state heat conduction is considered with the following constants: fuel thermal conductivity $k_f = 10\,\mathrm{W/m/K}$, cladding thermal conductivity $k_c = 10\,\mathrm{W/m/K}$, volumetric heat generation $q''' = 400\,\mathrm{W/m^3}$, gas thermal conductivity $k_{gas} = 0.1\,\mathrm{W/m/K}$, and Biot number $Bi \approx 0.1$.

The exact and computed solutions are shown in Fig. 3.53 for three meshes and two FE types (linear: `EDGE2`; quadratic: `EDGE3`). A convergence study is performed with a refinement factor of two ($r_x = 2$). The mesh refinements are performed uniformly in both the fuel and cladding domains; however, the

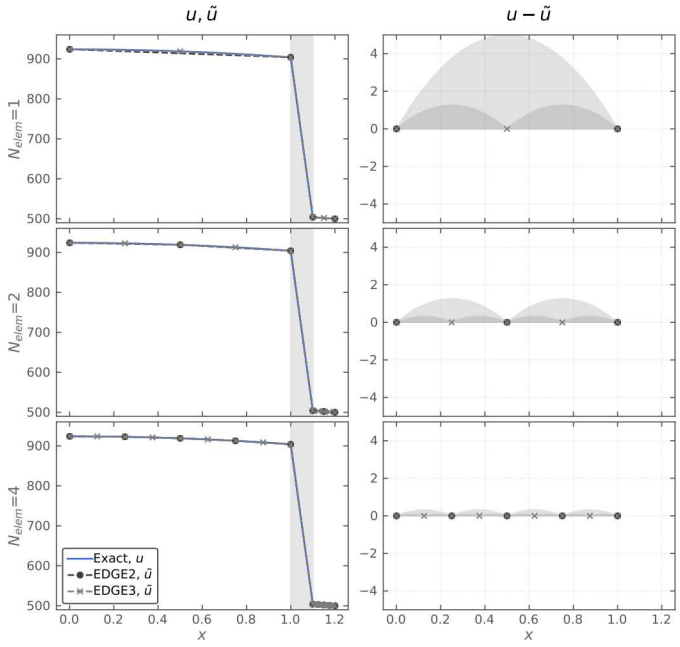

Figure 3.53: Temperature distribution and residuals for Prob. 3.20. Results are shown for the first three meshes. *First column*: exact and FE solutions using 1D elements. *Second column*: residuals are computed between the exact and computed solutions.

norms are computed only in the fuel domain. The computed norms are plotted and tabulated in Fig. 3.54. The linear FE solution is second order accurate, as expected. The quadratic solution is within numerical error of the exact solution due to its quadratic shape.

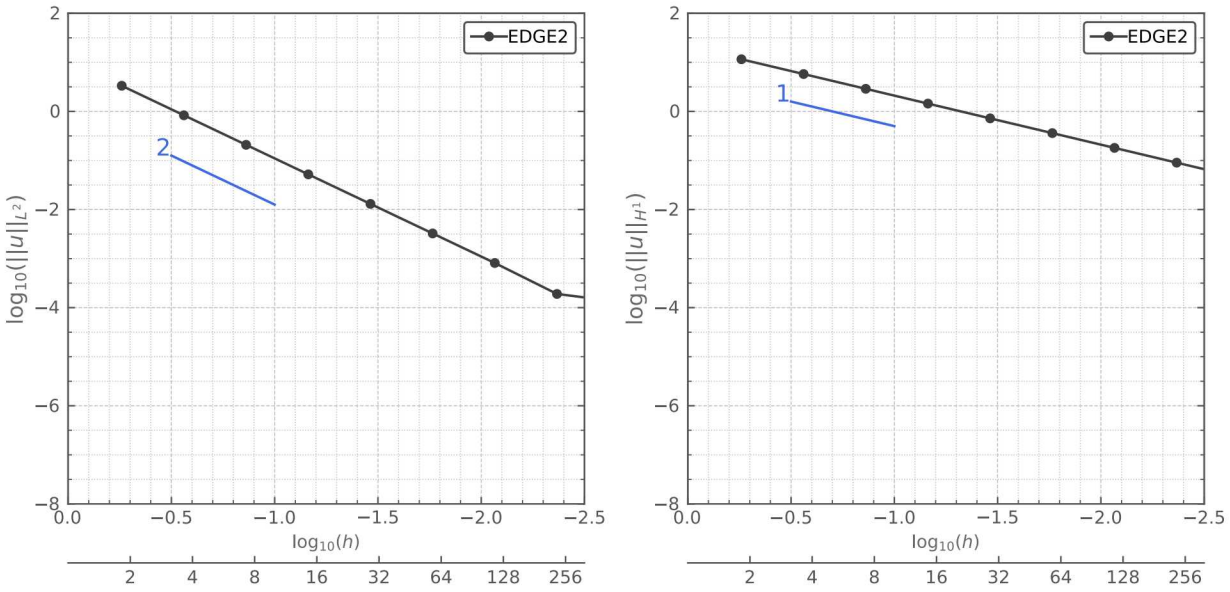

No. Elems	h	**Linear** ($p=1$) $\|\|u\|\|_{L_2}$	**Linear** ($p=1$) $\|\|u\|\|_{H_1}$	**Quadratic** ($p=2$) $\|\|u\|\|_{L_2}$	**Quadratic** ($p=2$) $\|\|u\|\|_{H_1}$
		elem_type=EDGE2		elem_type=EDGE3	
2	0.550000	3.333×10^{0}	1.155×10^{1}	1.224×10^{-11}	7.187×10^{-11}
4	0.275000	8.333×10^{-1}	5.774×10^{0}	5.260×10^{-8}	3.482×10^{-7}
8	0.137500	2.083×10^{-1}	2.887×10^{0}	1.523×10^{-8}	3.908×10^{-9}
16	0.068750	5.208×10^{-2}	1.443×10^{0}	2.420×10^{-7}	2.586×10^{-6}
32	0.034375	1.302×10^{-2}	7.217×10^{-1}	3.378×10^{-5}	1.794×10^{-6}
64	0.017188	3.255×10^{-3}	3.608×10^{-1}	4.801×10^{-4}	2.772×10^{-5}
128	0.008594	8.130×10^{-4}	1.804×10^{-1}	2.082×10^{-2}	1.164×10^{-3}
256	0.004297	1.903×10^{-4}	9.021×10^{-2}	4.567×10^{-1}	2.547×10^{-2}

Figure 3.54: Spatial refinement analysis for Prob. 3.20 ($Bi \approx 0.1$). Results are computed using 1D elements and a spatial refinement factor $r_x = 2$. The formal orders of accuracy are shown for each plot. *Left plot*: the L_2 norm quantifies convergence of the temperature distribution. *Right plot*: the H_1 norm quantifies convergence of the heat flux. *Table*: numerical values used to construct the plots.

Problem 3.21: Cylindrical gap heat transfer

An infinitely long fuel rod has constant thermal conductivity k and internal heat generation q'''. It is exposed on its right surface to some constant temperature $u(r_{co}) = u_{co}$. The temperature jump across the gap and cladding is

$$u_f - u_{co} = \frac{q'}{2\pi r_f h_{gap}} + \frac{q'}{2\pi k_c} \ln\left(\frac{r_{co}}{r_{ci}}\right), \tag{3.27a}$$

where u_f is the fuel surface temperature, u_{co} is the cladding outside temperature, and k_c is the cladding thermal conductivity. For this problem, the gap conductance h_{gap} reduces to $k_{gas}/(r_f \ln(r_{ci}/r_f))$, where k_{gas} is the thermal conductivity of the fill gas and r_{ci} is the cladding inside radius. The analytic solution for the temperature distribution in the fuel is

$$u(r) = u_f + \frac{q'}{4\pi k_f}\left(1 - \frac{r^2}{r_f^2}\right), \tag{3.27b}$$

where r_f is the fuel radius and k_f is the fuel thermal conductivity.

The problem is run in BISON using two blocks: the fuel domain (left block) on in $\boldsymbol{X} \in [0, 1.0]$ and the clad domain (right block) in $\boldsymbol{X} \in [1.1, 1.2]$. The domain between the two blocks is the gap and is filled with an inert gas with a predefined fill gas thermal conductivity. Neumann and Dirichlet boundary conditions are applied: $(du/dx)_{x=0} = 0$ and $u(x_{co}) = u_0$. Steady state heat conduction is considered with the following properties: fuel thermal conductivity $k_f = 10\,\mathrm{W/m/K}$, cladding thermal conductivity $k_c = 10\,\mathrm{W/m/K}$, volumetric heat generation $q''' = 400\,\mathrm{W/m^3}$, gas thermal conductivity $k_{gas} = 0.1\,\mathrm{W/m/K}$, and Biot number $Bi \approx 0.1$.

The exact and computed solutions are shown in Fig. 3.55 for three meshes and two FE types (linear: `EDGE2`; quadratic: `EDGE3`). A convergence study is performed with a refinement factor of two ($r_r = 2$). The mesh

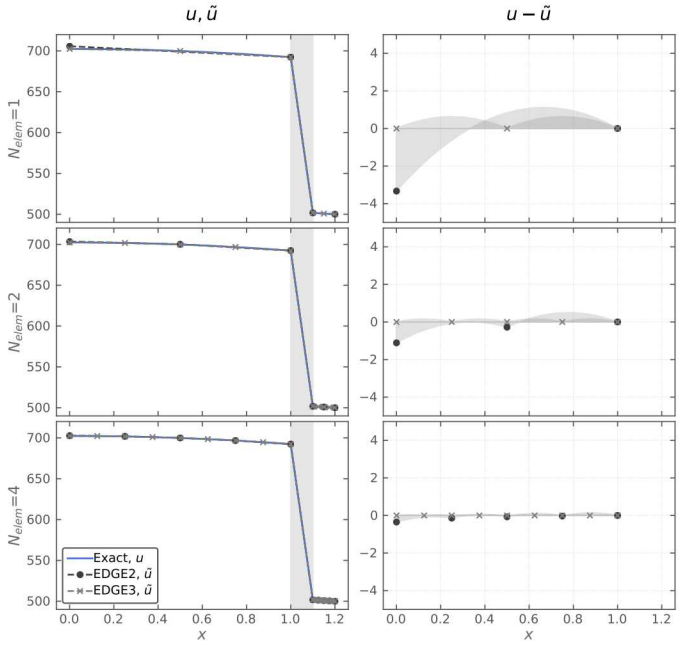

Figure 3.55: Temperature distribution and residuals for Prob. 3.21. Results are shown for the first three meshes. *First column*: exact and FE solutions using 1D elements. *Second column*: residuals are computed between the exact and computed solutions.

refinements are performed uniformly in both the fuel and cladding domains; however, the norms are computed only in the fuel domain. The computed norms are plotted and tabulated in Fig. 3.56. The linear FE solution is second order accurate, as expected. The quadratic solution is within numerical error of the exact solution due to its quadratic shape.

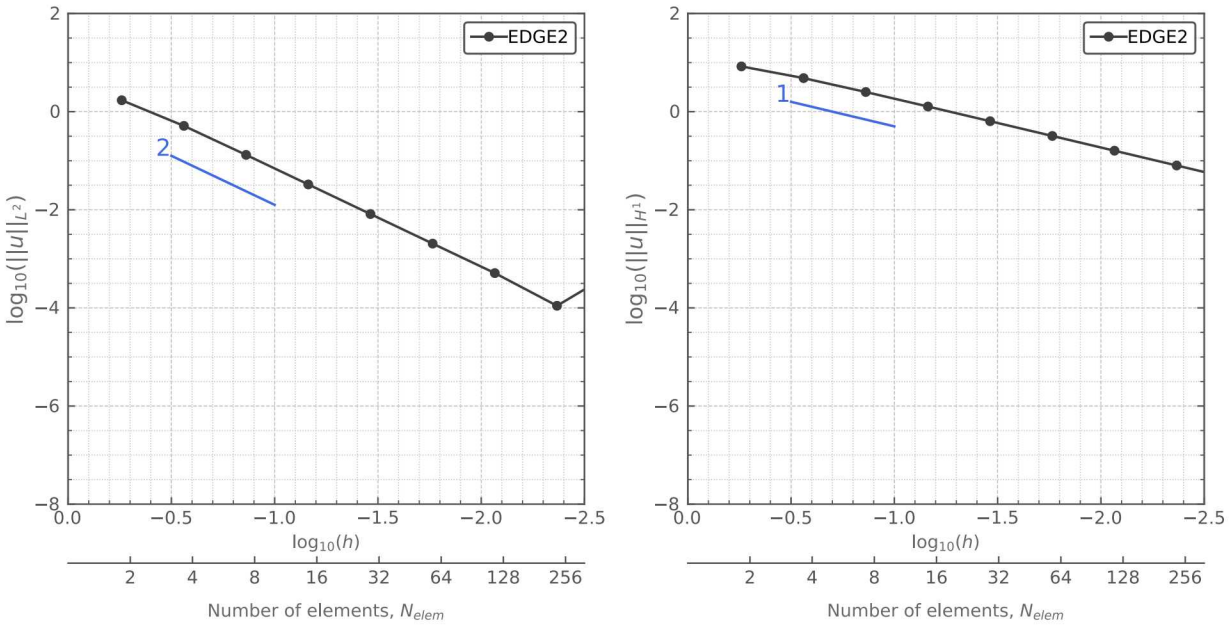

No. Elems	h	**Linear** ($p=1$) $\|\|u\|\|_{L_2}$	$\|\|u\|\|_{H_1}$	**Quadratic** ($p=2$) $\|\|u\|\|_{L_2}$	$\|\|u\|\|_{H_1}$
		elem_type=EDGE2		elem_type=EDGE3	
2	0.550000	1.707×10^{0}	8.355×10^{0}	9.814×10^{-7}	2.247×10^{-10}
4	0.275000	5.128×10^{-1}	4.824×10^{0}	8.239×10^{-8}	3.232×10^{-7}
8	0.137500	1.314×10^{-1}	2.513×10^{0}	5.104×10^{-7}	4.684×10^{-6}
16	0.068750	3.284×10^{-2}	1.272×10^{0}	1.188×10^{-7}	1.515×10^{-6}
32	0.034375	8.187×10^{-3}	6.386×10^{-1}	1.811×10^{-5}	1.684×10^{-6}
64	0.017188	2.043×10^{-3}	3.196×10^{-1}	3.613×10^{-4}	2.387×10^{-5}
128	0.008594	5.110×10^{-4}	1.599×10^{-1}	4.981×10^{-3}	3.682×10^{-4}
256	0.004297	1.106×10^{-4}	7.994×10^{-2}	2.069×10^{-1}	1.506×10^{-2}

Figure 3.56: Spatial refinement analysis for Prob. 3.21 ($Bi \approx 0.1$). Results are computed using 1D elements and a spatial refinement factor $r_r = 2$. The formal orders of accuracy are shown for each plot. *Left plot*: the L_2 norm quantifies convergence of the temperature distribution. *Right plot*: the H_1 norm quantifies convergence of the heat flux. *Table*: numerical values used to construct the plots.

Problem 3.22: Spherical gap heat transfer

A fuel sphere has constant thermal conductivity k and internal heat generation q'''. It is exposed on its right surface to some constant temperature $u(r_{co}) = u_{co}$. The temperature jump across the gap and cladding is

$$u_f - u_{co} = \frac{q'}{4\pi r_f^2 h_{gap}} + \frac{q'}{4\pi k_c}\left(\frac{1}{r_{ci}} - \frac{1}{r_{co}}\right), \tag{3.28a}$$

where u_f is the fuel surface temperature, u_{co} is the cladding outside temperature, and k_c is the cladding thermal conductivity. For this problem, the gap conductance h_g reduces to $k_{gas}/(r_f^2(r_f^{-1} - r_{ci}^{-1}))$, where k_{gas} is the thermal conductivity of the fill gas and r_{ci} is the cladding inside radius. The analytic solution for the temperature distribution in the fuel is

$$u(r) = u_f + \frac{q'}{8\pi r_f k_f}\left(1 - \frac{r^2}{r_f^2}\right), \tag{3.28b}$$

where r_f is the fuel radius and k_f is the fuel thermal conductivity.

The problem is run in BISON using two blocks: the fuel domain (left block) on in $\boldsymbol{X} \in [0, 1.0]$ and the clad domain (right block) in $\boldsymbol{X} \in [1.1, 1.2]$. The domain between the two blocks is the gap and is filled with an inert gas with a predefined fill gas thermal conductivity. Neumann and Dirichlet boundary conditions are applied: $(du/dx)_{x=0} = 0$ and $u(x_{co}) = u_0$. Steady state heat conduction is considered with the following properties: fuel thermal conductivity $k_f = 10\,\mathrm{W/m/K}$, cladding thermal conductivity $k_c = 10\,\mathrm{W/m/K}$, volumetric heat generation $q''' = 400\,\mathrm{W/m^3}$, gas thermal conductivity $k_{gas} = 0.1\,\mathrm{W/m/K}$, and Biot number $Bi \approx 0.1$.

The exact and computed solutions are shown in Fig. 3.57 for three meshes and two FE types (linear: `EDGE2`; quadratic: `EDGE3`). A convergence study is performed with a refinement factor of two ($r_x = 2$). The mesh refinements are performed uniformly in both the fuel and cladding domains; however, the

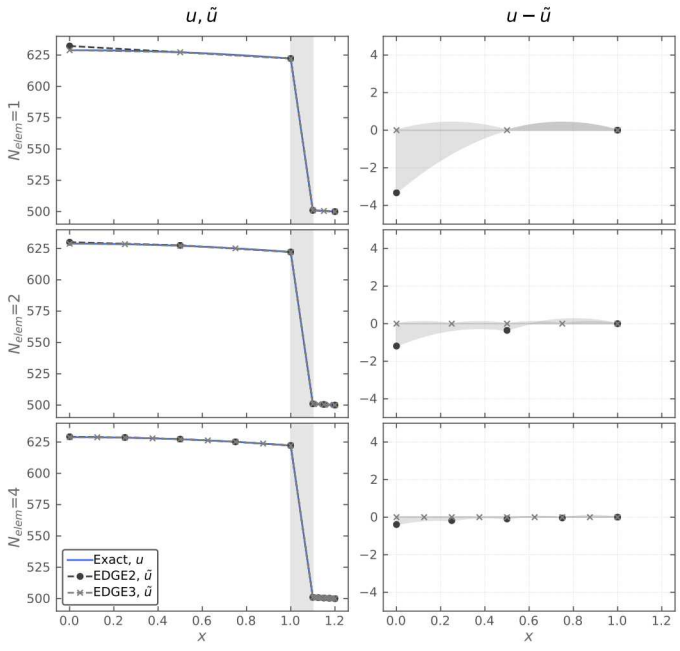

Figure 3.57: Temperature distribution and residuals for Prob. 3.22. Results are shown for the first three meshes. *First column*: exact and FE solutions using 1D elements. *Second column*: residuals are computed between the exact and computed solutions.

norms are computed only in the fuel domain. The computed norms are plotted and tabulated in Fig. 3.58. The linear FE solution is second order accurate, as expected. The quadratic solution is within numerical error of the exact solution due to its quadratic shape.

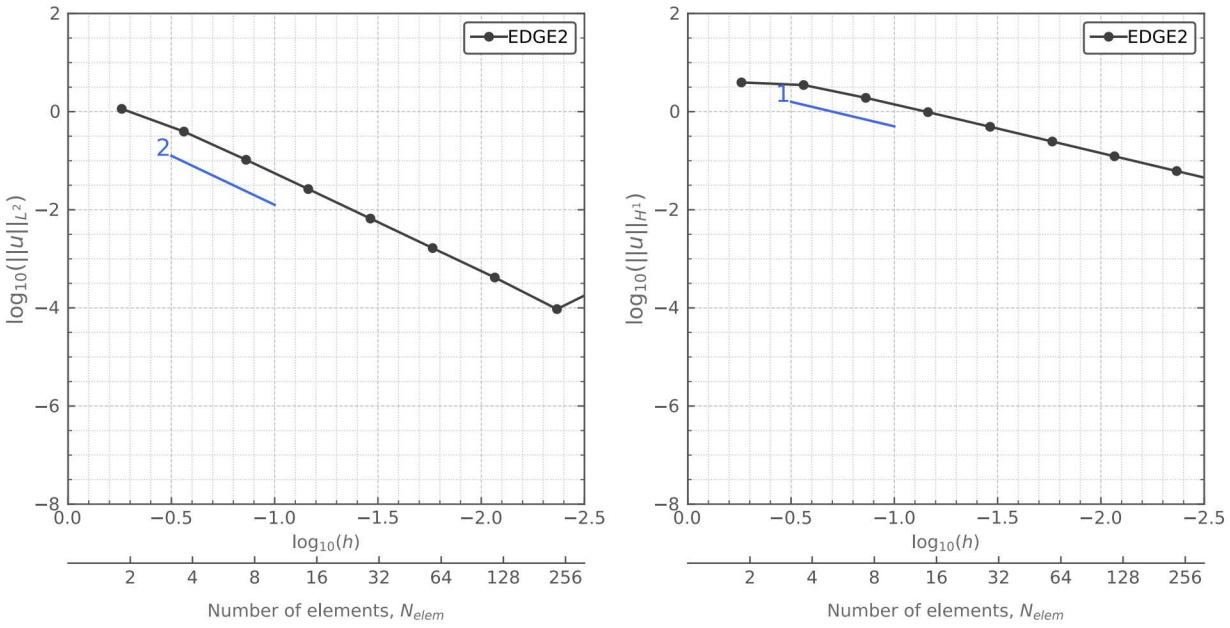

No. Elems	h	**Linear** ($p=1$) $\|\|u\|\|_{L_2}$	$\|\|u\|\|_{H_1}$	**Quadratic** ($p=2$) $\|\|u\|\|_{L_2}$	$\|\|u\|\|_{H_1}$
		elem_type=EDGE2		elem_type=EDGE3	
2	0.550000	1.140×10^{0}	3.939×10^{0}	5.914×10^{-6}	3.716×10^{-11}
4	0.275000	3.927×10^{-1}	3.491×10^{0}	3.190×10^{-7}	2.009×10^{-7}
8	0.137500	1.044×10^{-1}	1.912×10^{0}	1.223×10^{-7}	1.974×10^{-6}
16	0.068750	2.643×10^{-2}	9.773×10^{-1}	7.120×10^{-7}	3.652×10^{-7}
32	0.034375	6.626×10^{-3}	4.914×10^{-1}	1.719×10^{-6}	4.472×10^{-7}
64	0.017188	1.657×10^{-3}	2.461×10^{-1}	7.594×10^{-4}	6.617×10^{-5}
128	0.008594	4.165×10^{-4}	1.231×10^{-1}	1.676×10^{-4}	1.457×10^{-5}
256	0.004297	9.451×10^{-5}	6.154×10^{-2}	1.676×10^{-4}	1.457×10^{-5}

Figure 3.58: Spatial refinement analysis for Prob. 3.22 ($Bi \approx 0.1$). Results are computed using 1D elements and a spatial refinement factor $r_r = 2$. The formal orders of accuracy are shown for each plot. *Left plot*: the L_2 norm quantifies convergence of the temperature distribution. *Right plot*: the H_1 norm quantifies convergence of the heat flux. *Table*: numerical values used to construct the plots.

4. Concluding Remarks

In this study, the fuel performance code BISON was verified using an extensive set of verification problems. The majority of problems were designed to test BISON's conduction solution, and two additional problems test the mechanics capabilities. A physics-based approach was used to design a verification matrix which included all combinations of physics and simulation options. By mapping out code capabilities in a verification matrix, it is ensured that all capabilities are tested and gaps are clearly identified. The considered code capabilities were: treatment of the temporal term, chosen coordinate system, dimensionality, material property treatment, external source treatment, and boundary condition options.

Sixteen MES problems and three MMS problems were employed for the basic heat conduction solution. Three additional MES problems tested the heat conduction solution in the presence of a gap. Two MES problems were added to test the mechanical solution in the elastic region. These problems were selected to fill obvious gaps in the verification matrix. Though the matrix is not fully covered, this work establishes a baseline pedigree of the code which can be expanded upon later.

1. All one-dimensional verification problems display the proper convergence behavior for both first and second order Lagrange polynomials using any type of FE. This includes:
   - second order convergence of the temperature distribution for linear FEs,
   - first order convergence of the heat flux for linear FEs,
   - third order convergence of the temperature distribution for quadratic FEs,
   - second order convergence of the heat flux for quadratic FEs, and
   - super-convergent behavior for problems where the FEs shape matches the analytic solution.
2. The verification studies performed in this work are being incorporated into BISON documentation and automated test suites.
3. The capability of BISON to solve MMS problems has been demonstrated for the first time. This is an important step for future verification work, as MMS is the state-of-the-art verification method.
4. For two-dimensional problems, corner singularities arise due to non-smoothness of the domain (corners, edges, etc. on the boundary), change of the boundary conditions from one type to another, or discontinuities of the solution or model coefficients. For most problems, these effects are mild enough to maintain first order convergence.

5. Bessel functions and infinite series are not yet implemented as functions in MOOSE. This limits the multi-dimensional problems which can be incorporated into the BISON verification matrix, since their analytic solutions are complex functions.
6. The problems in this study use simplest meshes and uniform mesh refinement. This creates a strong base of verification, but future work may expand to more complicated refinement strategies: more complex meshes, non-uniform mesh refinement, local mesh refinement, differing aspect ratios, and combined temporal/spatial order analysis.

This work is the first expansive verification work performed for the BISON code. It establishes supporting evidence that the BISON solution is a faithful representation of the underlying mathematical model, especially for the heat conduction solution.

In the future, this work will be expanded to include testing of species conservation and more expansive testing of the mechanical response. Though two mechanics problems are created for this study (see Appendix B), a great number of tests is necessary to create a proper verification matrix to cover the mechanics. Significant effort is required to expand the verification matrix to include two- and three-dimensional problems, problems with atypical behavior, and problems that couple more than one conservation equation. This could reveal numerical bugs that are hidden when only individual equations are tested.

Acknowledgments

Thanks to Aaron Krueger (SNL) for his review of this document. Dylan McDowell (INL) performed preliminary work on the thick wall-cylinder problem to setup input (Prob. B.2).

This research is supported by and performed in conjunction with the Consortium for Advanced Simulation of Light Water Reactors (`http://www.casl.gov`), an Energy Innovation Hub (`http://www.energy.gov/hubs`) for Modeling and Simulation of Nuclear Reactors under US Department of Energy Contract No. DE-AC05-00OR22725. Any opinions, findings, conclusions, or recommendations expressed in this material are those of the authors and do not necessarily reflect the views of the US Department of Energy.

Bibliography

[1] D Gaston et al. "MOOSE: A parallel computational framework for coupled systems of nonlinear equations". In: *Nuclear Engineering and Design* 239.10 (2009), pp. 1768–1778. DOI: 10.1016/j.nucengdes.2009.05.021.

[2] R L Williamson et al. "Multidimensional multiphysics simulation of nuclear fuel behavior". In: *Journal of Nuclear Materials* 423.1–3 (2012), pp. 149–163. DOI: 10.1016/j.jnucmat.2012.01.012.

[3] J D Hales et al. *BISON Theory Manual The Equations Behind Nuclear Fuel Analysis*. Idaho National Laboratory. Idaho Falls, Idaho, Oct. 2014.

[4] Nuclear Regulatory Commission. *10 CFR Part 50: Domestic Licensing of Production and Utilization Facilities*. https://www.nrc.gov/reading-rm/doc-collections/cfr/part050/.

[5] W L Oberkampf and C J Roy. *Verification and Validation in Scientific Computing*. First. Cambridge, UK: Cambridge University Press, Nov. 2010.

[6] W L Oberkampf, M Pilch, and T G Trucano. *Predictive Capability Maturity Model for Computational Modeling and Simulation*. Tech. rep. SAND2007-5948. Sandia National Laboratories, Oct. 2007.

[7] P J Roache. *Verification and Validation in Computational Science and Engineering*. Albuquerque, NM: Hermosa Publishing, 1998.

[8] A Toptan et al. "Implementation and Assessment of Wall Friction Models for LWR Core Analysis". In: *Annals of Nuclear Energy* 115 (2018), pp. 565–572. DOI: 10.1016/j.anucene.2018.02.022.

[9] A Toptan et al. "A new fuel modeling capability, CTFFuel, with a case study on the fuel thermal conductivity degradation". In: *J Nuclear Eng Design* 341 (2019), pp. 248–258. DOI: 10.1016/j.nucengdes.2018.11.010.

[10] N W Porter. "Development of a Novel Residual Formulation of CTF and Application of Parameter Estimation Techniques". PhD thesis. North Carolina State University, 2018.

[11] Bison Team. *Assessment of BISON: A Nuclear Fuel Performance Analysis Code*. Tech. rep. INL/MIS-13-30314 Rev. 4. Idaho Falls, Idaho: Idaho National Laboratory, Aug. 2017.

[12] J Hales et al. "Verification of the BISON Fuel Performance Code". In: *Annals of Nuclear Energy* 71 (81–90), p. 2014. DOI: 10.1016/j.anucene.2014.03.027.

[13] D S Burnett. "Finite Element Analysis from Concepts to Applications". In: Reading, MA: Addison-Wesley Publishing Company, 1987. Chap. 9.

[14] E R de Arantes e Oliveira. "Theoretical Foundations of the Finite Element Method". In: *Int J Solids Struct* 4.10 (Oct. 1968), pp. 929–952. DOI: 10.1016/0020-7683(68)90014-0.

[15] A K Aziz. *The Mathematical Foundations of The Finite Element Method with Applications to Partial Differential Equations*. New York, NY: Academic Press, 1972. Chap. 6.

[16] J T Oden and J N Reddy. *An Introduction to the Mathematical Theory of Finite Elements*. New York, NY: John Wiley & Sons, 1976. Chap. 8.4.

[17] O C Zienkiewicz, R L Taylor, and J Z Zhu. *The Finite Element Method Its Basis & Fundamentals*. New York, NY: Elsevier, 2013. Chap. 7.9. DOI: 10.1016/C2009-0-24909-9.

[18] M Skroch et al. *CUBIT: Geometry and Mesh Generation Toolkit, 15.5 User Documentation*. Tech. rep. SAND2019-3478W. SNL, 2019.

[19] K Salari and P Knupp. *Code Verification by the Method of Manufactured Solutions*. Tech. rep. SAND2000-1444. Sandia National Laboratories, June 2000. DOI: 10.2172/759450. URL: https://www.osti.gov/servlets/purl/759450.

[20] M P McHale et al. *Standard for Verification and Validation in Computational Fluid Dynamics and Heat Transfer*. Standard ASME V&V 20-2009. American Society of Mechanical Engineers, 2009.

[21] I Babuska and B Szabo. "On the Rates of Convergence of the Finite Element Method". In: *Int J for Numerical Methods in Engineering* 18.3 (Mar. 1982), pp. 323–341. DOI: 10.1002/nme.1620180302.

[22] I Babuska, B A Szabo, and I N Katz. "The p-version of the Finite Element Method". In: *SAM J Numer Anal* 18.3 (June 1981), pp. 515–545. DOI: 10.1137/0718033.

[23] J Kamm, W Rider, and J Brock. "Combined Space and Time Convergence Analysis of a Compressible Flow Algorithm". In: *AIAA Paper* (2003-4041). DOI: 10.2514/6.2003-4241.

[24] S A Richards. "Completed Richardson extrapolation in space and time". In: *Communications in Numerical Methods in Engineering* 13.7 (1997), pp. 573–582. DOI: 10.1002/(SICI)1099-0887(199707)13:7<573::AID-CNM84>3.0.CO;2-6.

[25] E Isaacson and H B Keller. *Analysis of Numerical Methods*. New York, NY: Dover Publications, 1994.

[26] M Jakob. *Heat transfer*. Vol. 1. New York: Wiley, 1949.

[27] V S Arpaci. *Conduction Heat Transfer*. Reading, MA: Addison-Wesley Publishing Company, 1966.

[28] P J Scheider. *Conduction Heat Transfer*. Cambridge 42, Mass.: Addison-Wesley Publishing Company, Inc., 1955.

[29] J H VanSant. *Conduction Heat Transfer Solutions*. Tech. rep. UCRL—52863-Rev.l; DE87 012387. CA (USA): Lawrence Livermore National Lab., Aug. 1983. DOI: 10.2172/6224569.

[30] S S Kutateladze and V M Borishanskii. *A Concise Encyclopedia of Heat Transfer*. New York, NY: Pergamon, 1966.

[31] R B Bird, W E Stewart, and E N Lightfoot. *Transport Phenomena*. New York, New York: John Wiley & Sons, Inc., 1960.

[32] H S Carslaw and J C Jaeger. *Conduction of Heat in Solids*. 2nd. Oxford at The Clarendon Press, 1959.

[33] R Wait and A R Mitchell. "Corner singularities in elliptic problems by finite element methods". In: *Journal of Computational Physics* 8.1 (1971), pp. 45–52. DOI: 10.1016/0021-9991(71)90033-7.

[34] Z Cai and S Kim. "A Finite Element Method Using Singular Functions for the Poisson Equation: Corner Singularities". In: *SIAM Journal on Numerical Analysis* 39.1 (2001). DOI: 10.1137/S0036142999355945.

[35] D Givoli, L Rivkin, and J B Keller. "A finite element method for domains with corners". In: 35.6 (1992), pp. 1329–1345. DOI: 10.1002/nme.1620350611.

[36] Y N Anjam. "Singularities and regularity of stationary Stokes and Navier-Stokes equations on polygonal domains and their treatments". In: *AIMS Mathematics* 5.1 (2020), pp. 440–466. DOI: 10.3934/math.2020030.

[37] J Pfefferer and M Winkler. "Finite element error estimates for normal derivatives on boundary concentrated meshes". In: *SIAM Journal on Numerical Analysis* 57.5 (2018), pp. 2043–2073. DOI: 10.1137/18M1181341. URL: https://arxiv.org/pdf/1804.05723.pdf.

[38] A Toptan. "A Novel Approach to Improve Transient Fuel Performance Modeling in Multi-Physics Calculations". PhD thesis. North Carolina State University, Nuclear Engineering Department, 2019. URL: https://repository.lib.ncsu.edu/handle/1840.20/36352.

[39] A Toptan, D J Kropaczek, and M N Avramova. "On the Validity of the Dilute Gas Assumption for Gap Conductance Calculations in Nuclear Fuel Performance Codes". In: *Nuclear Eng Design* 350 (2019), pp. 1–8. DOI: 10.1016/j.nucengdes.2019.04.042.

[40] A Toptan, D J Kropaczek, and M N Avramova. "Gap conductance modeling I: Theoretical considerations for single- and multi-component gases in curvilinear coordinates". In: *Nuclear Eng Design* 353 (2019). DOI: 10.1016/j.nucengdes.2019.110283.

[41] A Toptan, D J Kropaczek, and M N Avramova. "Gap conductance modeling II: Optimized model for UO_2-Zircaloy interfaces". In: *Nuclear Eng Design* 355 (2019). DOI: 10.1016/j.nucengdes.2019.110289.

[42] A Toptan et al. "Modeling of gap conductance for LWR fuel rods applied in the BISON code". In: *Journal of Nuclear Science and Technology* (2020). (*in PRESS*). DOI: 10.1080/00223131.2020.1740808.

[43] W C Young and R G Budynas. *Roark's Formulas for Stress and Strain*. 7th. New York, NY: McGraw-Hill, 2002.

A. Vector Identities

The vector $\boldsymbol{u}$ is expressed by $\boldsymbol{u} = \boldsymbol{i}_1 u_1 + \boldsymbol{i}_2 u_2 + \boldsymbol{i}_1 u_3$ in terms of the local unit vectors $\boldsymbol{i}_i$ for $i = 1, 2, 3$. ψ denotes a scalar.

- **Cartesian coordinates** (x, y, z)

$$\begin{aligned}
\text{Gradient of } \psi: \quad & \nabla\psi = && \boldsymbol{i}_x \frac{\partial \psi}{\partial x_1} + \boldsymbol{i}_y \frac{\partial \psi}{\partial x_2} + \boldsymbol{i}_z \frac{\partial \psi}{\partial x_3} \\
\text{Laplacian of } \psi: \quad & \nabla^2\psi = && \frac{\partial^2 \psi}{\partial x^2} + \frac{\partial^2 \psi}{\partial x_2^2} + \frac{\partial^2 \psi}{\partial x_3^2} \\
\text{Divergence of } \boldsymbol{u}: \quad & \nabla \cdot \boldsymbol{u} = && \frac{\partial u_1}{\partial x_1} + \frac{\partial u_2}{\partial x_2} + \frac{\partial u_3}{\partial x_3} \\
\text{Curl of } \boldsymbol{u}: \quad & \nabla \times \boldsymbol{u} = && \boldsymbol{i}_x \left(\frac{\partial u_3}{\partial x_2} - \frac{\partial u_2}{\partial x_3} \right) + \boldsymbol{i}_y \left(\frac{\partial u_1}{\partial x_3} - \frac{\partial u_3}{\partial x_1} \right) + \boldsymbol{i}_z \left(\frac{\partial u_2}{\partial x_1} - \frac{\partial u_1}{\partial x_2} \right)
\end{aligned}$$

- **Cylindrical coordinates** (r, θ, z)

$$\begin{aligned}
\text{Gradient of } \psi: \quad & \nabla\psi = && \boldsymbol{i}_r \frac{\partial \psi}{\partial r} + \frac{\boldsymbol{i}_\theta}{r} \frac{\partial \psi}{\partial \theta} + \boldsymbol{i}_z \frac{\partial \psi}{\partial z} \\
\text{Laplacian of } \psi: \quad & \nabla^2\psi = && \frac{1}{r} \frac{\partial}{\partial r} \left(r \frac{\partial \psi}{\partial r} \right) + \frac{1}{r^2} \frac{\partial^2 \psi}{\partial \theta^2} + \frac{\partial^2 \psi}{\partial z^2} \\
\text{Divergence of } \boldsymbol{u}: \quad & \nabla \cdot \boldsymbol{u} = && \frac{1}{r} \frac{\partial (r u_1)}{\partial r} + \frac{1}{r} \frac{\partial u_2}{\partial \theta} + \frac{\partial u_3}{\partial z} \\
\text{Curl of } \boldsymbol{u}: \quad & \nabla \times \boldsymbol{u} = && \boldsymbol{i}_r \left(\frac{1}{r} \frac{\partial u_3}{\partial \theta} - \frac{\partial u_2}{\partial z} \right) + \boldsymbol{i}_\theta \left(\frac{\partial u_1}{\partial z} - \frac{\partial u_3}{\partial r} \right) + \boldsymbol{i}_z \left[\frac{1}{r} \frac{\partial (r u_2)}{\partial r} - \frac{1}{r} \frac{\partial u_1}{\partial \theta} \right]
\end{aligned}$$

- **Spherical coordinates** (r, θ, φ)

$$\text{Gradient of } \psi: \quad \nabla\psi = \boldsymbol{i}_r \frac{\partial\psi}{\partial r} + \boldsymbol{i}_\theta \frac{1}{r}\frac{\partial\psi}{\partial\theta} + \boldsymbol{i}_\phi \frac{1}{r\sin\theta}\frac{\partial\psi}{\partial\varphi}$$

$$\text{Laplacian of } \psi: \quad \nabla^2\psi = \frac{1}{r^2}\frac{\partial}{\partial r}\left(r^2\frac{\partial\psi}{\partial r}\right) + \frac{1}{r^2\sin\theta}\frac{\partial}{\partial\theta}\left(\sin\theta\frac{\partial\psi}{\partial\theta}\right) + \frac{1}{r^2\sin^2\theta}\frac{\partial^2\psi}{\partial\varphi^2}$$

$$\text{Divergence of } \boldsymbol{u}: \quad \nabla\cdot\boldsymbol{u} = \frac{1}{r^2}\frac{\partial(r^2u_1)}{\partial r} + \frac{1}{r\sin\theta}\frac{\partial(u_2\sin\theta)}{\partial\theta} + \frac{1}{r\sin\theta}\frac{\partial u_2}{\partial\varphi}$$

$$\text{Curl of } \boldsymbol{u}: \quad \nabla\times\boldsymbol{u} = \frac{\boldsymbol{i}_r}{r\sin\theta}\left[\frac{\partial(u_3\sin\theta)}{\partial\theta} - \frac{\partial u_2}{\partial\varphi}\right] + \frac{\boldsymbol{i}_\theta}{r}\left[\frac{1}{\sin\theta}\frac{\partial u_1}{\partial\varphi} - \frac{\partial(ru_3)}{\partial r}\right] + \frac{\boldsymbol{i}_\varphi}{r}\left[\frac{\partial(ru_2)}{\partial r} - \frac{\partial u_1}{\partial\theta}\right]$$

B. Mechanics: Method of Exact Solutions

Problem B.1: Static, 1D, an elastic rod subjected to stress

Considering a rod of length, l in the absence of any body forces subject to an applied stress of σ_0. The displacement, u is obtained by

$$u(x) = \frac{\sigma_0}{E}\left(x - \frac{l}{2}\right) \tag{B.1}$$

where E is the Young's modulus, σ_0 is the applied stress.

The governing equations for the static response of the rod are:

$$\text{equation of equilibrium:} \quad \frac{d\sigma}{dx} + b = 0, \tag{B.2}$$

$$\text{strain-displacement relation:} \quad \varepsilon = \frac{du}{dx}, \tag{B.3}$$

$$\text{constitutive relation:} \quad \sigma = E\varepsilon. \tag{B.4}$$

where E is the Young's modulus, u is the displacement, ε is the strain, and b is the body force.

The problem domain is defined in $\boldsymbol{X} \in [0, 1]$. Fig. B.1 shows the exact and FE solutions of the displacement and strain. The solution is super-convergent for both linear and quadratic FEs due to the linearity of Eq. B.1.

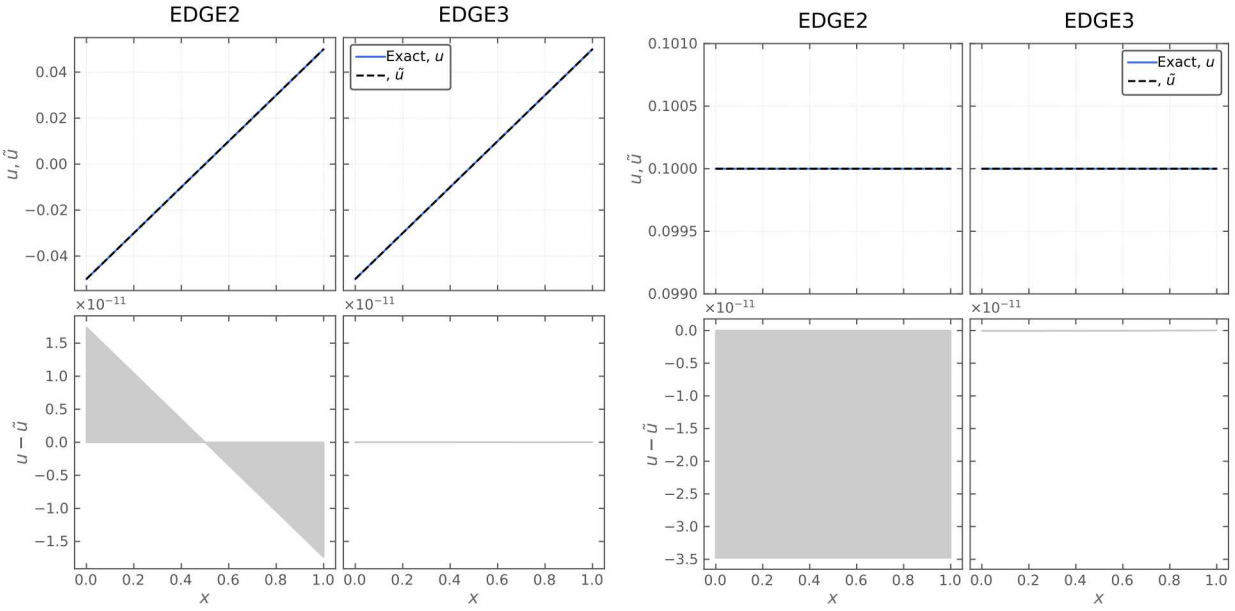

(a) Displacement u

(b) Strain ε

Figure B.1: Displacement, strain, and residuals for Prob. B.1. Results are shown for the first two meshes. *First row*: exact and FE solutions using 1D elements. *Second row*: residuals between the exact solution and the FE solutions.

Table B.1: Norms computed for Prob. B.1 from the spatial refinement analysis ($r_x = 2$). The errors are computed in two ways: (1) L_2 norm and (2) H_1 norm.

No. Elems	h	**Linear** ($p = 1$) $\|\|u\|\|_{L_2}$	$\|\|u\|\|_{H_1}$	**Quadratic** ($p = 2$) $\|\|u\|\|_{L_2}$	$\|\|u\|\|_{H_1}$
		elem_type=EDGE2		elem_type=EDGE3	
1	1.000000	2.276×10^{-13}	7.886×10^{-13}	2.276×10^{-13}	7.886×10^{-13}
2	0.500000	2.276×10^{-13}	7.886×10^{-13}	3.716×10^{-12}	1.287×10^{-11}
4	0.250000	2.752×10^{-12}	9.532×10^{-12}	7.520×10^{-12}	2.605×10^{-11}
8	0.125000	8.527×10^{-12}	2.954×10^{-11}	1.476×10^{-15}	8.534×10^{-15}
16	0.062500	2.034×10^{-12}	7.044×10^{-12}	1.372×10^{-17}	1.186×10^{-16}
32	0.031250	1.004×10^{-11}	3.479×10^{-11}	1.690×10^{-14}	5.390×10^{-14}

Problem B.2: Static axisymmetric 1D problem, thick-walled cylinder subjected to internal pressure

A thick-walled cylinder is subjected to a uniform radial internal pressure, q and a traction-free external pressure [43, 17]. For the axisymmetric one-dimensional problem in which no rigid body modes exist. No essential displacement boundary conditions are necessary. Ignored temperature and inertia effects. The normal stresses in the longitudinal, circumferential, and radial directions are respectively denoted as σ_1, σ_2, and σ_3:

$$\sigma_1 = \frac{-qb^2\left(a^2 - r^2\right)}{r^2\left(a^2 - b^2\right)}, \qquad \sigma_2 = 0, \qquad \sigma_3 = \frac{qb^2\left(a^2 + r^2\right)}{r^2\left(a^2 - b^2\right)} \tag{B.5}$$

where a is the outer radius and b is the inner radius ($a < b$), r is the radius, q is the force per unit area.

The axisymmetric elasticity problem. Let us consider an infinitely long cylinder in which the displacement field is given by $u(r, z) = u(r)$ and $v(r, z) = 0$ [17, pp.73–74]. The non-zero strains are $\boldsymbol{\varepsilon} = \{\varepsilon_r, \varepsilon_\theta\} = \left\{\frac{\partial u}{\partial r}, \frac{u}{r}\right\}$. The equilibrium equation simplifies to the following form

$$\frac{\partial \sigma_r}{\partial r} + \frac{\sigma_r - \sigma_\theta}{r} + b_r = \rho \frac{\partial^2 u}{\partial t^2}. \tag{B.6}$$

For an isotropic material, stress-strain relations—including temperature effects—are given by

$$\begin{pmatrix} \sigma_r \\ \sigma_\theta \end{pmatrix} = \frac{E}{(1+\nu)(1-2\nu)} \begin{bmatrix} (1-\nu) & \nu \\ \nu & (1-\nu) \end{bmatrix} \begin{pmatrix} \varepsilon_r - \alpha\Delta T \\ \varepsilon_\theta - \alpha\Delta T \end{pmatrix} \tag{B.7}$$

and

$$\sigma_z = \nu(\sigma_r + \sigma_\theta) - E\alpha\Delta T \tag{B.8}$$

where E is Young's modulus and ν is Poisson's ratio.

The problem domain is defined in $\boldsymbol{X} \in [0.5, 1.0]$. A Dirichlet boundary conditions is applied to the bottom boundary and the left boundary is a pressure boundary. Young's modulus is $E = 10\,000\,\mathrm{N/m^2}$ and Poisson's ratio is $\nu = 0.3$. Fig. B.2 shows the exact solution and FE solutions of the axisymmetric problem. The results are shown with 32x32 elements for each 2D element type.

The analytical solution exists for the stresses, however the primary variable is displacement. Therefore, the expected convergence behavior of the displacement cannot be captured through the use of a code verification study. Instead, *solution verification* is performed and the results are shown in Fig. B.3. Norms are calculated by comparing successively refined solutions at the inner surface of the cylinder.

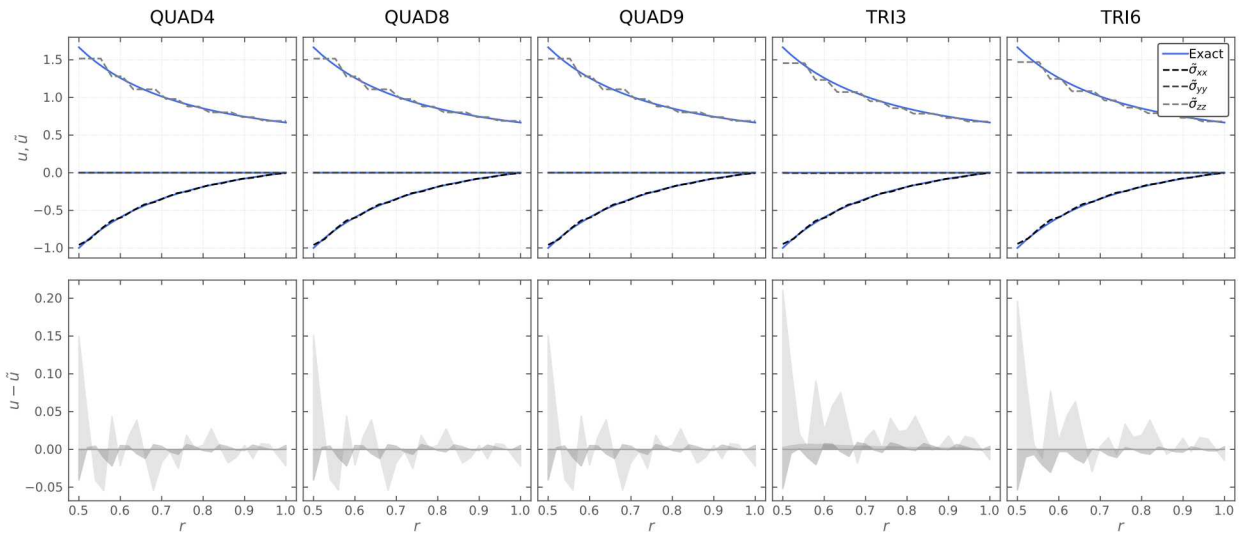

Figure B.2: Exact and FE solutions for Prob. B.2. Results are shown for a single a 32x32 mesh for five different types of FE. *First row*: exact and FE solutions using 2D elements for one-dimensional FE solution of stresses. *Second row*: residuals between the exact solution and the FE solutions.

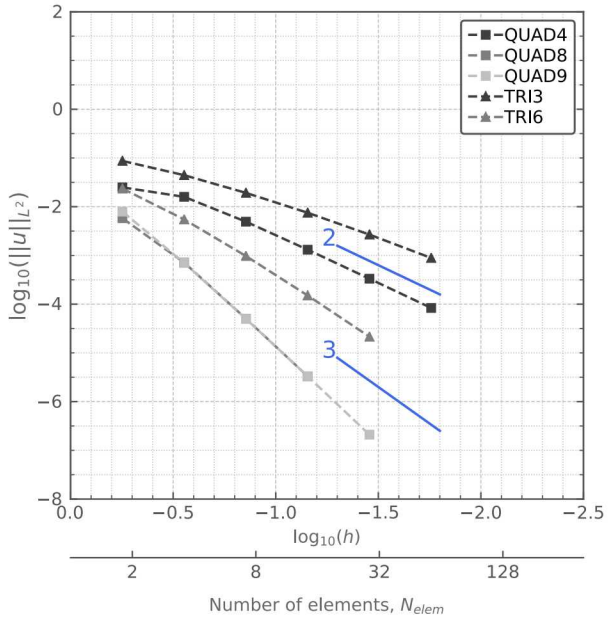

Figure B.3: Spatial refinement analysis for Prob. B.2. Solution verification at the inner surface for displacement solution of the axisymmetric problem. Errors are quantified in terms of the L_2 norm.